NANOSCALE OPTICAL DEVICES BASED ON PHASE COHERENT ELECTRON TRANSPORT

A Dissertation
Presented to
The Academic Faculty

By

Mahbub Alam

In Partial Fulfillment
of the Requirements for the Degree
Doctor of Philosophy
in
Electrical and Computer Engineering

School of Electrical and Computer Engineering
Georgia Institute of Technology
December 2016

NANOSCALE OPTICAL DEVICES BASED ON PHASE COHERENT ELECTRON TRANSPORT

Approved by:

Dr. David S Citrin, Committee Chair
Professor, School of ECE
Georgia Institute of Technology

Dr. Azad J Naeemi
Associate Professor, School of ECE
Georgia Institute of Technology

Dr. Paul L. Voss, Advisor
Associate professor, School of ECE
Georgia Institute of Technology

Dr. Nico F Declercq
Associate Professor, School of ME
Georgia Institute of Technology

Dr. Paul Douglas Yoder
Associate Professor, School of ECE
Georgia Institute of Technology

Date Approved: August 19, 2016

To anyone who loves science and the mysteries of the universe

ACKNOWLEDGMENT

I would like to thank my advisor, Dr. Voss, for his support and encouragement. I would also like to thank Dr. Citrin for the talks we had on research.

I acknowledge the support of my family members without whose love and support this work would not have been possible.

TABLE OF CONTENTS

LIST OF TABLES

LIST OF FIGURES

SUMMARY

The optical interaction of phase coherent electron in an open system has been investigated. It has been found that after optical excitation electron wavefunction evolves in a coherent manner in excited state and quantum interference of phase coherent electrons after optical excitation gives rise to periodic oscillation in photocurrent as a function of illumination length. This periodic oscillation results in illumination length dependent optical absorption for a material at illumination length around the Bloch wavelength of participating electrons. Under sub Bloch wavelength illumination, which has been investigated to be experimentally achievable with nanoplasmonic focusing, of a particular structure, where a gate potential has been applied in half of the device, the quantum interference of electrons can be utilized to manufacture new kinds of photodetectors where current in the external circuit changes direction with change in wavelength of light. This is a completely new phenomenon and only achievable with coherent wave-nature of electron and sub Bloch wavelength illumination. Momentum conserved transition has not been found as a necessary requirement for optical transition for Bloch scale illumination as momentum of the electron is not defined for ultra-small scale illumination. From the uncertainty of position and momentum of electron in the illumination area, a way of verifying Heisenberg uncertainty principle via optical absorption has been suggested under ultra-small scale illumination. Also, the coupling of longitudinal resonant modes, which arises from phase coherent electron transport in a Mach Zehnder interferometer structure, has been investigated for manufacturing a p-n junctionless, high quantum efficiency photodetector. A new spectrometer device under coherent electron transport regime which can detect and distinguish light of different frequencies has also been discussed. A new study field called opto coherent electronics has been proposed.

CHAPTER 1

INTRODUCTION

We live in an era of miniaturization. The quest for miniaturization is driven by the need for increasing processing power, decreased cost and increased portability. The transistor size in the present day Intel Skylake processor is 14 nm. Below device dimensions of 100 nm emergent phenomena have given rise to the new field of nanotechnology. The challenge is that when at small scales, one cannot treat the participating entities (electrons for our case) as particles which are governed by classical Newtonian mechanics. One must take into account the dual wave-particle nature of electrons which is described by quantum mechanics. Two of the most fundamental phenomena, tunneling and interference, can only be explained by the wave nature of electron as described by Schrodinger equation.

The quest for miniaturization in the post-silicon age has given rise to the discovery of new materials like graphene, for which a Nobel prize was awarded in 2010. Graphene is a single layer of carbon atoms arranged in a honey-comb lattice structure. Graphene has exceptional electronic, mechanical and optical properties[4, 5, 6]. One amazing thing about graphene is that quantum phenomena can be observed at room temperature. Graphene exhibits ballistic electron transport over unusually large lengths[2, 7, 8, 9, 10]. Researchers have recently measured momentum relaxation length of 10 μm in graphene nanoribbons at room temperature[2]. Up to this length, resistance is independent of length and Ohm's law does not describe transport[11]. Other researchers have also demonstrated a phase coherent length of 1 μm at low temperature ($4^{\circ}K$)[8], 50 nm at $100^{\circ}K$ [12] and an expected coherent length of 10-30 nm at $300^{\circ}K$[12]. Phase coherent length is defined to be the length up to which electrons keep their phase coherent wave nature and interference phenomena can be observed[11]. With current semiconductor device size approaching its limits, a potential path forward could be new device structures which use the wave property of electrons.

The aim of coherent electronics is to invent new devices whose operating principle

is based on the wave nature of electron. In a coherent optoelectronic system, during interaction with light, the whole system (electrons and photons) evolves in a coherent way. But the disadvantage with coherent electronics or optoelectronics is that electrons lose their coherence due to interaction with environment (phonon, impurity or other electrons) within a very short time and very short distance. So in order to reach the coherence limit, one must fabricate shorter structures or use new materials or structures with longer coherence lengths or operate at low temperature. The present time is a propitious time to investigate coherent electronics and optoelectronics because of the rapid advancement in fabrication technology and advent of new 2-D materials like graphene.

Another research area which has remained totally unexplored is very small scale illumination of structures where the illumination length is smaller than the wavelength of electrons in that material. Plasmonics can result in deep sub light wavelength focusing of optical fields. Experiments have resulted in and proposed plasmonic focusing devices with focusing down to 10 *n*m[3, 13]. It is clear that the use of long coherence length materials in conjunction with state of the art plasmonic structures would allow experimental demonstration of opto coherent electronic devices. This dissertation predicts new phenomena that occurs at this illumination length scale.

One objective of current research proposal is to investigate how the coherent optoelectronic properties of a semiconducting material or device structure change with scale of illumination when the illumination scale is similar to the Bloch wavelength of electron in that material. This dissertation proposes novel coherent optoelectronic phenomena and devices using nano-scale illumination of 2-D materials. We report four predictions in this thesis. The first of these is that optical absorption is illumination length dependent. Here from fundamental calculations we show that, at very small scale illumination (length of illumination is comparable with the Bloch wavelength of electrons), the optical absorption of graphene nanoribbon (GNR) is not length independent. We show how the long-scale illumination length optical absorption result emerges as the illumination length increases. The second prediction is a current direction switching photodetector (CDS-PD), in which the direction of current in the external circuit is

dependent on the wavelength of incident light. We show that this behavior comes from the quantum interference of electrons in multiple paths. The third prediction is a Mach-Zhender interferometer photodetector (MZI-PD) in graphene nanoribbon, where coupling light between two resonant peaks of Mach-Zhender interferometer (MZI) structure permits this structure to act as an efficient, small, p-n junctionless PD. The fourth device is a tunable GNR spectrometer, which detects and distinguishes light of different frequencies.

CHAPTER 2

ORIGIN AND HISTORY OF THE PROBLEM

The objective of this research is to make pioneering studies in opto coherent electronics. We have investigated how the coherent optoelectronic properties of a semiconducting material or device structure change with length of illumination when the illumination length is approximately the Bloch wavelength of electron in that material and proposed novel coherent optoelectronic phenomena and devices for nano-scale illumination of structure. We have performed our research and investigation on both a general 1-D two band material structure and on graphene nanoribbons. The 1-D model is evidence of the universal nature of the discoveries in this dissertation. The phenomena are expected to be observable in many 2-D materials. The GNR application was studied because of the advanced state of graphene experimental work make it a likely target for experimental investigation. In our research we have investigated illumination length dependent optical absorption of a material, a photodetector in which direction of current switches depending on frequency of incident light, the optoelectronic properties of MZI GNR structure and a GNR spectrometer.

First I describe what is meant by coherent optoelectronics. The Schrodinger equation is a wave equation for electrons. The dynamics of the electron wavefunction with a given wave vector and frequency is determined by the solution of Schrodinger equation. The propagation of this wavefunction in a medium is called coherent if by knowing the amplitude and the phase of the wave at a certain time and at a certain place we can predict the amplitude and phase of the wave at all other times and space points.

If the medium in which the electrons propagate possesses scattering centers that have some temporal dynamics and all the information about the scattering centers are not known but rather their statistical properties are known, then we do not know all the information about the scattered electron wave. Then it is said that the electron has gone through a phase breaking mechanism or dephasing mechanism. The interaction of electron with light is also one kind of scattering. The interaction is coherent if after

interaction with light, electron retains its phase information. We are interested in the regime where electron wave function evolves in a coherent manner during and after interaction with light.

The electron photon interaction may happen in a closed system. In this model electrons in a finite materiel interact coherently with light. Closed systems are relatively easy to study with lasers. The electron photon interaction may occur also in an open system, where the photoexcited electron can escape from the finite material into leads and also photoexcited holes can be replenished by electrons from leads. We are interested in the open system because we are interested in applying bias across the leads or measuring photocurrents leaving the system.

Now a few words about the wonder material, graphene[14]. Graphene is a single layer of carbon atoms arranged in a honey-comb lattice structure. Geim and Novoselov received the 2010 Nobel prize in physics for "groundbreaking experiments regarding the two-dimensional material graphene"[15]. Graphene has attracted much attention from researchers because of its exceptional electronic, mechanical and optical properties such as high electrical mobility, high thermal conductivity, high mechanical strength, linear energy dispersion around the Dirac point and strong light absorption from near-infrared to visible wavelength ranges[4, 5, 6]. Another amazing thing about graphene is that quantum effects are observed in room temperature[16]. This is why almost all our computations have been performed with graphene as the underlying material. Graphene exhibits ballistic electron transport over unusually large lengths[2, 7, 8, 9, 10]. Researchers have recently measured momentum relaxation length of 10 μm in graphene nanoribbons at room temperature[2]. Up to this length, resistance is independent of length and Ohm's law does not describe transport[11]. Researchers have also demonstrated a phase coherent length of 1 μm at low temperature ($4^{\circ}K$)[8] and 50 nm at $100^{\circ}K$ [12]. Berger et al. expect to see a phase coherent length of 100 nm at room temperature[8] and from the experimental results of Minke et al., a phase coherent length of 10-30 nm at room temperature[12] can be extrapolated. Phase coherent length means up to this length electrons keep their phase coherent wave nature and interference

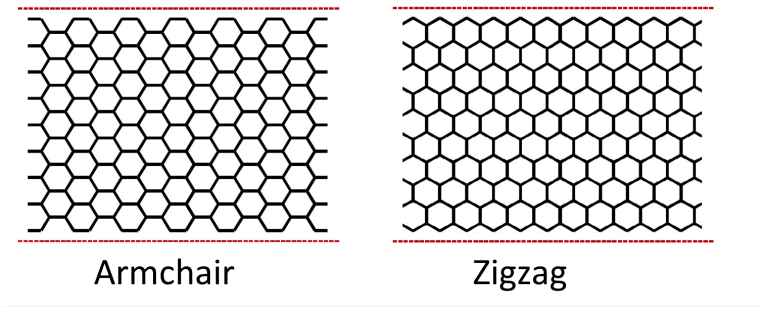

Figure 1. Graphene nanoribbon

phenomena can be observed[8, 11].

In the previous paragraph, we looked at coherent length of graphene in ground state. Now we look at carrier dynamics in graphene after photoexcitation. Using a 7-fs pump pusle, Breusing et al. found an intraband carrier-carrier relaxation time of 30 fs and phonon-mediated intraband cooling of electrons and holes on a 100 fs time scale in graphite[17]. Breusing et al. also showed ultrafast carrier equilibration within the first 250 fs that is primarily governed by electron-electron scattering in a single graphene layer[18]. Dawlaty et al. measured a fast relaxation transient in the 70-120 fs range and then a slower relaxation process in the 0.4-1.7 ps range in epitaxial graphene[19]. The slower relaxation time is found to be inversely proportional to the degree of crystalline disorder in the graphene layers. They relate the measured fast and slow time constants to carrier-carrier and carrier-phonon intraband and interband scattering processes in graphene. Wang et al. found an average phonon lifetimes in the 2.5-2.55 ps range in graphene[20]. Sun et al. found electron-acoustic phonon scattering in the time scale of 1 ps for highly doped layers and 4-11 ps in undoped layers[21].

Bulk graphene is a wonder 2-D material. But if now we restrict the width along one dimension, bulk graphene becomes a nanoribbon. Depending on the configuration of atoms along the edge in the longitudinal direction as shown in Figure 1, a graphene nanoribbon (GNR) can be described as either armchair-edge or zigzag-edge.

In spite of remarkable electronic and optical properties, the absence of electronic band-gap in bulk graphene restricts its application in digital electronics and optoelectronics. Armchair graphene nanoribbons can have an electronic band-gap because of

wavefunction confinement in transverse direction.

Now we review previous work on the optical absorption of GNR. In the literature, the researchers have used perturbation theory to calculate the optical conductance of graphene nanoribbons[22, 23, 24], which is expressed as

$$\begin{aligned}\sigma_1(\omega) =& \frac{2\pi e^2}{m_e e^2 \omega L} \sum_{nmk} \left[(E_{n,k}) - f(E_{m,k})\right] |\langle n,k| P_x |m,k\rangle|^2 \\ & \times \delta(E_{m,k} - E_{n,k} - \hbar\omega)\end{aligned} \tag{1}$$

where, e is the charge of an electron, m_e is the mass of an electron, ω is the angular frequency of light, L is the length of the nanoribbon, n and m are indices for bands, k is the index for momentum and $f()$ is the probability of state occupation which follows the Fermi-Dirac distribution.

This expression is valid for infinite length nanoribbon and energy and momentum conservation is imposed through the Dirac delta function which can approximated as a Gaussian broadening function[23]. Though, there is a term, L (length of nanoribbon) in the denominator, this comes for calculation of joint density of states per unit length and not for length of illumination. The matrix element, $\langle n,k| P_x |m,k\rangle$ is independent of length of illumination.

In our research, we have used the non-equilibrium Green's function (NEGF) formalism which is a microscopic theory for describing quantum transport of electron including interactions (phonon, photon and other electrons)[25]. The NEGF formalism with the light interaction in the position basis gives us the ability to theoretically study nano-scale illumination of different lengths of nanoribbon and compute quantities of interest such as photocurrent, optical absorption and quantum efficiency (QE). For our case, the light interaction matrix element, $\langle l| P_x |m\rangle$, where l and m are indices for position, is calculated in the position basis and is dependent on the length of illumination. Also, momentum conservation is not externally imposed but rather comes from within the formulation depending on the length of illumination.

L. E. Henrickson in 2002 showed how the matrix element of light interaction can be expressed in the position basis for the photocurrent calculation in a resonant tunneling double barrier GaAs structure[26]. We have used this method for our computations and

translated the results for 2-D GNR. Guo et al. used NEGF formalism with photon interaction on position basis for the investigation on photoconductivity of single intrinsic carbon nanotubes. Ostovari et al. used the NEGF formalism for simulation of AGNR photodetectors with asymmetric source and drain contacts.

Our work on GNR MZI-PD was inspired by previous work. One device structure whose operation is based on quantum interference and has attracted attention is the resonant tunneling diode (RTD)[27]. Henrickson showed how a double barrier RTD structure in GaAs can be used as a photodetector by coupling light between two resonant longitudinal modes of the RTD structure. In graphene nanoribbons, a Mach-Zehnder interferometer structure gives the same transmittance pattern as that of a resonant tunneling diode for incoming electrons[28, 29, 30, 31]. This means at some energies electrons go through the device with transmittance one and as if there were no barriers because of constructive interference at those energies and at some other energies electrons cannot go through the device at all (zero transmittance) because of destructive interference. Photon assisted tunneling through double quantum walls by spatial Rabi oscillation has also been studied[32, 33]. In our research we investigate for the first time the interaction of light in graphene nanoribbon MZI structure and, specifically, we look at the coupling of light between longitudinal resonant modes for both zig-zag and armchair structures and how this can be used to make a photodetector.

Now, we briefly review previous work on Graphene PDs. Bulk graphene PDs have been studied in detail both theoretically and experimentally[5, 6, 34, 35, 36]. The primary features of graphene PDs are photodetection in wide spectral range from infrared to ultraviolet region, a transit time limited bandwidth of around 1.5 THz and high internal quantum efficiency of 15-30%[5, 6, 36]. Researchers have also shown theoretically armchair graphene nanoribbon (AGNR) PDs with p-i-n structure with QE of 2-6%[37], with asymmetric source and drain contacts with QE of up to 60%[38] and with external electric field with QE of up to 10%[39]. The photocurrent generation mechanisms in graphene photodetectors include the photovoltaic effect, photothermoelectric effect, bolometric effect and phonon drag effect[6].

In the photovoltaic effect, the built-in electric field generated in the junction of p- and n-type graphene is utilized for separation of photogenerated electrons and holes[40]. Researchers have also shown photocurrent generation without bias and p-n junction by utilizing the built-in electric field at the metal-graphene interface[41]. Such a bulk graphene PD has an internal quantum efficiency of around 10% and external quantum efficiency of about 0.2%[42]. Some asymmetry in the valence band and conduction band profile (through p-n junction, metal-graphene interface, gate potential or applied bias) is used to separate the electron-hole pairs before they are recombined to produce net photocurrent in the external leads.

For our research, the CDS-PD uses gate potentials, MZI-PD uses applied bias and graphene spectrometer uses applied bias for net photocurrent generation. Our MZI-QI-PD has peak internal quantum efficiency of 50% and peak external quantum efficiency of approximately 6%. Our CDS-PD has internal quantum efficiency of 50% and external quantum efficiency of about 5%. For single layer bulk graphene PD, external QE can never cross 2.3% because optical absorption is limited to 2.3%.

Experimentally researchers have fabricated very narrow width GNRs and GNR heterojunctions and GNR structures. Chen et al.[1] have synthesized bottom-up 7-13 GNR heterojunctions as is shown in Figure 2(a). Baringhaus et al.[2] have fabricated sidewall graphene nano-ring with 1.6 μm outer diameter attached to graphene leads as is shown in Figure 2(b).

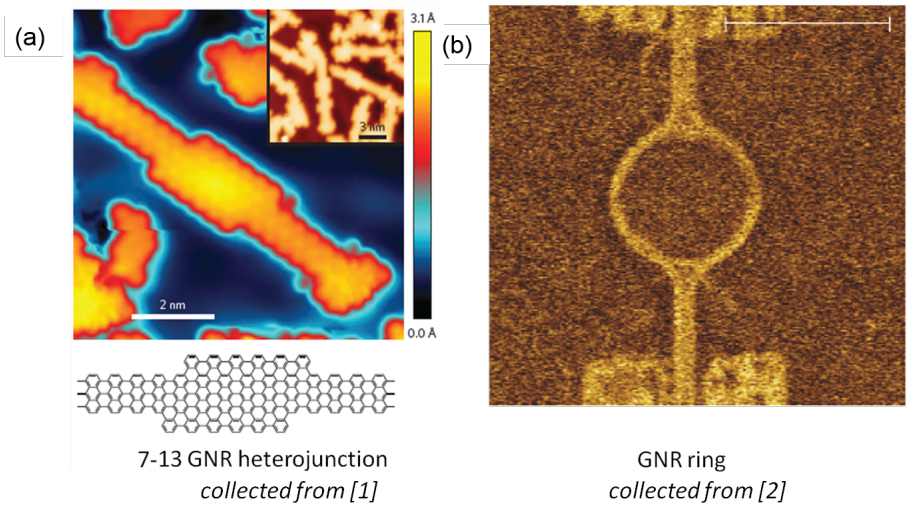

Figure 2. Experimental Graphene nanoribbon structures. (a)7-13 GNR heterojunction[1] (b)GNR ring[2]

For the proposed phase coherent optoelectronic devices we need phase coherent electron transport of around 5-30 *nm* and also hyperfocusing of light in this range. Researchers have recently measured momentum relaxation length of 10 μm in graphene nanoribbons at room temperature[2]. Researchers have also demonstrated a phase coherent length of 1 μm at low temperature ($4^{\circ}K$)[8] and 50 *nm* at $100^{\circ}K$ [12]. Berger et al. expect to see a phase coherent length of 100 *nm* at room temperature[8] and from the experimental results of Minke et al., a phase coherent length of 10-30 *nm* at room temperature[12] can be extrapolated. In the excited state the shortest dephasing time comes from electron-electron scattering which has a value of 30 fs in the most restrictive case. 30 fs results in a phase coherent length of 30 nm considering fermi velocity of graphene as 10^6 m/sec. These experimental results give hope for the creation of new functionality in optoelectronic devices based of phase-coherence of electrons.

Researchers have shown focusing of light to a spot with a diameter down to 1/20 of its wavelength with a coupling efficiency of 10 %[13]. Researchers have been able to create an extreme subwavelength hot spot down to the size of sub-10 *nm*[13]. Researchers have also demonstrated three-dimensional plasmonic nanofocusing of light that converge at a ~10 *nm* apex[3]. So the phase coherence of electrons up to 30 nm at room temperature and hyperfocusing of light in this range is experimentally reachable

as is required for the discovered phenomena and devices in this thesis.

CHAPTER 3

MATHEMATICAL MODEL

3.1 General description of the non-equilibrium Green's function (NEGF) formulation

We have used non-equilibrium Green's function (NEGF) formalism to calculate the current through the device[11, 43, 25, 44]. Here the Green's function, G^R is the impulse response of the device and non-equilibrium means we are in general setting a potential between the leads in order for the current to flow. The Green's function of the device, G^R is calculated from the knowledge of Hamiltonian, H_C of the device and self-energies, Σ_{l1}, Σ_{l2}, Σ_{photon}, Σ_{phonon} and $\Sigma_{electron}$ (leads, photon, phonon and electron) of interaction. This is shown in Equation 2. All calculations are performed in the energy domain and the position basis.

$$[EI - H_C - \Sigma_{l1} - \Sigma_{l2} - \Sigma_{photon} - \Sigma_{phonon} - \Sigma_{electron}]G^R = I \tag{2}$$

We have used nearest neighbor, tight binding model to calculate the Hamiltonian, H_C of the device[45, 46, 29, 47, 30, 48, 28, 49, 38]. If the transfer energy, t is greater than the energy range of interest, then the tight-binding model (the discrete lattice representation) gives fairly accurate results[44, 50]. In the second quantized form, the nearest neighbor tight-binding model has the following form

$$\hat{H}_C = \sum_i \epsilon_i \hat{c}_i^\dagger \hat{c}_i + \sum_{(i,j)} t_{i,j} \hat{c}_i^\dagger \hat{c}_j \tag{3}$$

where $\epsilon_i (= 0)$ is the on-site energy, $t_{i,j} = -t(t = 2.7eV)$ is the transfer energy of the nearest neighbor sites and $\hat{c}_i^\dagger$ and $\hat{c}_j$ are the creation operator and annihilation operator of the π electron at site i and j respectively.

The electron correlation function, G^n and hole correlation function,G^p (equivalent to density matrices) are calculated from the Green's function of the device and scattering functions, Σ^{in} and Σ^{out}.

$$G^n = G^R \Sigma^{in} G^A \tag{4}$$

$$G^p = G^R \Sigma^{out} G^A \tag{5}$$

The scattering functions (Σ^{in} and Σ^{out}) describe the rate at which electrons are scattered in and out at a certain energy level. This can be scattering into the device or out of the device through leads at a certain energy ($\Sigma^{in}_{l1},\ \Sigma^{in}_{l2},\ \Sigma^{out}_{l1}$ and Σ^{out}_{l2}) or scattering from one energy to another energy due to some interactions (Σ^{in}_{photon} , Σ^{out}_{photon}, Σ^{in}_{phonon} and Σ^{out}_{photon}).

We assume a Fermi-Dirac distribution in the leads (f_1 and f_2). Γ_l's are scattering rates provided there are electrons and free states available and Σ_l's are scattering rates considering the availability of electrons and free states through Fermi-Dirac distribution and Pauli exclusion principle.

The scattering functions are calculated in the following way

$$\Sigma^{in} = \Sigma^{in}_{l1} + \Sigma^{in}_{l2} + \Sigma^{in}_{photon} + \Sigma^{in}_{phonon} \tag{6}$$

$$\Sigma^{out} = \Sigma^{out}_{l1} + \Sigma^{out}_{l2} + \Sigma^{out}_{photon} + \Sigma^{out}_{phonon} \tag{7}$$

$$\Gamma_{l1} = i[\Sigma_{l1} - \Sigma^{\dagger}_{l1}] \tag{8}$$

$$\Gamma_{l2} = i[\Sigma_{l2} - \Sigma^{\dagger}_{l2}] \tag{9}$$

$$\Sigma^{in}_{l1} = f_1\Gamma_{l1};\ \Sigma^{out}_{l1} = (1 - f_1)\Gamma_{l1} \tag{10}$$

$$\Sigma^{in}_{l2} = f_2\Gamma_{l2};\ \Sigma^{out}_{l2} = (1 - f_2)\Gamma_{l2} \tag{11}$$

The transmittance, T through the device can be calculated with the following formula

$$T = trace[\Gamma_{l1}G^R\Gamma_{l2}G^A] \tag{12}$$

The effect of light illumination is incorporated in the calculation by the the inclusion of Σ_{photon} term in calculation of Green's function as is shown in equation 2. The electron photon interaction is calculated in the lowest order perturbation theory and self consistent Born approximation [26, 51, 46, 52, 38]. Lowest order means that only single photon (linear) processes are included and self consistent Born approximation means one must iterate until one arrives at a self-consistent electron density at the ground and the excited levels. The electron-photon interaction has the form $H_{elec-photon} = \frac{e}{m_0}A.P$, where A is the vector potential and P is the momentum operator. If we express vector potential, A in the second quantized form, the electron-photon interaction in the

position basis after some manipulation assumes the following form[26]

$$H_{elec-photon} = \sum_{lm} M_{lm}[\hat{b}e^{-i\omega t} + \hat{b}^{\dagger}e^{i\omega t}]\hat{c}_l^{\dagger}\hat{c}_m \tag{13}$$

where

$$M_{lm} = (z_m - z_l)\frac{ie}{\hbar}\sqrt{\frac{\hbar I_{\omega}}{2N\omega\epsilon c}}\,\langle l|\,\hat{H}_c\,|m\rangle \tag{14}$$

where

$$I_w = \frac{Nc}{V\sqrt{\mu_r\epsilon_r}} \tag{15}$$

where l and m are site-basis states. z_m and z_l are the position of site m and site l respectively. $\hat{b}$ and $\hat{b}^{\dagger}$ are the bosonic annihilation and creation operator respectively. I_w is the photon flux in the units of $photons/m^2/sec$, N is the number of photons in control volume, V, c is the speed of light, ϵ_r is the relative permittivity, μ_r is the relative permeability and ϵ is the absolute permittivity.

The scattering functions for photon, Σ^{in}_{photon} and Σ^{out}_{photon} are calculated assuming monochromatic light and two energy levels for excitation.

$$\Sigma^{in}_{lmphoton} = \sum_{pq} M_{lp}M_{qm}[NG^n_{pq}(E - \hbar w) + (N+1)G^n_{pq}(E + \hbar w)] \tag{16}$$

$$\Sigma^{out}_{lmphoton} = \sum_{pq} M_{lp}M_{qm}[NG^p_{pq}(E + \hbar w) + (N+1)G^p_{pq}(E - \hbar w)] \tag{17}$$

$$\Sigma_{photon} \simeq i[\Sigma^{in}_{photon} + \Sigma^{out}_{photon}]/(-2) \tag{18}$$

Knowing the electron and hole density functions (G^n and G^p) and the rate at which electrons are scattered in and out of the device (Σ^{in}_{l1} and Σ^{out}_{l1}), energy resolved current (current per unit energy) is given by

$$I_{en}(E) = \text{trace}\left(\frac{q}{\pi\hbar}(\Sigma^{in}_{l1}G^p - \Sigma^{out}_{l1}G^n)\right) \tag{19}$$

Total current is found by integrating the energy resolved current over the energy range of applied bias.

$$I_{total} = \int I_{en}(E)dE \tag{20}$$

Total inscattering and outscattering (Σ^{in} and Σ^{out}) consist of inscattering from leads and photon (Σ^{in}_{l1}, Σ^{in}_{l2} and Σ^{in}_{photon}) and outscattering from leads and photon (Σ^{out}_{l1}, Σ^{out}_{l2} and

Σ^{out}_{photon}) as is shown in equation 6 and 7. If we want to calculate only the photoexcited part of electron and hole density matrices, then we consider the scattering due to photons only (Σ^{in}_{photon} and Σ^{out}_{photon}). They are given by

$$G^{ph}_{n} = G^{R}\Sigma^{in}_{photon}G^{A} \tag{21}$$

$$G^{ph}_{p} = G^{R}\Sigma^{out}_{photon}G^{A} \tag{22}$$

Energy resolved photoexcited current is given by

$$I^{ph}_{en}(E) = \text{trace}\left(\frac{q}{\pi\hbar}(\Sigma^{in}_{l1}G^{ph}_{p} - \Sigma^{out}_{l1}G^{ph}_{n})\right) \tag{23}$$

It should be mentioned here that we have used tight binding (TB) model for both armchair structure and zigzag structure for GNR MZI photodetector as is described in Section 4.3 . Zig-zag edges of graphene nanoribbon have been shown to be magnetic[53, 54, 55]. Some researchers have used tight binding model without magnetism in NEGF formalism for zig-zag MZI structure[29, 30] and other zig-zag nanoribbon structure[56]. Our device operation is not spin dependent. We have not included the effect of magnetism in our tight binding hamiltonian. But armchair nanoribbon does not have edge magnetism. Therefore, the tight binding hamiltonian without magnetism can be used for armchair nanoribbon without loss of accuracy. Our device operation remains valid for armchair MZI structure and we plan to include the effect of magnetism in our future studies of zig-zag MZI structures.

3.2 Open and closed systems

The electron photon interaction may happen in a closed system. This is shown in Figure 3(a). In this model electrons in a finite material interact coherently with light. This gives rise to famous Rabi oscillation which is shown in Figure 3(b). The electron photon interaction may occur also in an open system which is shown in Figure 3(c), where the photoexcited electron can escape from the finite material into leads and also photoexcited holes can be replenished by electrons from leads.

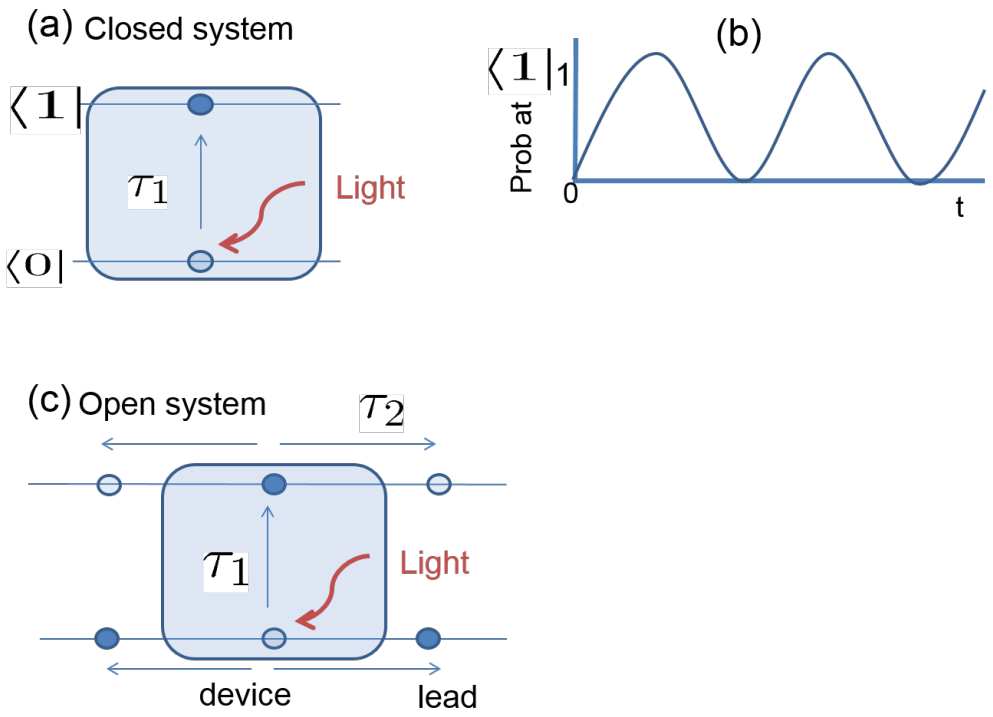

Figure 3. (a) Closed system (b) Rabi oscillation in closed system (c)Open system

There are two lifetimes involved here. One is the lifetime of electron from photoexcitation in either ground or excited state (τ_1) and second is the escape time of the electron into the leads(τ_2). The lifetimes are given by following equations.

$$\tau_1 = \frac{\hbar}{2Im(\Sigma_{photon})} \tag{24}$$

$$\tau_2 = \frac{\hbar}{2Im(\Sigma_{lead})} \tag{25}$$

where $Im(\Sigma_{photon})$ and $Im(\Sigma_{lead})$ are imaginary parts of self energies due to photon and lead respectively.

We are interested in the open system because we are interested in applying bias into the system or photocurrents out of the system.

For the light intensity we are using, $\tau_1 >> \tau_2$. This means once electrons are excited from ground state to excited state, the electrons will leave the device before then can come down to the ground state. Also for the device size envisioed in this thesis (5-30

nm), the dephasing time constants for excited electrons in conduction band[17, 18, 57, 21, 20, 19] are not short enough for the electrons to lose their coherence.

3.3 Optical absorption and quantum efficiency

Knowing the photocurrents, we can calculate optical absorption and quantum efficiency. As shown if Figure 4, I_1 and I_2 are photocurrents in ground state and I_3 and I_4 are photocurrents in excited state. Total photocurrent is $I_1 + I_2$ or $I_3 + I_4$ and net photocurrent is $I_1 - I_3$ or $I_2 - I_4$.

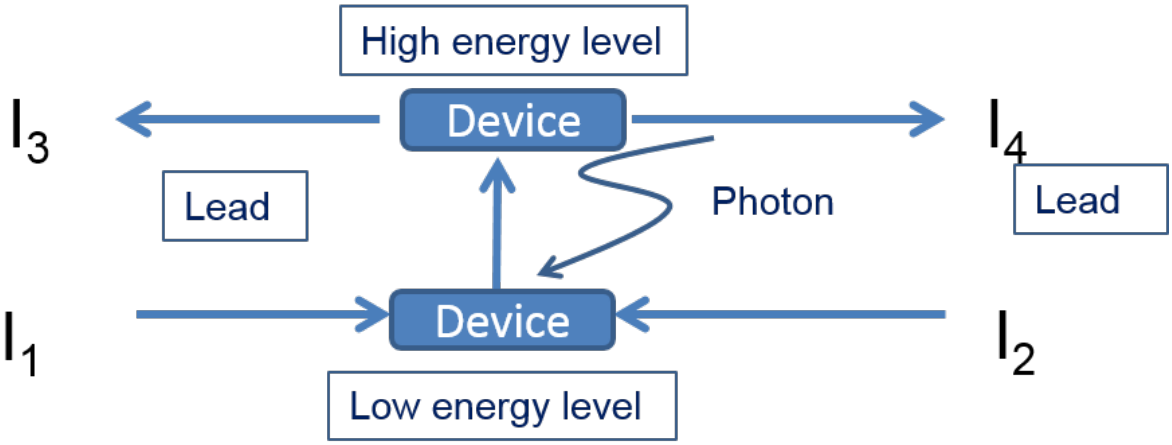

Figure 4. Schematic for photocurrents in ground and excited states

Knowing total photocurrent and net photocurrent, optical absorption and quantum efficiency are calculated as shown below

$$\text{Optical absorption} = \frac{\text{total photocurrent in either ground or excited state/q}}{\text{no of photons in the illuminated area per second}} \tag{26}$$

$$\text{Quantum efficiency (QE)} = \frac{\text{net photocurrent in either lead/q}}{\text{no of photons in the illuminated area per second}} \tag{27}$$

3.4 Electron-phonon interaction

We have included the effect of elastic dephasing due to phonons in this thesis. The motivation is to see how the coherence of electron is lost with phonon dephasing. The

self energy for phonon and scattering function for phonon are found using the following relationships[11]

$$\Sigma_{phonon} = D \times G^R \tag{28}$$

$$\Sigma^{in}_{phonon} = D \times G^n \tag{29}$$

$$\Sigma^{out}_{phonon} = D \times G^p \tag{30}$$

D is the parameter for the strength of phonon interaction. Phonon interaction comes as a scalar potential in the Schrodinger equation. The elements of matrix D represent the correlation between the random potential U_R at location i and location j

$$D_{ij} =< U_{Ri} U_{Rj} > \tag{31}$$

Two cases are of interest.

•**Case 1:** $D_{ij} = D_0$. Here the random potential is well-coordinated throughout the channel having essentially the same value at all points i, so that the every element of matrix D has the same value of D_0.

•**Case 2:** $D_{ij} = D_0$ for $i = j$ and $D_{ij} = 0$ for $i \neq j$.

For case 1, only the phase of the electron is destroyed but for case 2 both the phase and the momentum of the electron is destroyed[11]. In this thesis, we have used case 1, where only the phase of the electron is destroyed.

In order to include the effect of phonon dephasing, the simulations must be done in a self-consistent way. There are there self-consistency loops for phonon dephasing. First, phonon dephasing introduces a scalar potential, Σ_{phonon} in the Schrodinger equation (equation 2) so the greens function, G^R of the device changes. The scalar potential Σ_{phonon} itself is dependent of Green's function of the device as is shown in equation 28, so we need a self-consistency loop here. Second, elastic phonon dephasing also introduces an image of the electron and hole density functions (G^n and G^p) in each energy level as is shown in equations 29 and 30. Electron and hole density functions (G^n and G^p) are in turn dependent on scattering functions of phonon (Σ^{in}_{phonon} and Σ^{out}_{phonon}).

So we need a self consistency loop here. Third, after knowing the electron and hole density functions (G^n and G^p) with phonon interaction in a self consistent way we are ready to calculate the photon interaction. The electron-photon interaction has its own self energy term (Σ_{photon}), which affects the Green's function and its own scattering functions (Σ^{in}_{photon} and Σ^{in}_{photon}), which affects the electron and hole density functions (G^n and G^p). So we need a third self-consistency loop over the two loops already mentioned. The method described in the present paragraph is shown in Figure 5 in a flowchart form.

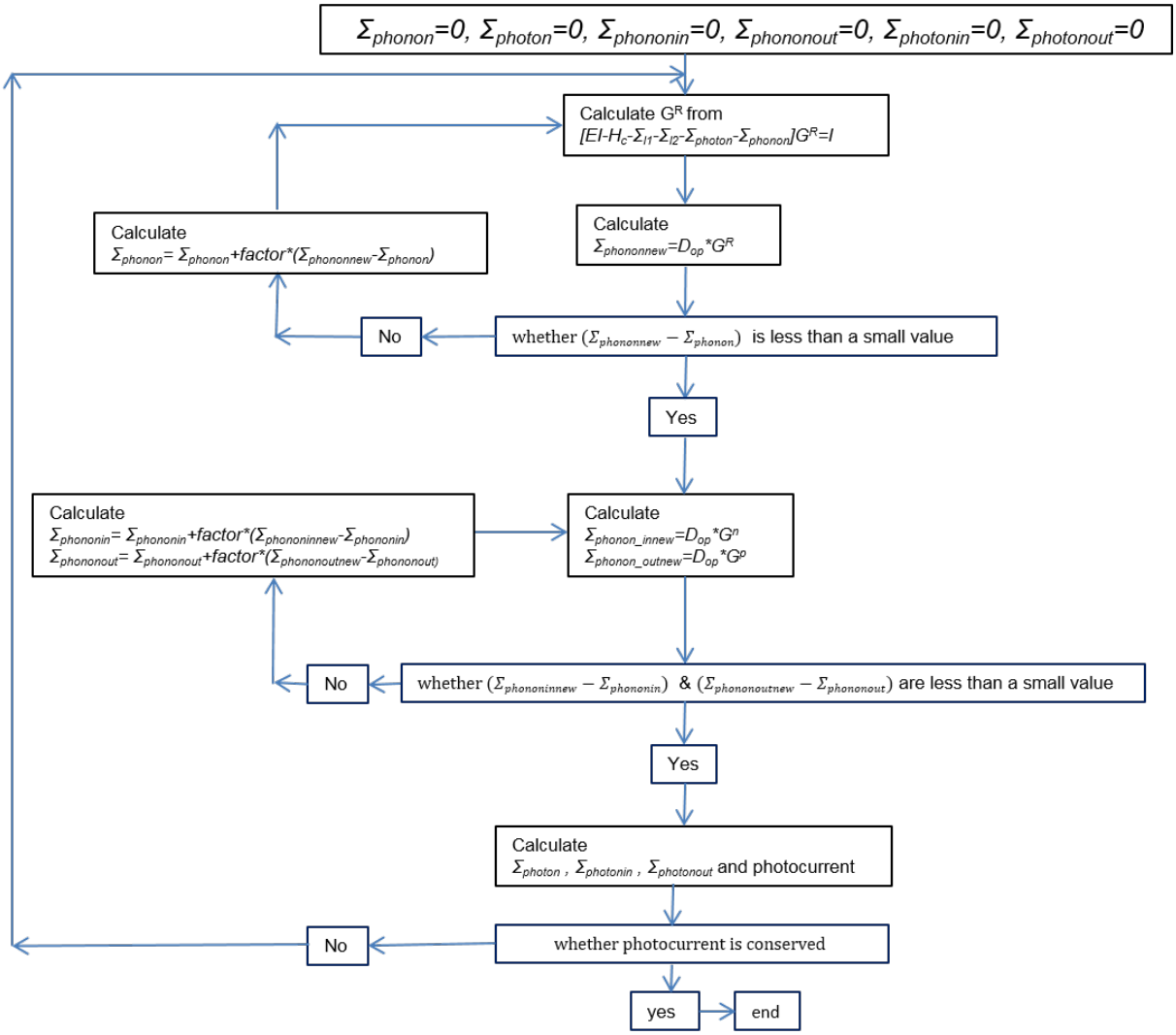

Figure 5. Flowchart for incorporation of elastic phonon dephasing in our NEGF formulation

3.5 Electron-electron interaction

We account for the electron-electron interaction in the system through Hartree potential or Poisson equation. Electron-electron interaction gives rise to a Hartree potential, U(r) which is used in NEGF formulation to find the Green's function of that device (equation 2). In equation 2, $\Sigma_{electron}$ is U(r). Our current direction switching device as is described in section 4.2 is undoped. The effect of gate potential has been taken care of by bending the valence band and conduction band in that part of the device. Since the photoexcited hole and electron density functions are different for each energy level, the total photoexcited electron and hole densities ($n(r)$ and $p(r)$) are found by integrating the electron and hole densities over the energy range. Since electron and hole densities are different, this gives rise to some net charge within the device. So when electrons pass through the device, they will feel some potential. This is the source of Hartee potential. This Hartree potential can be found by solving the Poisson equation as is shown in equation 32 .

$$\nabla^2 U(r) = \frac{e}{\epsilon}(n(r) - p(r)) \tag{32}$$

Here $U(r)$ is the Hartree potential, e is the charge of an electron, ϵ is the permittivity of the material, $n(r)$ is the electron density and $p(r)$ is the hole density.

In matrix form, Poisson equation takes the following form[58, 59]

$$AU = \frac{\Delta^2}{\epsilon}\rho \tag{33}$$

$$\rho = \frac{e[n(r) - p(r)]}{\Delta^3}\Delta \tag{34}$$

where U and ρ are potential and charge density vectors, Δ is length of grid and A is the matrix generated from finite difference method.

The flowchart for finding the Hartree potential, U(r) for each value of photon energy is provided in Figure 6.

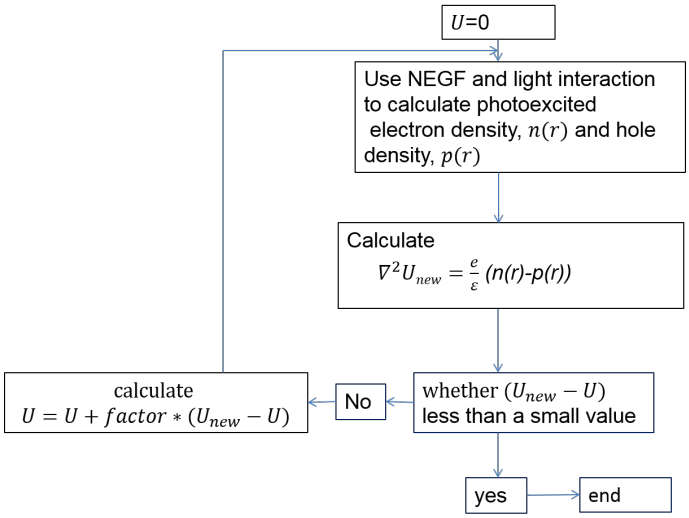

Figure 6. Flowchart for incorporation of electron-electron interaction through Hartree potential in NEGF formulation

We have used 2-D Poisson solver to find the Hartree potential in this thesis. Any graphene nanoribbon has four boundaries. Two boundaries are at the end of device where the device meets the lead and the other two boundaries are at the top and bottom of nanoribbon.

We have performed simulation with both Dirichlet and Neumann boundary conditions. For Dirichlet boundary condition, the potential has a fixed value at the boundary and for Neumann boundary condition the slope of the potential is fixed at the boundary.

3.6 Modeling of semi-infinite leads

In NEGF formalism, the Green's function is calculated using the following equation

$$[EI - H_C - \Sigma_{l1} - \Sigma_{l2} - \Sigma_{photon} - \Sigma_{phonon} - \Sigma_{electron}]G^R = I \tag{35}$$

The effect of leads in the NEGF (Schrodinger equation) is taken into account through the self energy terms Σ_{l1} (lead 1) and Σ_{l1} (lead 2). As with any interaction (light, electron, lead), interaction does two things. One is to change the discrete energy levels (through real part of self energy) and the second is to provide a broadening around the discrete energy levels (through imaginary part of self energy).

There are different methods for calculating lead self-energy like the recursive method, the iterative method and the eigenvalue method[60, 61]. They give equivalent results.

The iterative method is quick and convenient if the problem is formulated in the Green's function formalism[60]. In the iterative methods there are the transfer matrix method and lead decimation method[61]. For our research work, we have used both the lead decimation method and transfer matrix method. They give exactly same result. For all the research work presented in this thesis we have used lead decimation method. The equations involved for the lead decimation method are given below [61].

$$\epsilon_{i+1}^{s} = \epsilon_{i}^{s} + \alpha_i(E - \epsilon_i)^{-1}\beta_i \tag{36}$$

$$\epsilon_{i+1} = \epsilon_i + \beta_i(E - \epsilon_i)^{-1}\alpha_i + \alpha_i(E - \epsilon_i)^{-1}\beta_i \tag{37}$$

$$\alpha_{i+1} = \alpha_i(E - \epsilon_i)^{-1}\alpha_i \tag{38}$$

$$\beta_{i+1} = \beta_i(E - \epsilon_i)^{-1}\beta_i \tag{39}$$

where the initial values are

$$\epsilon_0^s = h_1; \epsilon_0 = h_1; \alpha_0 = u; \beta_0 = u_d \tag{40}$$

here h_1 is the hamiltonian for an unit cell in the lead, u is the transfer matrix between two adjoining unit cells in the lead and u_d is the complex conjugate of the u.

The calculations are done iteratively until α_i is less than a very small value. Knowing ϵ_i^s corresponding to ith iteration when the method converges, G_{00} can be calculated from the following relationship

$$G_{00} = (E - \epsilon_i^s)^{-1}$$

Then the self energy of the leads can be calculated using the following relationship

$$\Sigma_l = uG_{00}u_d$$

Knowing Σ_l, we can find out the Green's function of the system using equation 35.

3.7 Electron-photon interaction matrix element for AGNR

We know that electron-photon interaction comes into Schrodinger equation through interaction potential term, $H_{elec-photon} = \frac{e}{m_0} A.P$, where A is the vector potential of electromagnetic wave, P is the momentum operator for electron, e is the charge of an electron and m_0 is the mass of an electron.

In this section, we show how we have calculated the $\langle l| H_{elec-photon} |m\rangle$ term. The position of four typical atoms in armchair configuration is shown in Figure 7(a) and assumed directions for vector potential and momentum operator are shown in Figure 7(b)

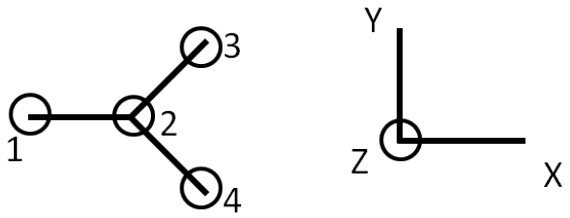

Figure 7. (a) Position of atoms for AGNR. (b)Directions used in the derivation

The interaction potential matrix element in the position basis between elements l and m is shown below

$$\begin{aligned}
\langle l| H_{elec-photon} |m\rangle &= \frac{e}{m_0} \langle l| A.p |m\rangle \\
&= \frac{e}{m_0} \langle l| A_x p_x + A_y p_y + A_z p_z |m\rangle \, (\because p_z = 0) \\
&= \frac{e}{m_0} A_x \langle l| p_x |m\rangle + \frac{e}{m_0} A_y \langle l| p_y |m\rangle \\
&= eA_x \langle l| \frac{p_x}{m_0} |m\rangle + eA_y \langle l| \frac{p_y}{m_0} |m\rangle \\
&= eA_x \langle l| \frac{dx}{dt} |m\rangle + eA_y \langle l| \frac{dy}{dt} |m\rangle \\
&= eA_x \frac{i}{\hbar} \langle l| [\hat{H}_c, x] |m\rangle + eA_y \frac{i}{\hbar} \langle l| [\hat{H}_c, y] |m\rangle \\
&= e\frac{i}{\hbar} (A_x(x_m - x_l) + A_y(y_m - y_l)) \langle l| \hat{H}_c |m\rangle
\end{aligned} \tag{41}$$

For horizontal polarization, $A_y = 0$, so matrix element between 1 and 2 becomes

$$\langle 1| H_{elec-photon} |2\rangle = e\frac{i}{\hbar} A_x a \langle 1| \hat{H}_c |2\rangle \tag{42}$$

For horizontal polarization, the matrix element between 2 and 3 is

$$\langle 2|\, H_{elec-photon}\, |3\rangle = e\frac{i}{\hbar}\frac{1}{2}aA_x \langle 2|\, \hat{H}_c\, |3\rangle \tag{43}$$

These matrix elements have been used for calculation of electron-photon interaction for AGNR. It should be mentioned here that in this thesis we have used horizontally polarized light.

3.8 Justification for the model

•**Nearest neighbor tight binding model:** If the transfer energy, t is greater than the energy range of interest, then the tight-binding model gives fairly accurate result. For graphene, transfer energy, t is 2.7 eV. The narrowest possible graphene nanoribbon is 3-AGNR, which has a bandgap of 2.24 eV. Most of our simulations were done with 7-AGNR, which has a bandgap of 1.27 eV. For a 7-AGNR, 10 nm long CDS-PD device, the current direction switching takes place at around 1.4 eV which is at lower part of the parabolic band of GNR. So tight binding model should give very accurate result.

•**Coherence length:** Recent measurements of the phase-coherence distance have been performed, giving for example a phase coherent length of 1 μm at low temperature ($4^\circ K$)[8], 50 nm at $100^\circ K$ [12] and an expected length of 10-30 nm at $300^\circ K$[12]. These phase-coherence distances are much shorter than the ballistic transport distance in graphene which has been measured to be at least 10 microns in graphene nanoribbons[2]. Our device size is less than 20 nm. So for this device size, we can assume phase coherence at room temperature and ignore the effects like electron-electron and electron-phonon interaction which destroy the coherence of electrons.

•**Electron-photon interaction:** Since the used electron Hamiltonian in this thesis is nearest neighbor, light interaction is also nearest neighbor, that is, after photon interaction electrons can jump to three nearest neighbors for graphene and two nearest neighbors for 1-D chain.

•**Electron-electron interaction:** We account for the electron-electron interaction in the system through Hartree potential or Poisson equation. The potential found in this method due to charge imbalance is very small and has negligible effect on device operation.

In literature, researchers mention an electron interaction time constant of 30 fs [57, 19] for photoexcited carriers in graphene, which considering fermi velocity of graphene as 10^6 m/sce gives a length of 30 nm. That means electrons can travel for 30 nm in excited level (conduction band) before losing their coherence. Our expected device length is 5-30 nm in size.

•**Inelastic and elastic phonon scattering:** Among the inelastic optical phonons the dominant one is at 0.2 eV[57] for graphene. With an applied gate potential of 0.03 eV, our 7-AGNR, CDS-PD device size is around 10 nm in length and low energy electrons (energy around 0.07 eV) take part in current direction switching operation for photon energy of around 1.4 eV. Since these low energy electrons(energy around 0.07 eV) in CB have less energy than 0.2 eV phonon, these phonons cannot affect the electrons.

Also the time constant for optical phonons is 100 fs [18, 19, 20] and has no effect in the length scales of our device.

The time constant for acoustic phonon is in the range of 4-11 ps[21] and has no effect in the length scales, our device is envisioned.

We have shown the effect of elastic phonon dephasing in the CDS-PD device operation. This is done to give a general view of how electron dephasing length affects the device operation.

CHAPTER 4

RESULTS AND DISCUSSION

As we have iterated in the introduction, the objective of current research proposal is to investigate how the coherent optoelectronic properties of a semiconducting material or device structure change with length of illumination when the illumination length is around the Bloch wavelength of electron in that material and to propose novel coherent optoelectronic phenomena and devices for nano-scale illumination of structure. We report four basic contributions in that regard.

- Illumination length dependent optical absorption of GNR
- GNR current direction switching photodetector (CDS-PD)
- GNR Mach-Zehnder interferometer photodetector (MZI-PD)
- GNR coherent spectrometer

4.1 Illumination length dependent optical absorption in graphene nanoribbon

Bulk graphene does not have band-gap. But it has optical absorption of 2.3% from near infrared to far ultraviolet region due to linear energy dispersion relationship around the Dirac (K) point. The E-K diagram for bulk graphene using the 1st nearest neighbor TB model is shown in Figure 8(a). Since bulk graphene has two atoms per unit cell, it gives rise to two bands. They are valence band and conduction band. The E-K diagram along one direction only (y direction) is shown in Figure 8(b). Bulk graphene has famous linear energy dispersion around the K point which gives the electrons the mass-less behavior like the linear E-K relationship of mass-less photons.

If we restrict bulk graphene along one dimension, bulk graphene becomes nanoribbon. Graphene nanoribbon can be of zigzag edge or armchair edge type depending on the configuration of atoms along the edge. From the band diagram it is found that zigzag graphene nanoribbons are always of metallic type, ie, there is no band-gap for zigzag

nanoribbon. But armchair graphene nanoribbons (AGNR) can be either metallic or semi-conducting depending on number of atoms in the transverse directions. AGNR has three typical families corresponding to N=3p, 3p+1 and 3p+2, where N is the number of atoms in transverse direction and p is any positive integer. If p is odd and N=3p+2, then this particular AGNR becomes metallic. For all other cases the AGNR is semi-conducting. In Figure 9 we show the band-diagram and energy transmittance pattern for semiconducting 7-AGNR. The band-diagram has been calculated using 1st nearest neighbor TB Hamiltonian and transmittance has been calculated from NEGF formalism with the same 1st nearest neighbor TB Hamiltonian. 7-AGNR means there are 7 atoms along the width of the armchair graphene nanoribbon. For 7-AGNR, the unit cell has 14 atoms. So in the E-K diagram, there are 14 bands (7 valence bands and 7 conduction bands). If we look at the transmittance diagram we see that, 7-AGNR has a band-gap of 1.27 eV around zero (0) energy and as energy is increased in the valence or conduction band, the transmittance increases as more transverse bands come into conduction and then transmittance decreases and comes to zero.

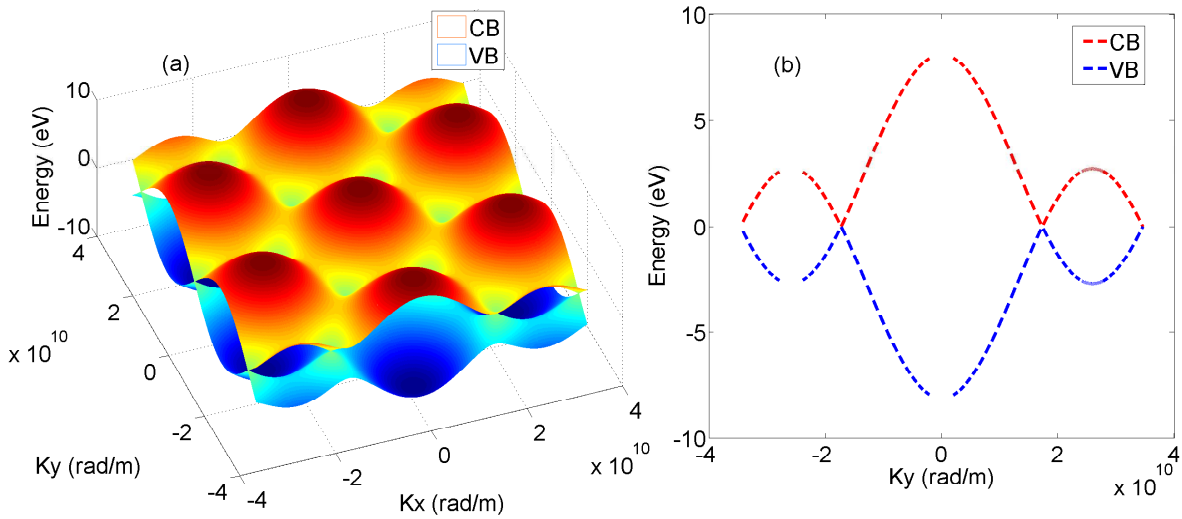

Figure 8. E-K diagram for bulk graphene with nearest neighbor tight binding model (a)2-D (b)along y axis.

As we described in Chapter 2, in the literature, the researchers used perturbation

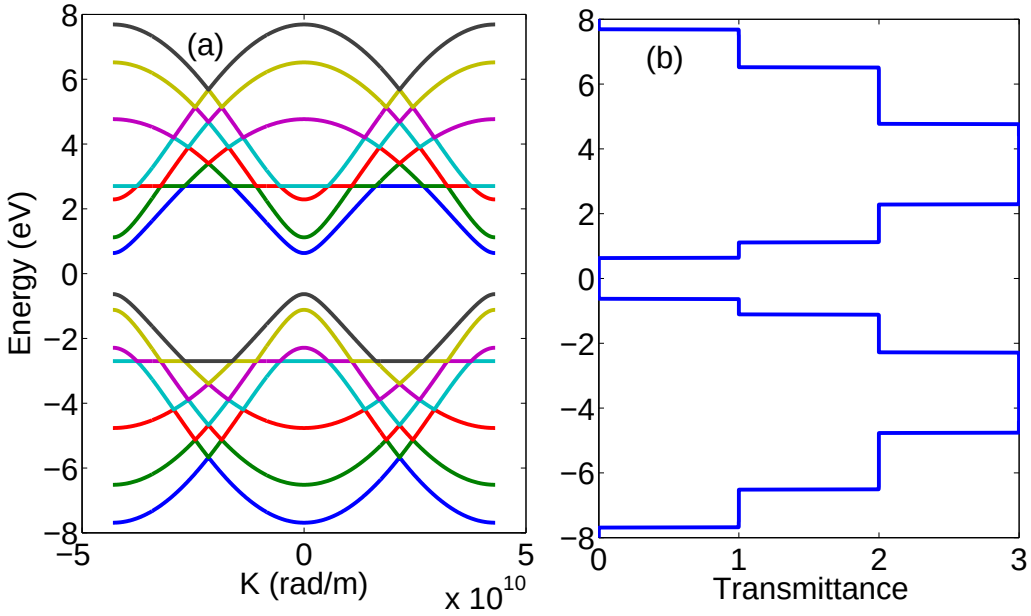

Figure 9. (a) E-K diagram and (b) energy-transmittance diagram for 7-AGNR (semiconducting with a band-gap of 1.27 eV).

theory to calculate the optical conductance of graphene nanoribbon[22, 23, 24, 62].

$$\sigma_1(\omega) = \frac{2\pi e^2}{m_e^2 \omega L} \sum_{nmk} [f(E_{n,k}) - f(E_{m,k})] \, |\langle n,k| P_x |m,k\rangle|^2 \times \delta(E_{m,k} - E_{n,k} - \hbar\omega) \tag{44}$$

where, e is the charge of an electron, m_e is the mass of an electron, ω is the angular frequency of light, L is the length of the nanoribbon, n and m are indices for bands, k is the index for momentum, $f()$ is the probability coming from Fermi-Dirac distribution.

This expression is for infinite length nanoribbon and momentum conservation is imposed through the Dirac delta function which can be approximated as a Gaussian Broadening function[23]. The term L in the denominator comes for calculation of joint density of states per unit length. The matrix element, $\langle n,k| P_x |m,k\rangle$ is independent of length of illumination.

On the other hand, the NEGF formalism with light interaction in the position basis gives us the ability to theoretically study nano-scale illumination of different lengths of nanoribbon. For our case, the light interaction matrix element, $\langle l| P_x |m\rangle$, where l and m are indices for position, is calculated in position basis and is dependent on length of illumination. Also momentum conservation is not externally imposed but rather comes

from within the formulation depending on the length of illumination.

4.1.1 Results and discussion

The optical absorptions for different photon energy for 15-AGNR and 7-AGNR are shown in Figure 10. The results match quite closely the already published results[24]. In the high photon energy region away from the band-gap, the results match more closely, because for these photon energies the device illumination length is more than the Bloch wavelength of electron. If we look at optical absorption pattern with photon energy, we see a number of peaks corresponding to highest lying VB to lowest lying CB in energy, the second highest lying VB to second lowest lying CB and so on. For this result we have illuminated 25 unit cells (10.508 nm) for 15-AGNR and 30 unit cells (12.638 nm) for 7-AGNR. For the calculation, the electron energy interval used was 0.01 eV and the photon energy interval used was 0.01 eV.

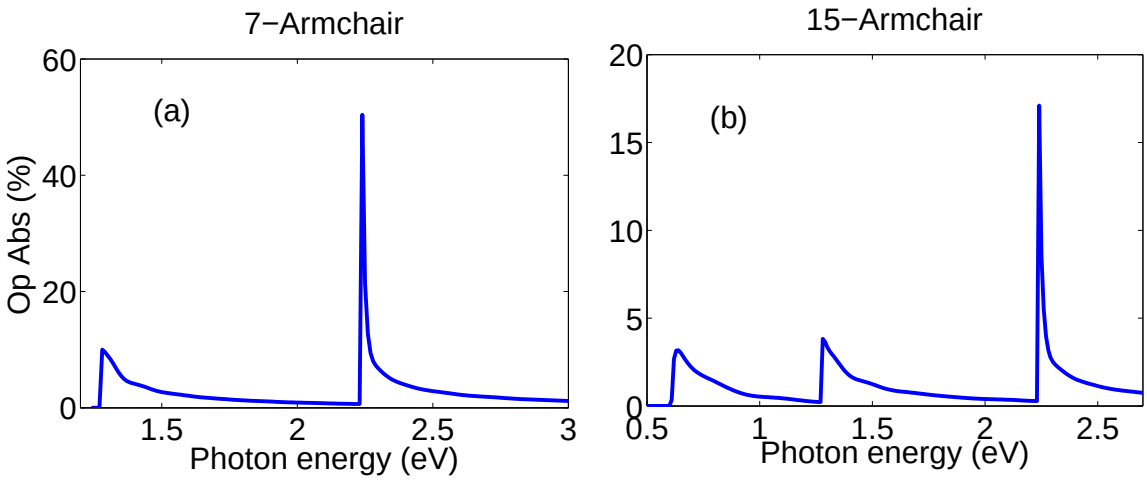

Figure 10. Optical absorption vs. photon energy for (a) 7-AGNR (b) 15-AGNR.

The main result of this section is how the optical absorption varies as we change the illumination length of an armchair graphene nanoribbon. In Figure 11, we show the optical absorption of 3-AGNR (band gap of 2.24 eV), 7-AGNR (band gap of 1.27 eV) and 15-AGNR (band gap of 0.6 eV) vs. number of unit cells illuminated for several photon energies near the band-gap. In this scale, 30 unit cells is 12.64 nm.

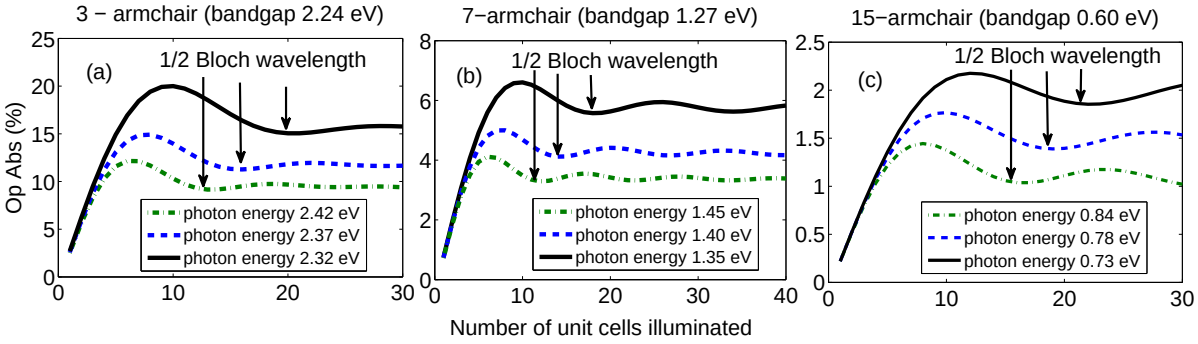

Figure 11. Optical absorption vs. number of unit cells illuminated for different photon energy (a) 3-AGNR (b) 7-AGNR (c) 15-AGNR.

In general optical absorption is small for 1 unit cell and increases rapidly to a peak at a number that corresponds to $\frac{1}{4}$ the Bloch wavelength. The absorption then decays (with damped oscillations) to its macroscopic limit. The Bloch wavelength is thus a suitable approximation for the length at which the long-illumination length optical absorption occurs. It should be noticed that for the same kinetic energy electrons can have different k_x, depending on the width of the nanoribbon. It is reasonable that the optical absorption does not have a meaningful value until the illumination length is larger than the Bloch wavelength of electron. We know that optical absorption is governed by the matrix term $\langle f|\, A.\hat{p}\,|i\rangle$, where, $\langle f|\, and\, \langle i|$ are the final and initial states, A is the vector potential of light and $\hat{p}$ is the momentum operator for electron. In position basis, we have to integrate over at least one full wavelength of electron wavefunction until we come at long-illumination length optical absorption results.

Optical absorption from an initial state to a final state due to electron-photon interaction depends on three factors. First, the density of states in initial and final states, second the photon energy (optical absorption varies inversely with the angular frequency, ω of light) and third, the shape of wavefunction of electron in the initial and final states and polarization of light. The information about density of states is carried in the diagonal elements of electron and hole density matrices. The interaction term, $H_{elec-photon}$ is proportional to $\frac{1}{\sqrt{\omega}}$. Since in the expressions for scattering functions for photon (Σ^{in}_{photon} and Σ^{out}_{photon}), $H_{elec-photon}$ term is multiplied twice (because propagator or green's function

takes electron from one quantum state to another), ultimately, photoexcited electron and hole densities and photocurrent become proportional to $\frac{1}{\omega}$. The information about the wavefunction of the electron is carried both in the diagonal and off-diagonal elements of the density matrices in ground and excited states. We possibly have to satisfy two conservation rules. First is the energy conservation for electron-photon system and second is the momentum conservation. Energy conservation is strictly satisfied. In fact, our numerical method is based on this assumption. The energy difference between initial state and final states of electron is equal to the energy of incident photons. Momentum conservation is not externally imposed in our formalism. It comes within the formalism. Scattering functions for photon (Σ^{in}_{photon} and Σ^{out}_{photon}) contain the term of the density matrix for initial state. Knowing scattering functions for electron we can find out Photoexcited electron and hole densities using the Green's function in the final state. The information about the polarization of light comes through the M term.

In Figure 12, we show the optical absorption of 7-AGNR for different VB electron energies for 5 ,14 and 20 unit cells illuminated. The photon energy is 1.4 eV and the band-gap is 1.27 eV. So, in conduction band, electrons should have a kinetic energy of 0.065 eV. For momentum conserved adsorptions, electrons should make transitions from -0.7 eV in VB to 0.7 eV in CB.

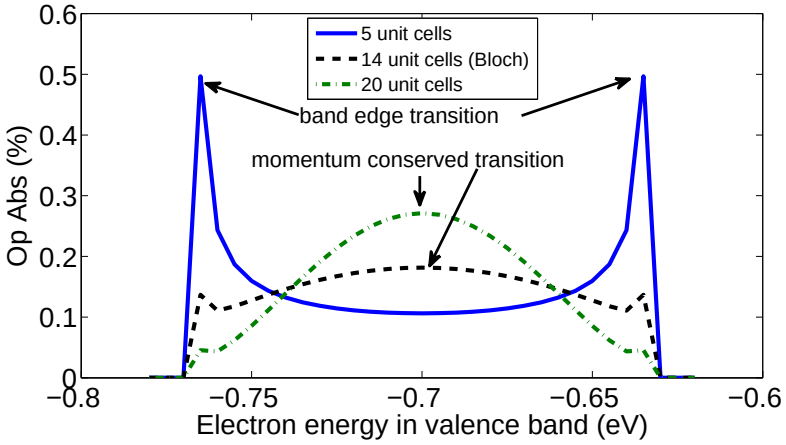

Figure 12. Optical absorption vs. electron energy in VB for different length illuminated for photon energy of 1.4 eV for 7-AGNR.

In Figure 12, we see that when (mainly due to the very high density of states) only

a few unit cells are illuminated, absorption is dominated by very high density of states at the band edges (top of VB and bottom of CB). Then as number of unit cells illuminated is increased momentum conserving electron transitions begin to take place as evidenced by higher optical absorption for those electrons which take part in momentum conserving transitions. Once again this momentum conserving transition takes place for a number of unit cells corresponding to the the Bloch wavelength of the VB electrons. Although experiments contain the total response of all VB electrons, simulations give insight into electron-energy resolved physics that is not available experimentally.

4.1.2 Heisenberg uncertainty principle via optical absorption

In Figure 13, we show the optical absorption for different valence-band electron energies for 25 ,40 and 50 unit cells illuminated for photon energy of 1.49 eV for 7-AGNR. As more unit cells are illuminated, optical absorption takes place at narrower energy range and curves become steeper around -0.745 eV (momentum conserving energy).

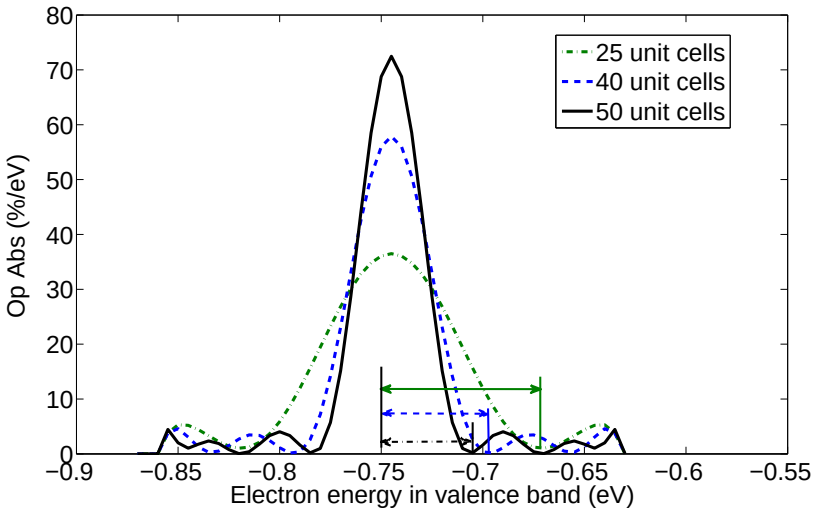

Figure 13. Optical absorption vs. electron energy in valence band for different length illuminated for photon energy of 1.49 eV for 7-armchair.

It is very interesting and fitting that the Heisenberg uncertainty relationship, $\Delta p \Delta x \geq \hbar$ is always satisfied for different length of illuminations in our calculations. The values for Δx, Δp and $\Delta x \Delta p$ for three different lengths of illumination as shown in Figure 13 are shown in tabular form in Table 1. Δp is calculated from the energy difference of

maxima at -0.745 eV and first minima (at any side). Δx is the length of illumination. The values of $\Delta x \Delta p$ as found in our calculation is always greater than $\hbar$ (Planck's constant).

Table 1. Heisenberg uncertainty principle via optical absorption

Δx (m)	Δp (kg-m/sec)	$\Delta x \Delta p$ (joule-sec)
2.1158e-08	5.2089e-26	1.1021e-33
1.6898e-08	6.6956e-26	1.1314e-33
1.0508e-08	1.0955e-25	1.1512e-33

4.1.3 In-depth study of the relationship between optical absorption and Bloch wavelength

The variation of optical absorption with illumination length for illumination length around the Bloch wavelength occurs due to quantum interference of photoexcited electrons in conduction band and photoexcited holes in valence band. The relationship between Bloch wavelength and optical absorption reaching the macroscopic limit is shown through Figure 14. Here 7-AGNR is excited by 1.4 eV light. In Figure 14(a), the variation of optical absorption with illumination length is shown. Optical absorption shows a damped oscillation pattern with illumination length and within one Bloch wavelength the oscillation completes two full cycles. Here the Bloch wavelength is around 26 unit cells of AGNR. The real part of wave-function in 7-AGNR in valence band at -0.7 eV is shown in Figure 14(d). Since photon energy is 1.4 eV, momentum conserved transition takes place from -0.7 eV to 0.7 eV. From Figure14(d), we can see that Bloch wavelength is 26 unit cells. In Figure 14(c), we see that net photocurrent for one sided insertion also completes two full cycles within one Bloch wavelength. Since photocurrent comes from photoexcited electron density and electron density is square value of absolute value of wave-function, within one Bloch wavelength photocurrent completes two full cycles.

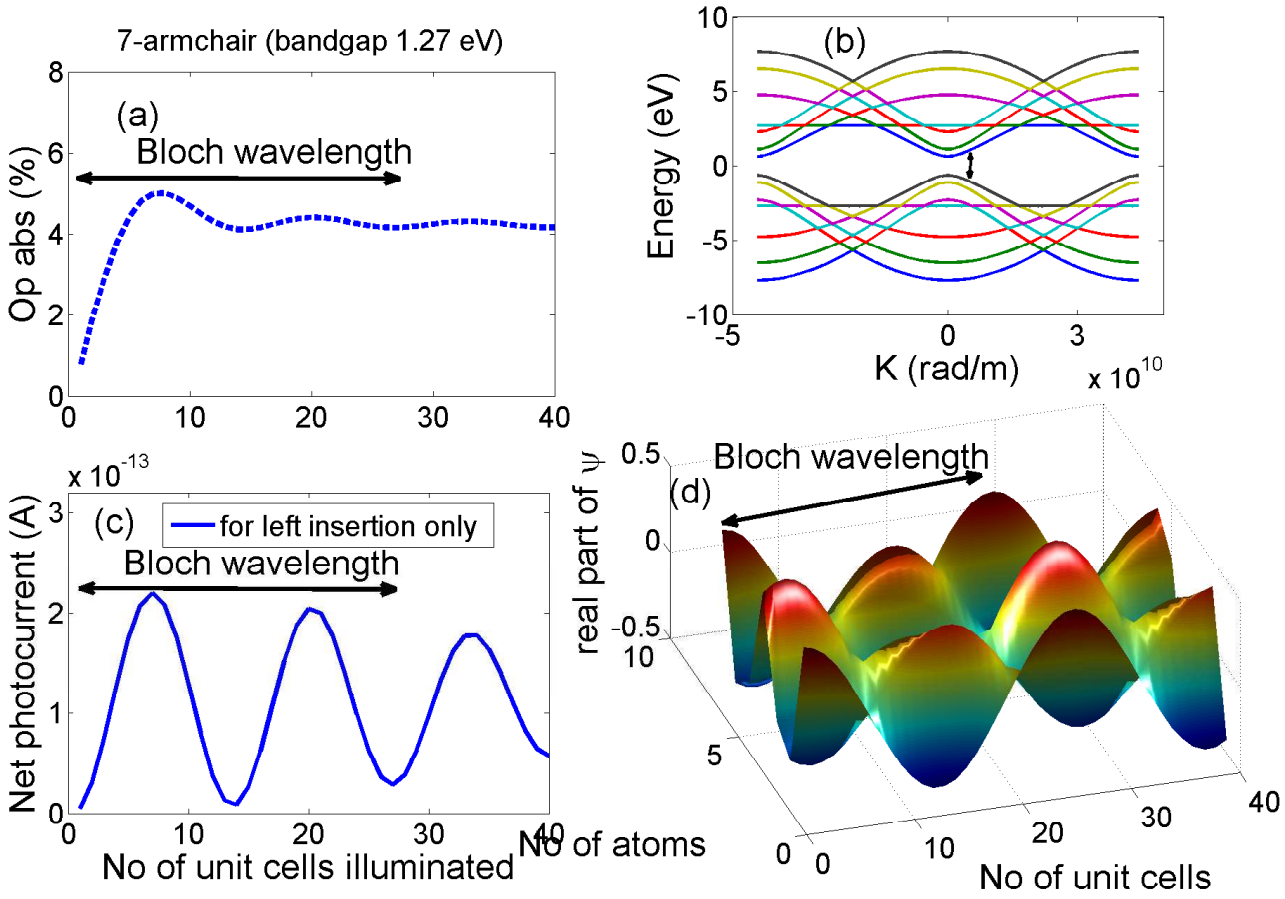

Figure 14. (a) Optical absorption vs. illumination length (b) net photocurrent vs. illumination length (c) band diagram (d) wave function in VB. All results are for photon energy of 1.4 eV and 7-AGNR.

4.1.4 Optical interaction in 1-D two level system

We can explain the origin of damped oscillation in optical absorption with periodic oscillation of the photocurrent for one sided insertion of electrons in VB. One sided insertion means the photoexcited holes in VB are replenished from one lead only. The origin of this periodic oscillation can be best understood with a hypothetical 1-d structure with 2 energy levels in each atomic position. So we digress for a moment and explain the quantum interference for 1-d structure. The 1-d structure with two energy levels per atomic position and the band diagram for the 1-D atomic chain with a bandgap of 2 eV are shown in Figure 15.

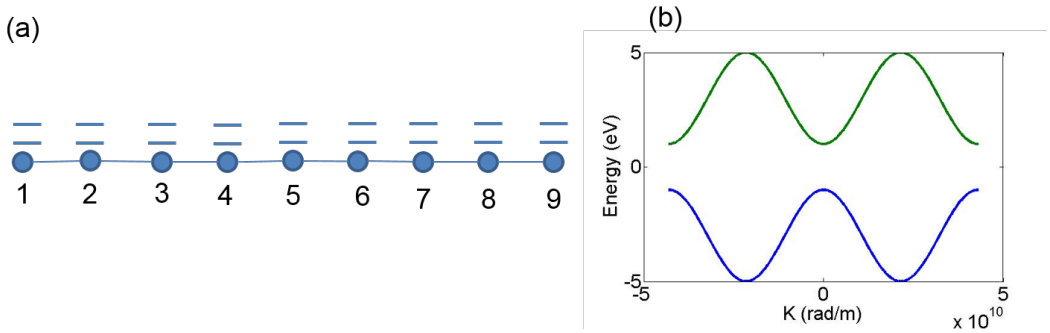

Figure 15. (a) 1-D atomic chain with 2 energy levels per atomic position (b) band diagram for the 1-D atomic chain

The 1-d structure with two energy levels per atomic position and atom 10 excited from nearest neighbors 9 and 11 are shown in figure 16(a). Since atom 10 has been excited only, we see electrons emanate out from position 10. After photoexcitation holes are created in VB and photoexcited electrons in the CB leave the device through leads in both sides . These photoexcited holes in the VB are replenished by electrons from leads in both sides. In the simulation, we can ensure that photoexcited holes are replenished from one side only. This can done by making the probability of availability of electrons in one of the leads as 1 (one) and in other lead as 0 (zero) in all available energy ranges. In Figure 16 the photoexcited holes are replenished by electrons in VB from left side only.

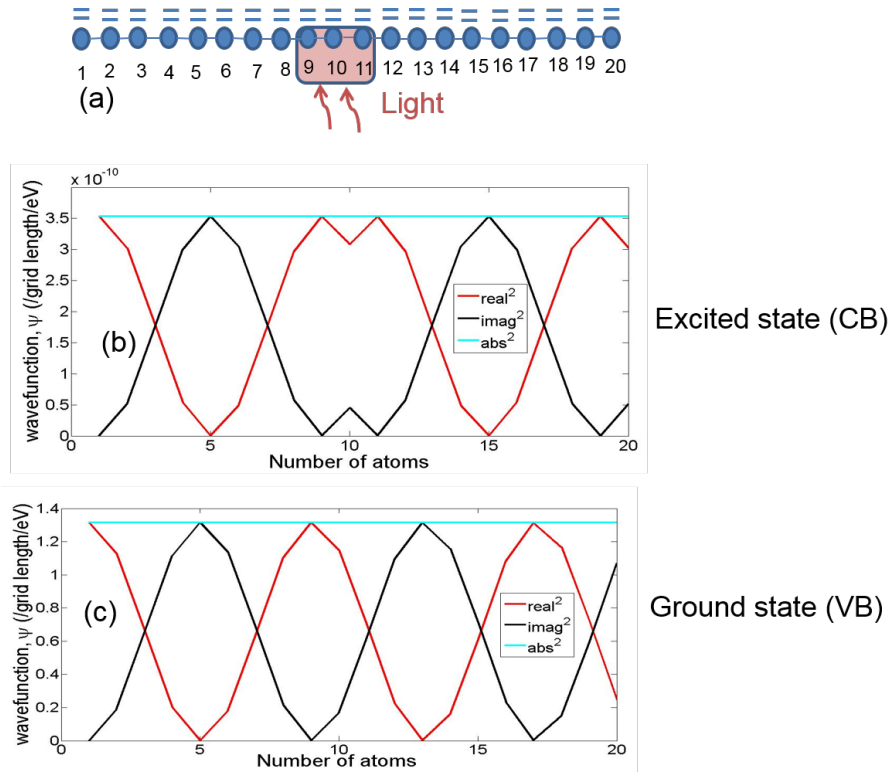

Figure 16. (a) 1-D atomic chain with atom 10 excited (b) wavefunction in excited state for atom 10 excited (c) wavefunction in ground state

Now if all the atoms are excited as has been shown in Figure 17, electron interferes with itself in CB and VB. For one side of the device, electron interferes constructively and for other side for some length electron interferes constructively and for some length electrons interferes destructively. This is shown in Figure 18. Here four curves for currents with illumination length are shown. These are currents in two leads for ground and excited levels. Holes are replenished in VB from left lead (lead 1) only. In left lead (lead 1) in excited level, current rises up quadratically with illumination length. This is because in left lead electron wave-function interferes constructively always with illumination length and electron density is square of absolute value of wave-function and current is proportional to electron density. In right lead (lead 2), current shows a periodic oscillation pattern because for some illumination length electron wave-function interferes constructively and for some illumination length electron wave-function interferes destructively. It should be mentioned here that for the simulation results shown in Figure 18, 2.3 eV light is used and we have considered momentum conserved transition

only for electron (transition from -1.15 eV to +1.15 eV).

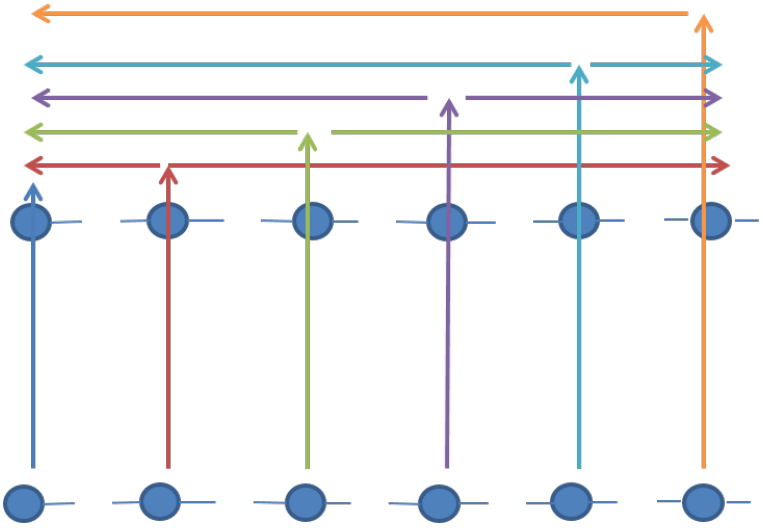

Figure 17. Pictorial diagram showing quantum interference of electron with itself for optical excitation of 1-D two level atomic chain

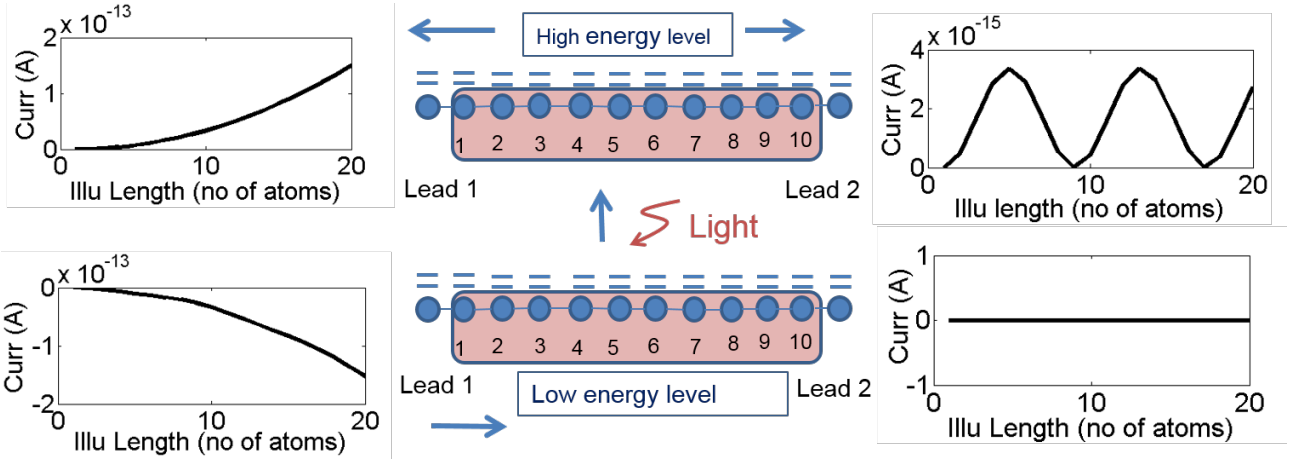

Figure 18. Photocurrent vs illumination length in different leads and ground and excited states for 1-D atomic chain (left insertion only)

4.1.5 Optical interaction and periodic oscillation in photocurrent in AGNR

Now for graphene nanoribbon with photoexcitation the same thing as descried in previous section for 1-d chain of atoms happens. In Figure 19, four curves for currents with illumination length are shown. These are currents in two leads for ground and excited levels. Here holes in the VB are replenished from left side only. In the excited state, we can see that in the left side of the ribbon there is a build-up of wave-function, and in the

right side of device the wave-function is low because for some illumination length the wave-function adds constructively and for some illumination length the wave-function adds destructively. It should be mentioned here for the results shown in Figures 19 and 20, we have integrated the energy resolved current over the available electron energies to get the total current whereas for Figure 18, currents were shown for momentum conserved electrons only.

For right insertion, we get the result as shown in Figure 20. Here the results are same as Figure 19 but the currents have just changed sides.

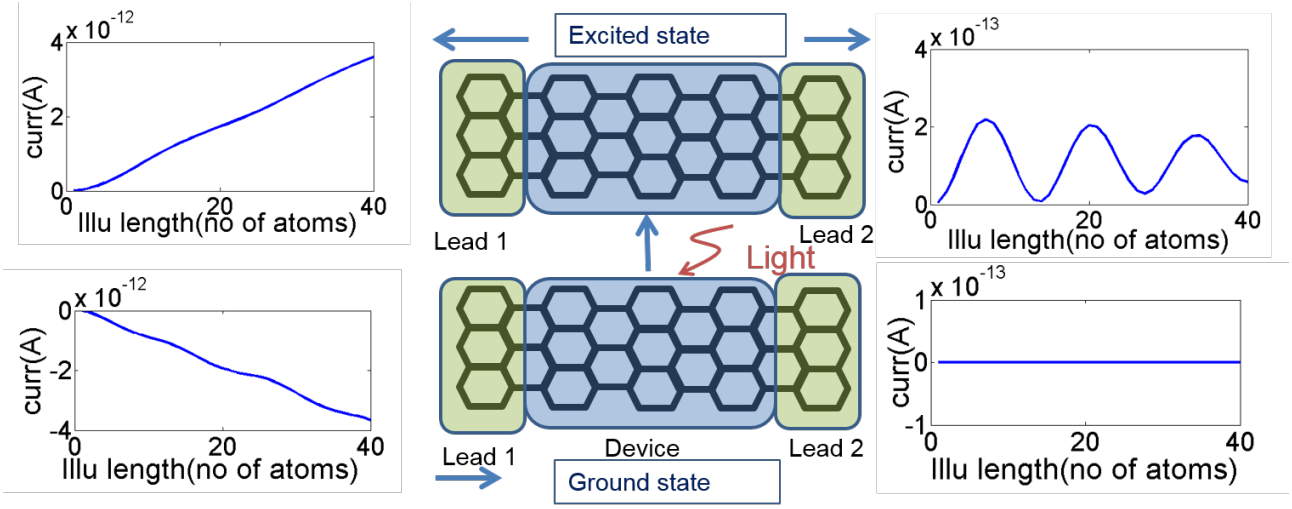

Figure 19. Photocurrent vs illumination length in different leads and ground and excited states for 7-AGNR (left insertion only)

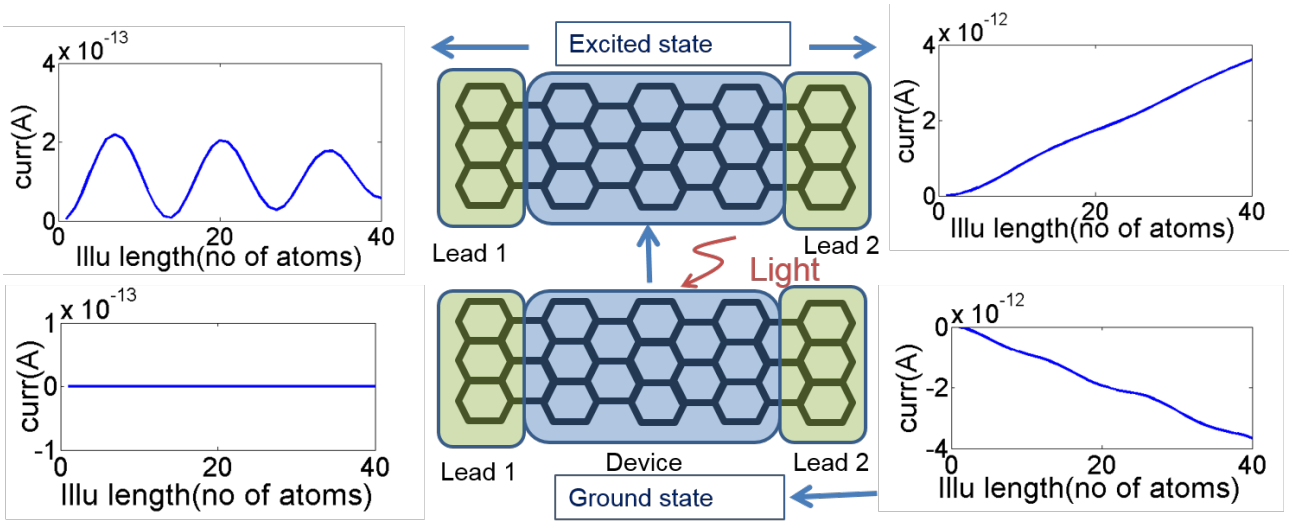

Figure 20. Photocurrent vs illumination length in different leads and ground and excited states for 7-AGNR (right insertion only)

Now if electrons are inserted from both sides, as is the case for real life experimental case (not simulation), we get the result as shown in Figure 21. By summing up the photocurrents in either ground or excited state, we can get the total photocurrent and then can find the optical absorption using equation 26. Then we get the optical absorption pattern with illumination length as shown in Figure 14.

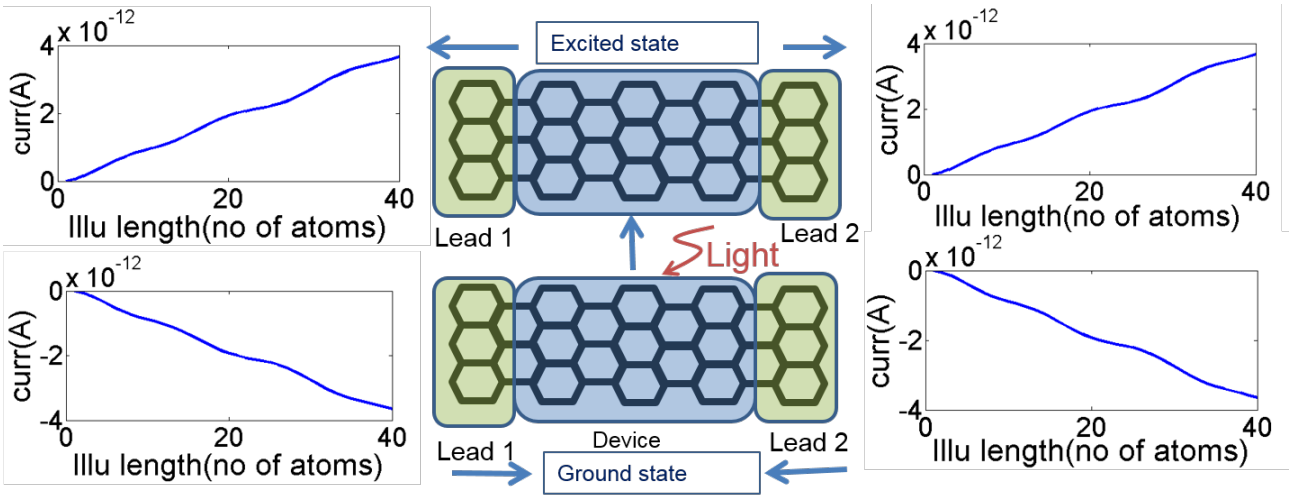

Figure 21. Photocurrent vs illumination length in different leads and ground and excited states for 7-AGNR (insertion from both sides)

In Figures 19 and 20, we have shown currents in leads for ground and excited states as a function of illumination length. Now for a particular illumination length, we can also look at wave-function in ground and excited states. This is shown in Figure 22. The holes in the valence band are replenished from left side only. In Figure 22 (a) (excited state), we see that there is a build up of electrons in left side of the nanoribbon because of constructive interference but in the right side the electron density is low because of constructive interference for some illumination length and destructive interference for some other illumination length. The result shown in Figure 22 is for 7-AGNR with 40 unit cells illuminated with a photon energy of 1.4 eV and only momentum conserved electron has been considered.

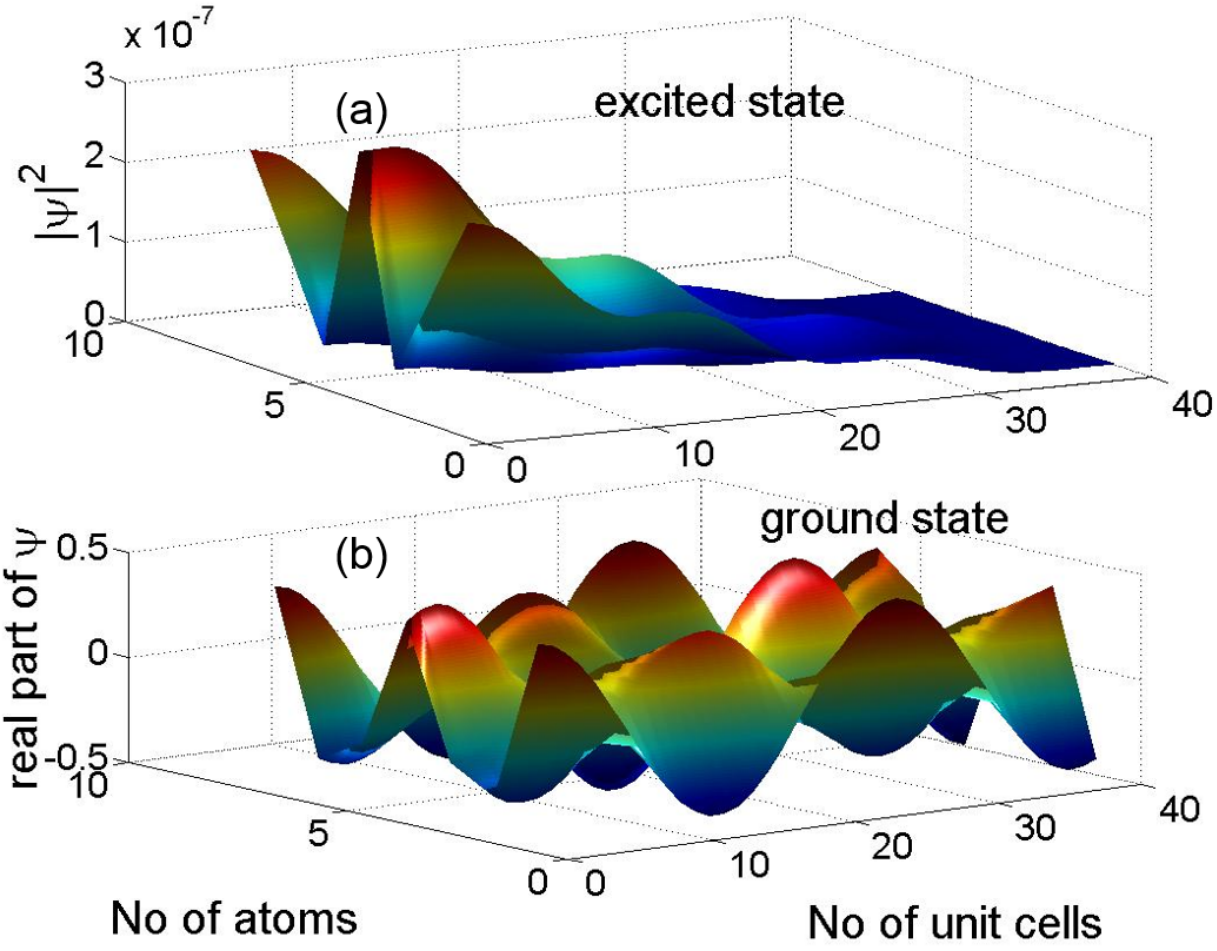

Figure 22. Wavefunction in 7-AGNR with optical excitation (a) excited state (b) ground state (40 unit cells illuminated with a photon energy of 1.4 eV and only momentum conserved electron has been considered)

In this section, we show the results of computation of optical absorption of AGNR as a function of illumination length. We have also shown the results for a 1-D atomic chain and found that this is a generalized result applicable for any material. We find that optical absorption is not independent of illumination length and Bloch wavelength of electron gives a suitable indicator about when the long-illumination length limit optical absorption will begin to occur. This study helps to understand material behavior under extremely small scale illumination (illumination lengths are comparable with the Bloch wavelength of electron) and also paves the way for envisioning novel coherent optoelectronic phenomena and devices.

4.2 GNR current direction switching (CDS) photodetector

Our 2nd invention is a very simple nanoribbon photo-detector structure, in which the photocurrent in the external circuit (leads) changes direction depending on the frequency of incident light. The physical principle behind the phenomenon of direction of current switching is based on quantum interference of photoexcited electrons in multiple paths.

4.2.1 Device structure

The device is simple AGNR. We create a potential well in one half of the device by applying an external gate bias voltage. The device structure is shown in Figure 23. Gate Voltage can be applied through ionic liquid. A negative gate voltage will create positive charges in graphene and will electrostatically pull down the conduction band (CB) and valence band (VB) for electrons in graphene in the position where gate is placed. In NEGF simulation, the pull-down of CB and VB is simulated by adding the negative energy in the diagonal elements of the hamiltonian. It is noticeable here that the active device area is longitudinally asymmetric as is required for photocurrent generation.

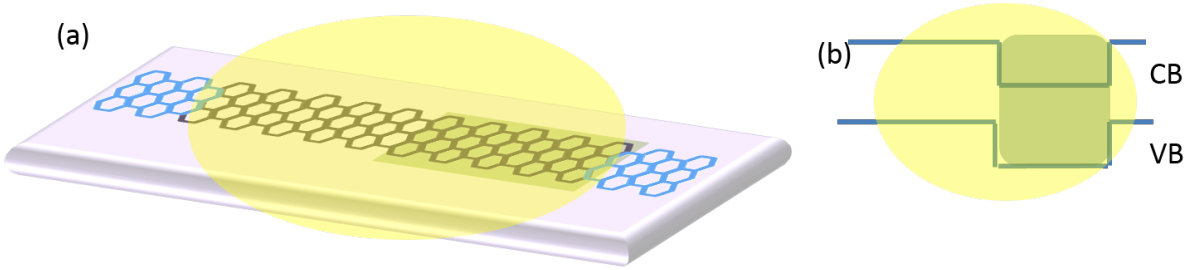

Figure 23. (a)Device structure (lead region blue, device region black, gate region green and illuminated region yellow (b)Band profile for the device

4.2.2 Operating principle

For a conventional p-n junction photo-detector or solar cell, incident light produces electron-hole pairs and then these electron-hole pairs are separated by the built-in potential of p-n junction. Then holes diffuse in the p side and electrons diffuse in the n side to reach the leads. So photo-generated holes are replenished by electrons from the

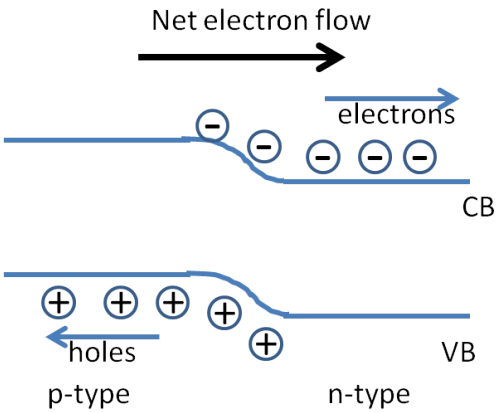

Figure 24. Operation of conventional p-n junction photodetector

leads of p side and photogenerated electrons diffuse out to the leads of n side and a net photocurrent is created. This is shown in Figure 24.

The operations of current direction switching (CDS) PD for low and high photon energy are shown in Figures 25 and 26 respectively. For low photon energy (photon energy is still greater than band-gap energy) the photogenerated electrons in the CB can go to either side. The photo-generated holes in the VB can only go to left side because of presence of potential barrier in right side as is shown in Figure 25. The electron and hole densities at 0.65 eV and -0.65 eV corresponding to photon energy of 1.3 eV(lower photon energy) where CDS phenomenon does not take place are shown in Figure25 (a) and Figure25(c). We have a net electron flow from left to right side. In the convention we use, this gives rise to a negative photocurrent and negative quantum efficiency (QE). For Figure 25, the device is 7-AGNR with 16 cells illuminated with a gate potential (GP) of 0.06 eV.

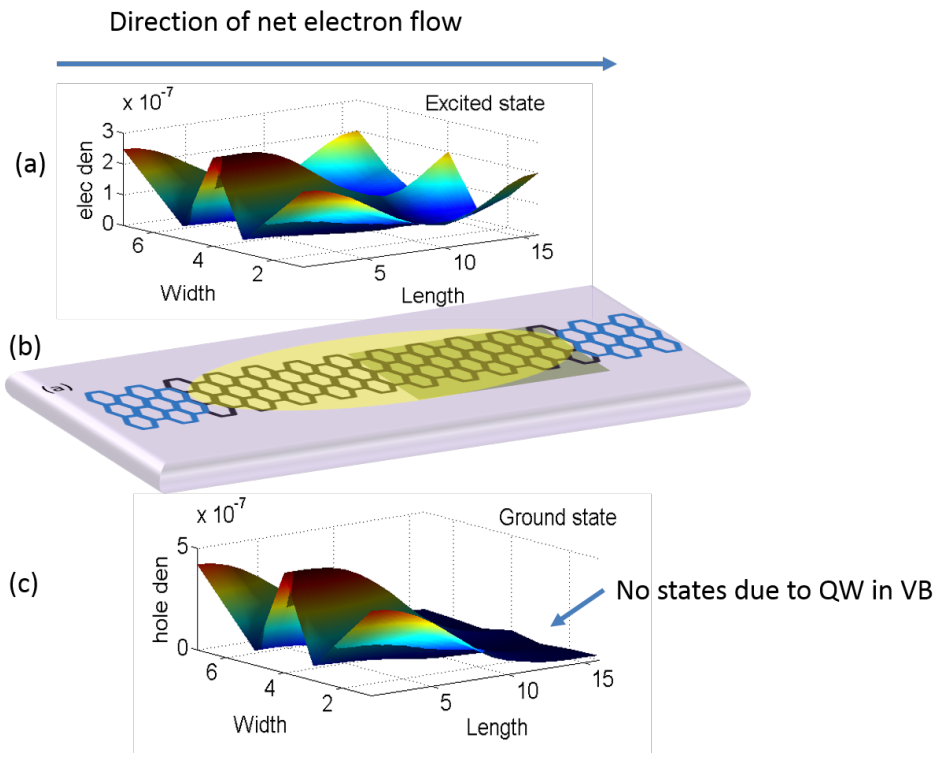

Figure 25. Operation of current direction switching photodetector for low photon energy(a)electron density in excited state (b)device structure (c)hole density in ground state.

For higher photon energy, the photo-generated electrons can go to either side as before and also the photo-generated holes can go to either side as is shown in Figure 26. The electron and hole densities at 0.72 eV and -0.72 eV corresponding to photon energy of 1.44 eV(higher photon energy) where CDS phenomenon takes place are shown in Figure26 (a) and Figure26(c). In the CB (excited state), electron density is higher at left side than right side so there is a net electron flow from right to left. In the VB (ground state), the hole density is higher at right side than left side so there is a net hole flow from left to right (electron flow from right to left). So we see that at this particular photon energy, net electron flow considering both VB and CB is from right to left. In Figures 25 and 26, we have shown electron and hole densities corresponding to momentum conserved case but, of course, to find the photocurrent we have to integrate the energy resolved current over the available electron energies. For Figure 26, the device is 7-AGNR with 16 cells illuminated with a GP of 0.06 eV.

So in conclusion for this section we can say that, at suitable higher photon energies,

because of quantum interference of electrons, under some restrictive conditions (for a particular gate bias, the illumination length is less than a certain length), net electron flow will be in opposite direction than conventional direction and current will switch direction in external circuit.

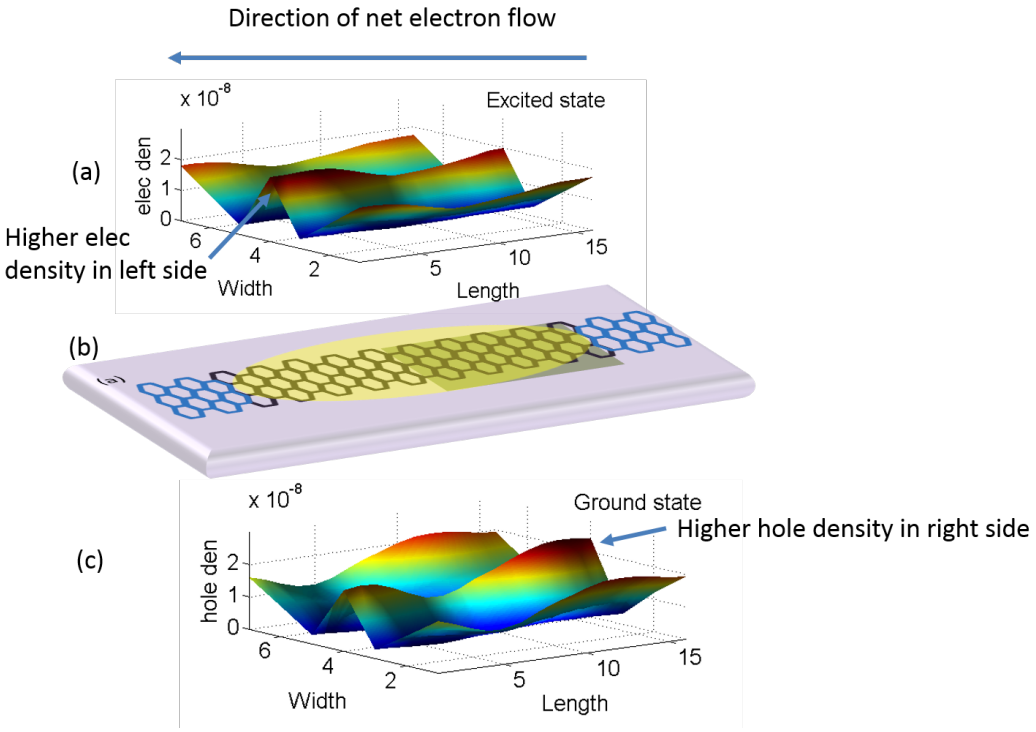

Figure 26. Operation of current direction switching photodetector for high photon energy (a)electron density in excited state (b)device structure (c)hole density in ground state.

4.2.3 Results and discussion

The quantum efficiency (QE) for different photon energy for the CDS photodetector is shown in Figure 27. This result is for 7-AGNR which has a band-gap of 1.27 eV. For lower photon energy (photon energy is greater than band-gap energy), QE is negative. Then at some higher photon energy, QE becomes positive. At still higher photon energy, the QE efficiency becomes negative again and then the whole pattern is repeated when 2nd VB and CB comes into conduction. In Figure 27, the QE shown is for 10 unit cells. For low GP, there is a large positive QE for some photon energies. As GP is increased, this positive QE becomes smaller and at certain GP, the CDS effect is no longer observed.

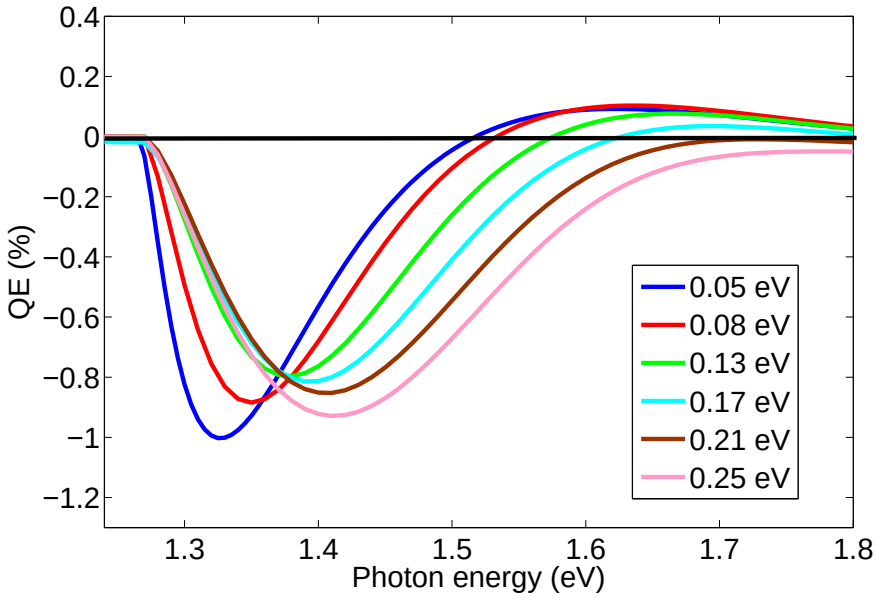

Figure 27. QE vs. photon energy for different gate potential (GP) (Device length 10 unit cells)

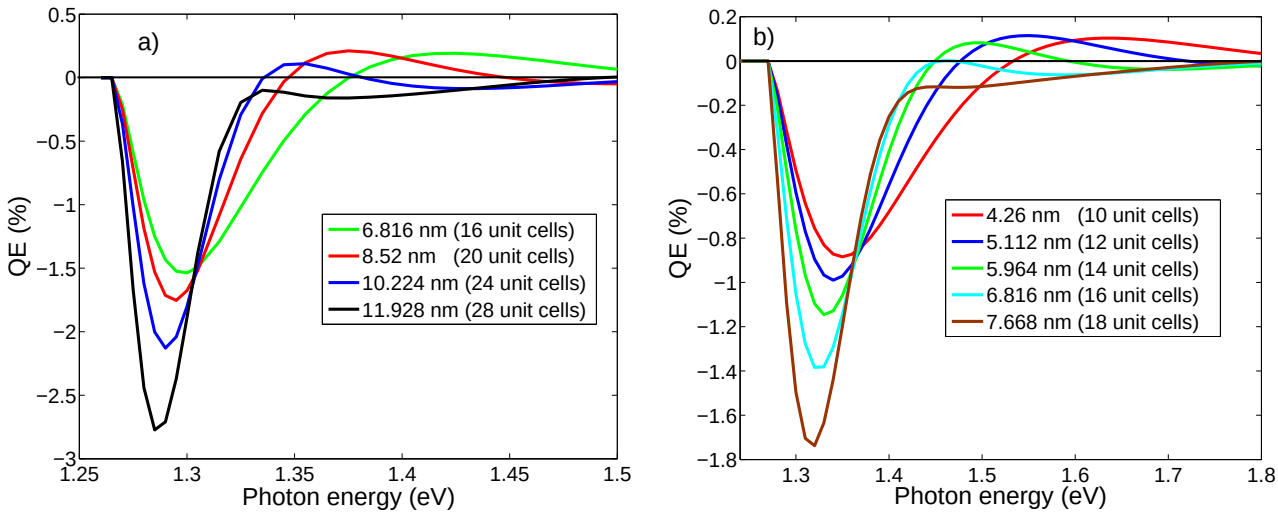

Figure 28. QE vs. photon energy for different device length (a) GP is 0.03 eV (b) GP is 0.08 eV

Alternatively, as the illumination length is increased for certain fixed GP as is shown in Figure 28, at some illumination length, the CDS effect goes away. For Figure 28(a), the applied GP is 0.03 eV and for Figure 28(b), the applied GP is 0.08 eV. In Figure 28(a), we see that the CDS effect is observable at device length of approximately 10 nm

which is experimentally reachable both from electron coherence and light hyperfocusing point of views.

In Figure 29, we show the variation of photocurrent as a function of GP for a particular illumination length (12 unit cells) for various photon energies. For low photon energy, the photocurrent does not have a positive part as GP is varied. As photon energy is increased, at certain photon energy, the positive photocurrent surfaces. For some range of photon energies, photocurrent is positive for a small range of GP. For these photon energies, positive photocurrent will be there as long as GP is smaller than a certain value such that for a particular photon energy, momentum conserved transition is possible for electron(for example, for 1.54 eV of photon energy, the maximum GP that can be applied for observing positive photocurrent is (1.54/2-0.64) eV or 0.13 eV. Then as photon energy is increased more, the positive photocurrent is not visible for any GP.

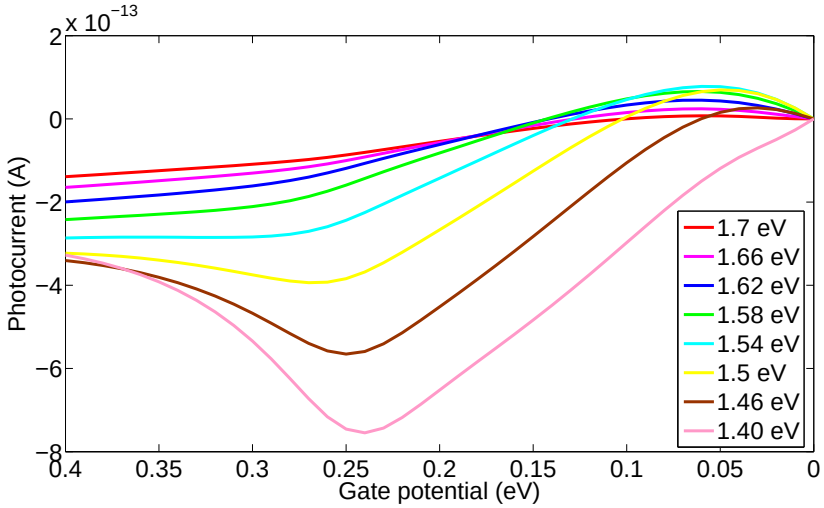

Figure 29. Photocurrent vs Gate potential for various photon energy (length of illumination 12 unit cells)

4.2.4 Explanation of CDS phenomenon with periodic oscillation in photocurrent

If we illuminate a normal AGNR (without any applied gate potential), there will be no net photocurrent. For a particular photon energy, there is an electron energy at which momentum conserved transitions take place (for example for 1.4 eV of photon energy, momentum conserved electron transition is from -0.7 eV to 0.7 eV). If we look at this

electron energy only and further assume photoexcited holes at this energy are replenished from only one side of the lead (let us say, left side), then there will be a net electron photocurrent going from left to right. This photocurrent will have a periodic oscillation with variation of length of illumination. This periodic oscillation has a wavelength which is half the electron Bloch wavelength. Now if the electrons come only from right side in the valence band, the net photocurrent will be from right to left with the same periodic oscillation with length of illumination. These two periodic oscillations will both be present in under practical operating condition (that is, photoexcited holes will be replenished from both the left and right side) and since the periodic oscillations are in step with each other there will be no net photocurrent. Of course, to find the total net photocurrent we have to integrate the energy resolved photocurrent over all the electron energies in the valence band. This integrated net photocurrent also have a periodic oscillation with periodicity of half the momentum conserved electron Bloch wavelength and left to right and right to left going photocurrents are in step with each other and there is no net photocurrent. But the condition changes if we apply a gate potential in part of the device. Now the left to right going electrons in valence and conduction bands do no see the the same potential profile as right to left going electrons. Net photocurrents still have periodic oscillations due to interference but these periodic oscillations are now out of step with each other. So at some illumination lengths, the total net photocurrent (summation of net photocurrents for left and right injections) is from left to right and at some other illumination lengths, the total net photocurrent is from right to left. This has been shown in Figure 30. For a small range of illumination length, CDS phenomenon takes place.

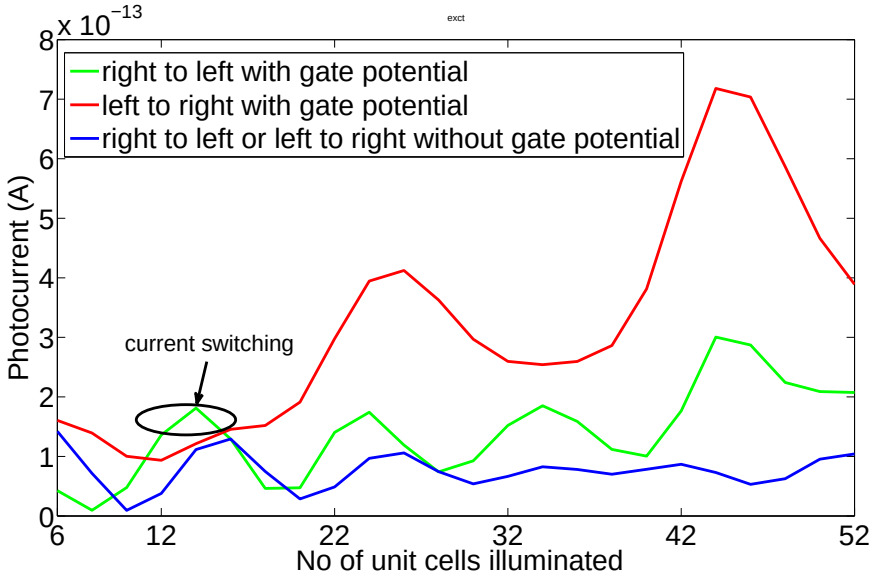

Figure 30. Net photocurrent with left or right insertions vs no of unit cells illuminated. red and green curves are for GP of 0.08 eV and blue curve is without GP.

4.2.5 Illumination of different parts of the device

To understand clearly CDS phenomenon, we have illuminated different parts of the device and looked at the result. We find that when only the left part of the device is illuminated, the QE vs. photon energy curve is like a conventional PD. If we illuminate the quantum well part only then there is no photocurrent, as the structure becomes symmetric from the point of view of photon illumination. But if we illuminate both the parts together, we get the CDS effect. One of the advantages of this computational method is that we can find the photocurrent contributions that are coming from different VB electron energies. Obviously, to get the total photocurrent we have to integrate the electron energy specific photocurrent over electron energies. The QE vs. photon energy and energy resolved photocurrent for different parts illuminated are shown in different parts of Figure 31.

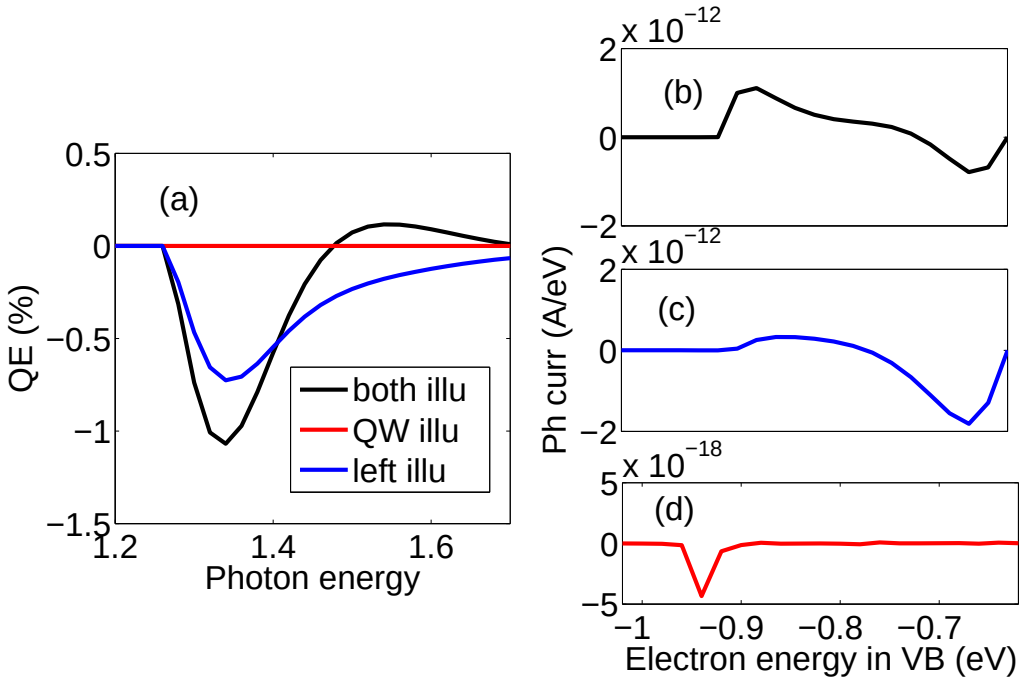

Figure 31. (a) QE vs. photon energy for different parts illuminated. (b)Energy resolved photocurrent vs. VB electron energy for both parts illuminated (c)Energy resolved photocurrent vs. VB electron energy for left part illuminated. (d)Energy resolved photocurrent vs. VB electron energy for right part (QW) illuminated.

4.2.6 Decohered electrons

To understand, whether the effect is coming from the coherence of electrons, we used decohered electrons for photocurrent calculations. The result is shown in Figure 32. We simulated decohered electrons by making the off-diagonal elements of the electron and hole density matrices zero. This means position specific phase information of the electron has been lost and electrons can no longer produce interference phenomena. If we look at the energy resolved photocurrent, we will find that it has both negative part and positive part. After integrating over available electron energies, if the total photocurrent is negative, we get conventional PD results. But after integration, if total photocurrent is positive we get current direction switching. For decohered electrons the total photocurrent is negative and we do not have current direction switching.

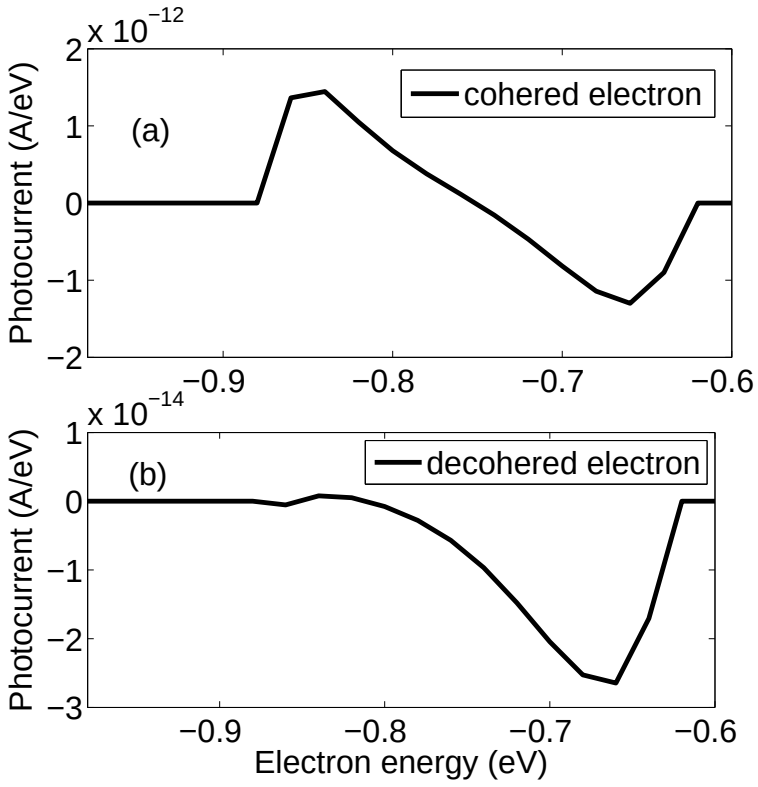

Figure 32. Energy resolved photocurrent for 7-AGNR for photon energy of 1.5 eV for (a) cohered electron (b) decohered electron

4.2.7 Severed paths in VB and CB for electrons

The current direction switching result comes from quantum interference of electron with itself in the left part and the QW part. We can verify this hypothesis by severing the connection between left part and QW part. This is not possible under experimental case but certainly possible in our simulation. The severing is done by making the transfer integral, t between the desired adjoining atoms as 0 (zero). First, we severed the connection between the left part and QW part in the ground state and the CDS effect was gone (shown in Figure 33 (b), (e)). Then we did the severing for excited energy and the CDS effect was gone (shown in Figure 33 (c), (f)). The CDS result is present if there is no severing (shown in Figure 33 (a), (d)). This points to the fact that the result is coming from multipath electron interference.

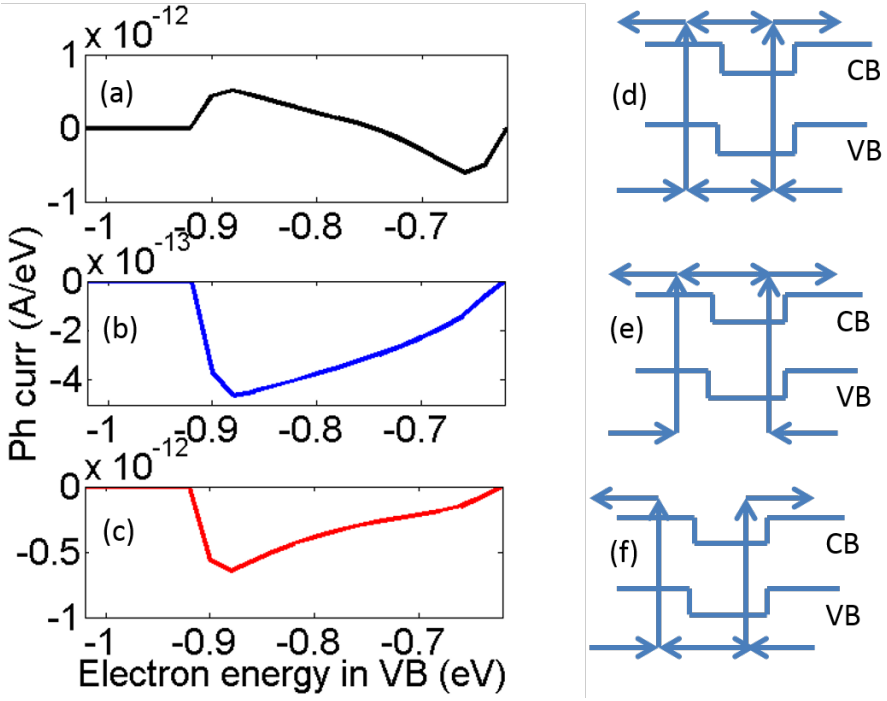

Figure 33. Energy resolved photocurrent vs. electron energy with (a)the connections between left and right parts are present in both ground and excited states. (b)the connection between left and right parts is severed in ground state (c)the connection between left and right parts is severed in excited state. Schematic current paths in VB and CB with (d)the connections between left and right parts are present in both ground and excited states. (e)the connection between left and right parts is severed in ground state (f)the connection between left and right parts is severed in excited state.

4.2.8 3-AGNR and 9-AGNR

In the previous sections, we have shown the results for 7-AGNR. The current direction switching effect is not limited to a particular width of the nanoribbon. This effect shows up for any width of semiconducting AGNR. In this section, the results for two other widths of nanoribbon, namely, 3-AGNR and 9-AGNR are shown in Figures 34 and 35 respectively. A gate potential of 0.08 eV has been used in both the cases. Like the results of the 7-AGNR, for a particular GP, as the illumination length is increased more than a particular length, the CDS effect becomes nonexistent. For a particular GP, the illumination length at which the CDS effect goes away can be different for different widths of AGNR because the band-structure for different widths are different and for a particular energy, Bloch wavelength of the electron can be different for different widths of AGNR.

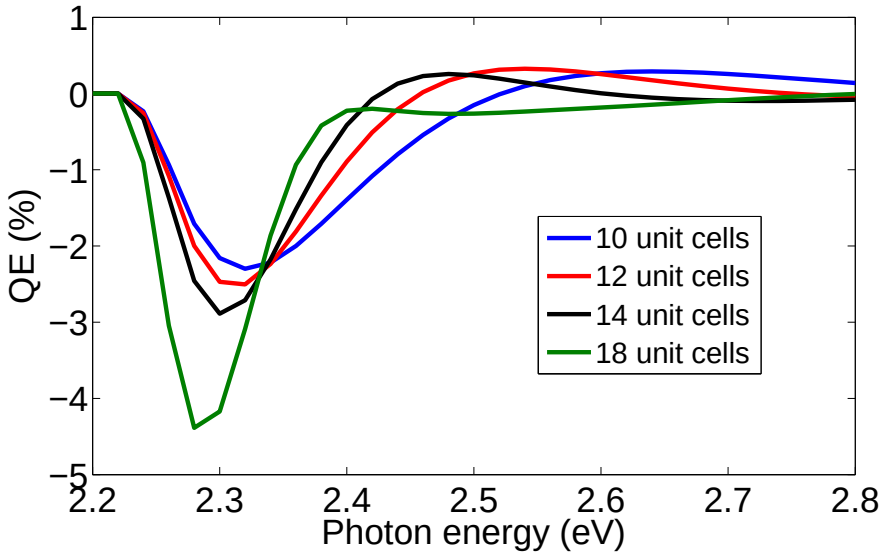

Figure 34. QE vs. photon energy for 3-AGNR for different illumination length

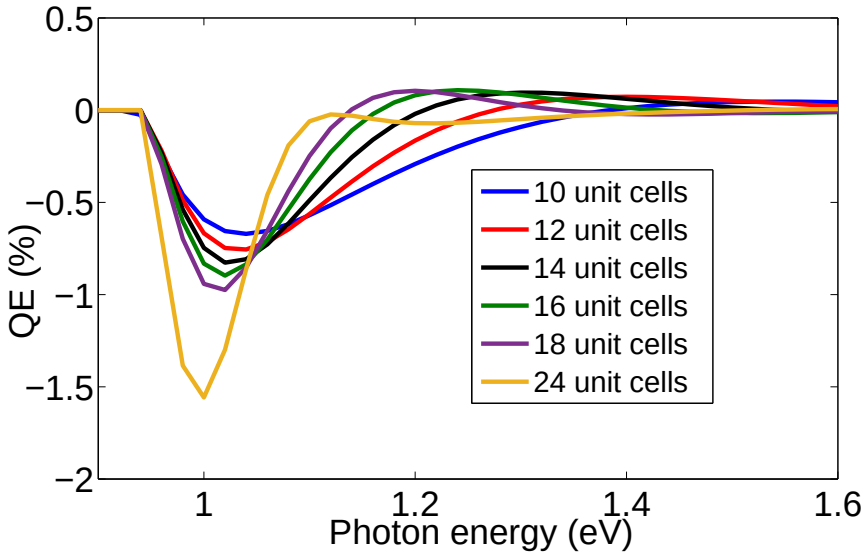

Figure 35. QE vs. photon energy for 9-AGNR for different illumination length

4.2.9 1-D structure

To examine whether the current direction switching result is graphene specific or applicable for any semiconductor material, we performed computations for a hypothetical two-band 1-D structure. This 1-D structure consists of an 1-D chain of atoms with two available energy levels for each atomic position as is shown in Figure 36(a). The hamiltonian is formed with nearest neighbor tight binding model. This structure has a band-gap of 2.0 eV. The band diagram for the structure is shown in Figure 36(b). The

photocurrent vs. photon energy for various length of illumination for an applied gate potential of 0.1 V is shown in Figure 37. In Figure 37, it is seen that for a gate potential of 0.1 V, if the illumination length is up to 12 unit cells, the CDS effect is visible. When the illumination length is increased to 14 unit cells, the CDS effect goes away.

So,we have found that the current direction switching result holds for the 1-D structure also. This points to the fact that this is a much more robust phenomenon and also to the fact that this comes from longitudinal wave pattern of the electron.

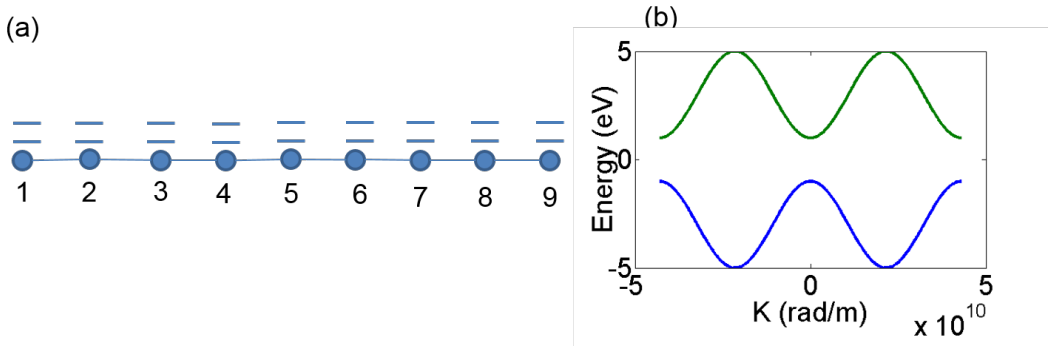

Figure 36. 1-D atomic chain and Band-diagram for 1-D structure

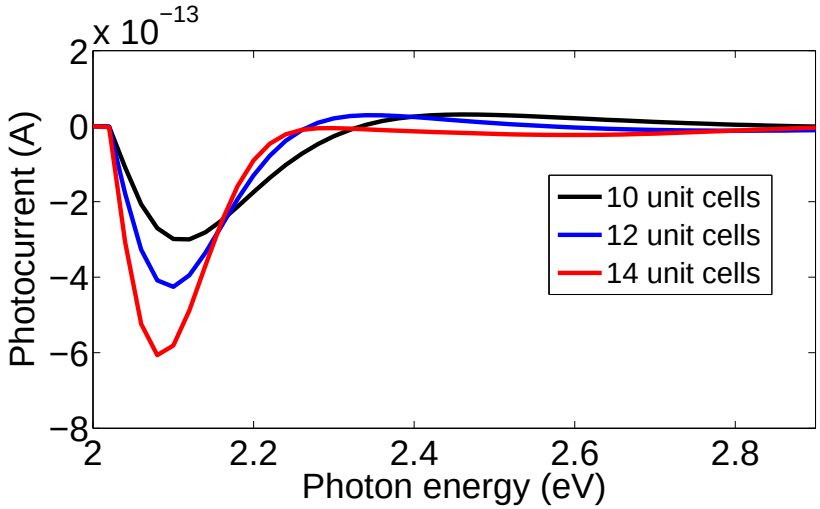

Figure 37. Photocurrent vs. photon energy for 1-D structure for various illumination length for a gate potential of 0.1 eV

4.2.10 Higher bands for 7-AGNR

The current direction switching effect is present not only for transitions from highest lying VB to lowest lying CB but also for higher lying bands. The optical transitions

in AGNR are governed by selection rules. For polarization of light along the length of nanoribbon, the allowed transitions are from highest lying VB to lowest lying CB, from 2nd highest lying VB to 2nd lowest lying CB and so on. The band diagram for 7-AGNR and allowed transitions are shown in Figure 38. The photocurrent vs. photon energy for 7-AGNR for illumination length of 12 unit cells and for a gate potential of 0.08 eV is shown in Figure 39.

Two peaks for photocurrents are observed in Figure 39. One is around 1.27 eV (corresponding to transition are from highest lying VB to lowest lying CB) and the second is around 2.24 eV (corresponding to transition from 2nd highest lying VB to 2nd lowest lying CB). Around both these peaks the current direction switching effects are also observed.

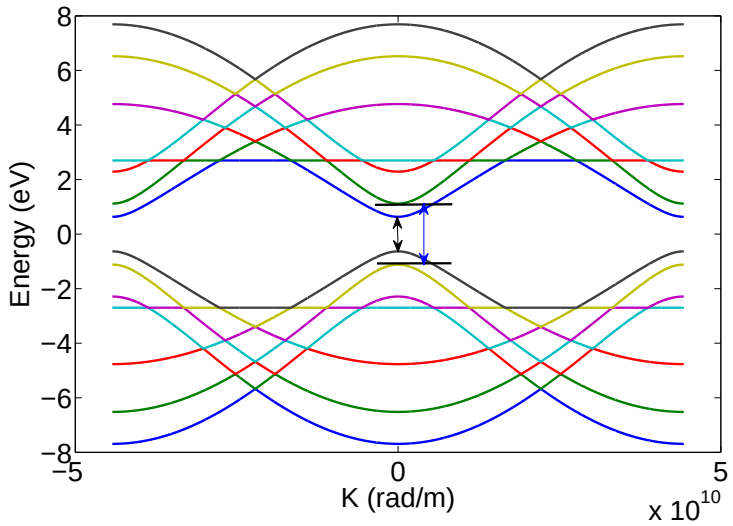

Figure 38. Band-diagram for 7-AGNR

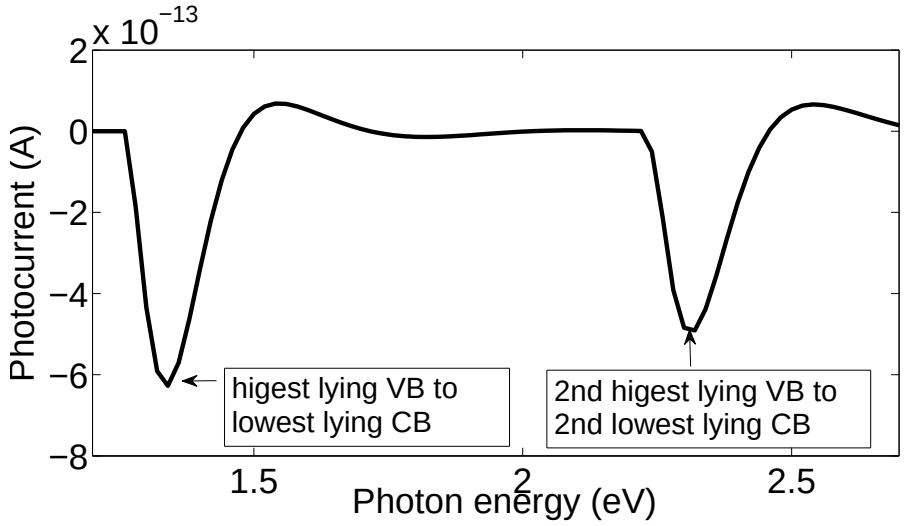

Figure 39. Photocurrent vs. photon energy for 7-AGNR for illumination length of 12 unit cells and for a gate potential of 0.08 eV

4.2.11 Electron can interfere only with itself

When we illuminate the device structure, photoexcited holes are created. These holes can be filled up by electrons which can potentially come from either side of the device. The band-profile in VB and CB can inhibit the injection of electrons at particular energies from left or right side. To understand the origin of CDS effect, within our simulation, we injected electrons in the VB to fill up the photoexcited holes either from left side only or from right side only. The results are shown in Figure 40. This result is for 7-AGNR when 10 unit cells are illuminated with a GP of 0.1 eV. When the electrons in the VB are injected from the left side only, the net electron photocurrent is from left to right (negative photocurrent) and when the electrons in the VB are injected from the right side only, the net electron photocurrent is from right to left (positive photocurrent). If we find out the algebraic sum of photocurrents coming from left injected and right injected electrons, we find that this algebraic sum is equal to the photocurrent when both left and right injections are present at the same time. This result also points to the fact that electron can only interfere with itself and at a particular electron energy left and right going electrons cannot interfere.

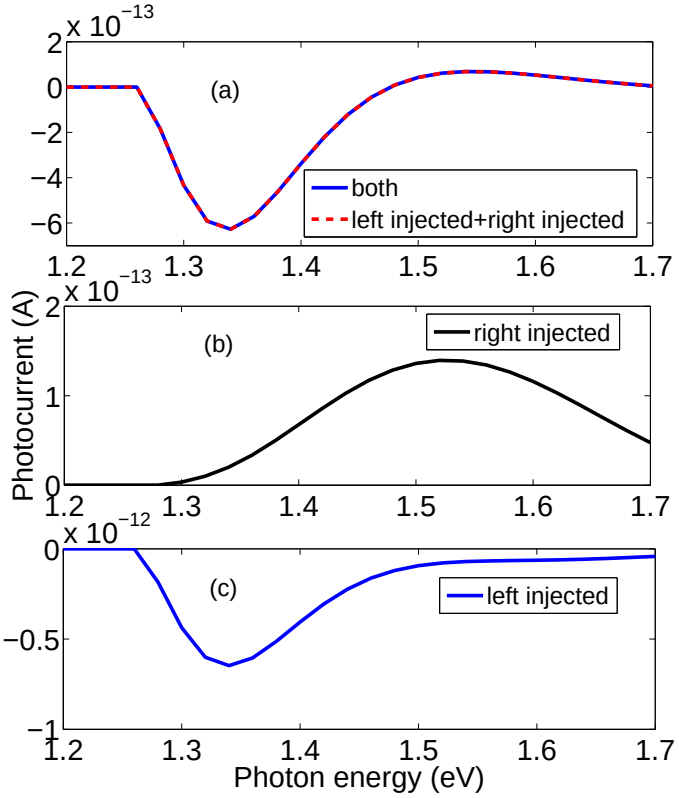

Figure 40. Photocurrent vs. photon energy for (a) electrons injected from both sides and algebraic sum of left and right injected electrons (b) right injected electron(c) left injected electron.

4.2.12 Electron-electron interaction

As described in section 3.5, we account for the electron-electron interaction in the system through Hartree potential or Poisson equation. The effect of gate potential has been taken care of by bending the valence band and conduction band in that part of the device. Since the photoexcited hole and electron density functions are different for each energy level, the total photoexcited electron and hole densities, $n(r)$ and $p(r)$ are found by integrating the electron and hole densities over the energy range. Since electron and hole densities are different, this gives rise to some net charge within the device. So when electrons pass through the device, they will feel some potential. This is the source of Hartee potential. This Hartree potential can be found by solving the Poisson equation as is shown in equation 45 .

$$\nabla^2 U(r) = \frac{e}{\epsilon}(n(r) - p(r)) \tag{45}$$

Here $U(r)$ is the Hartree potential, e is the charge of an electron, ϵ is the permittivity of the material, $n(r)$ is the electron density and $p(r)$ is the hole density.

If there is an excess of negative charges (electrons) in various places within the device, the electrons passing through the device will feel a positive potential (potential barrier) and if there is an excess of positive charges (holes) in various places within the device, the electrons passing will feel a negative potential (potential well). The magnitude of photogenerated electron and hole densities are small and their magnitudes are almost same. So net charge density is very small and potential arising from this charge density is also very small (in the range of 10^{-17} to 10^{-15}) and has negligible effect on electrons passing through the device. In Figure 41 , we show the result without considering the electron-electron interaction and with considering the electron-electron interaction. This result is for 7-AGNR, a GP of 0.1 eV and 12 unit cells illuminated. The results are identical for all practical purposes.

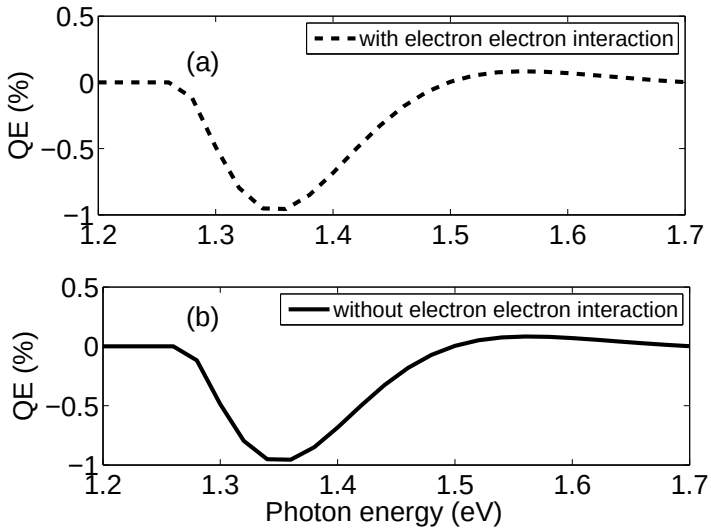

Figure 41. QE vs. photon energy for CDS device (a) with electron electron interaction (b) without electron electron interaction.

4.2.13 Phonon dephasing

We have included the effect of elastic dephasing due to phonon. The motivation is to see how the coherence of electron is lost with phonon dephasing. Elastic phonon dephasing

introduces a scalar potential in the Schrodinger equation (NEGF formalism) and introduces an image of the electron and hole density functions in the same energy level[11]. A detailed description of the mathematical formulation for the elastic phonon dephasing and also a flowchart for the self-consistency loops has been provided in section 3.4.

The results with phonon dephasing for the CDS device are shown in Figures 42 and 43. In Figures 42(a) and 43 (a), we can see that as the strength of dephasing parameter, D is increased CDS effect gradually vanishes. For Figure 42(a), we have used 7-AGNR with a GP of 0.1 eV and with 10 unit cells (4.26 nm) illuminated and for Figure 43(a), we have used 7-AGNR with a GP of 0.03 eV and with 24 unit cells (10.224 nm) illuminated

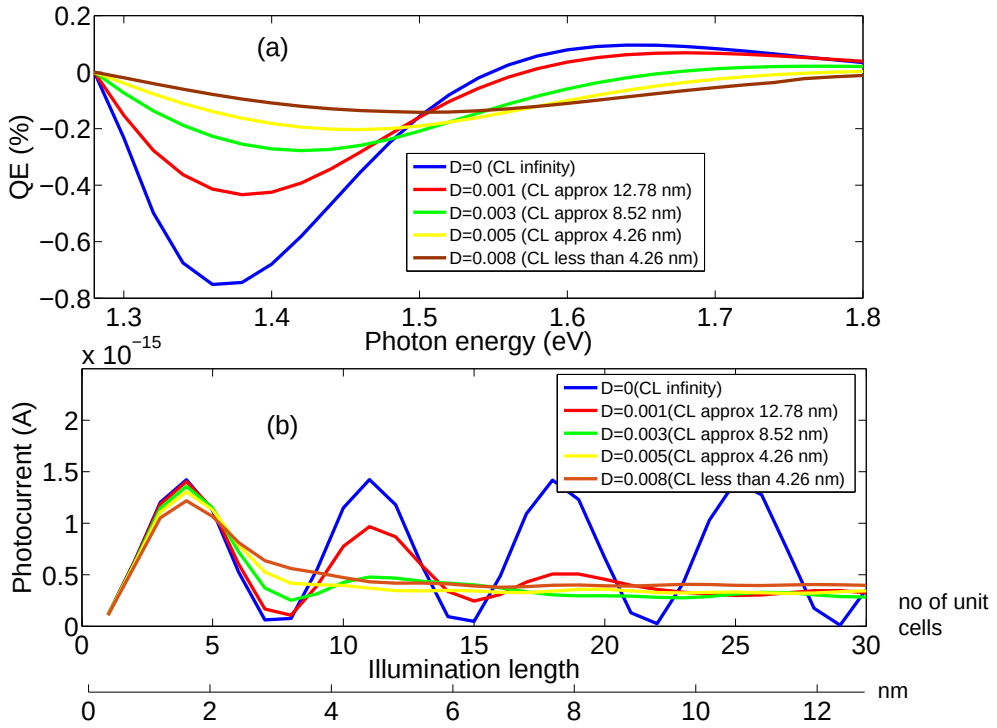

Figure 42. (a) QE vs. photon energy with phonon dephasing for different phonon dephasing parameter (Device length 10 unit cells (4.26 nm) and GP is 0.1 eV). (b) Net photocurrent vs. illumination length for 7-AGNR for different phonon dephasing parameter (momentum conserved electron only for photon energy of 1.6 eV)

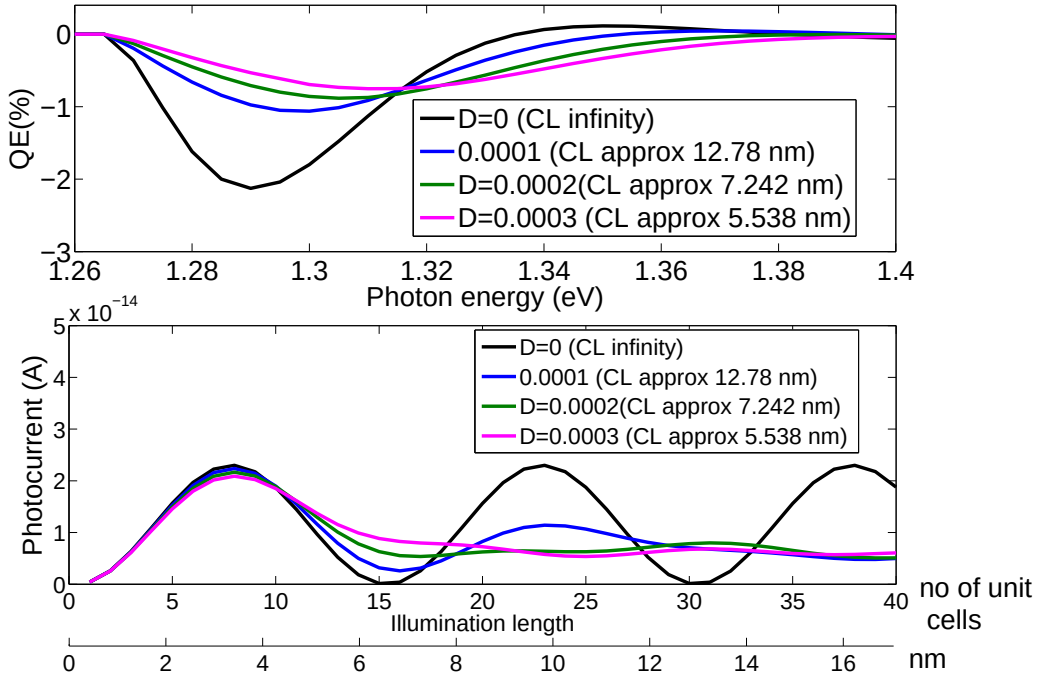

Figure 43. (a) QE vs. photon energy with phonon dephasing for different phonon dephasing parameter (Device length 24 unit cells (10.224 nm) and GP is 0.03 eV). (b) Net photocurrent vs. illumination length for 7-AGNR for different phonon dephasing parameter(momentum conserved electron only for photon energy of 1.36 eV)

Now in order to find the relationship between the phonon dephasing parameter, D and coherent length, we have done simulation for 7-AGNR with one sided insertion of electrons in VB with phonon dephasing. We have explained before that for one sided insertion of electrons in VB, the net photocurrent has periodic oscillation. The results are shown in Figures 42(b) and 43(b) . In Figures 42 (a) and 43 (a), the results are for 7-AGNR CDS device while in Figures 42 (b) and 43 (b), the results are for 7-AGNR (not CDS device but nanoribbon only). In Figure 42 (b), we see that as the parameter D is 0, the coherent length is infinity (wavy pattern remains for infinite length), if D is 0.001, coherent length is around 30 unit cells (12.78 nm), if D is 0.003, coherent length is around 20 unit cells (8.52 nm) and if D is 0.005 coherent length is less than 10 unit cells (4.26 nm). The results shown in 42 (a) are for CDS device with length of 10 unit cells. In 42 (a), we see that as D becomes 0.005, the CDS result also starts to go away because now the coherent length is less than the device length. For the results shown in Figure 43, the same thing happens.

4.2.14 Discussion on bound state within the quantum well

For our current direction switching device, we have a potential well (quantum well) in one side of the device to create asymmetry in the device. We know that there is always at least one bound state within the finite potential well [63]. Electrons can be excited from valence band to this bound state in the conduction band. Once the electrons are in quantum well (QW) of the CB, there is no other mechanism in our simulation now for these electrons to get out, because we do not have inelastic phonon excitation in our simulation and also the nanoribbon is infinitely long in both directions. Since this electron is stuck in the QW and there is no corresponding accumulation of holes in the the VB, there is net negative charge in the QW region of the device. We have performed simulation to check whether this bound state within the QW affect the results negatively. We have simulated the effect of bound electrons through Poisson equation and Hartree potential as described in section 3.5.

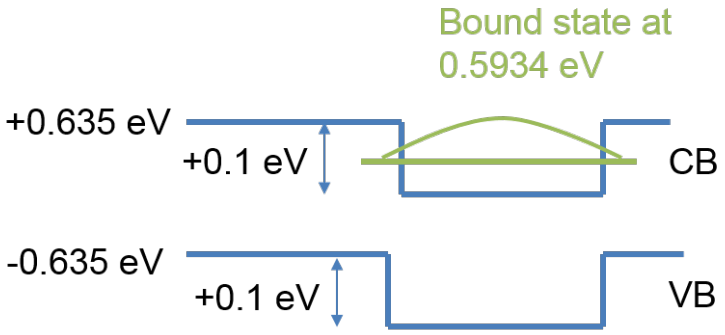

Figure 44. Bound state in QW in CB for 7-AGNR CDS device

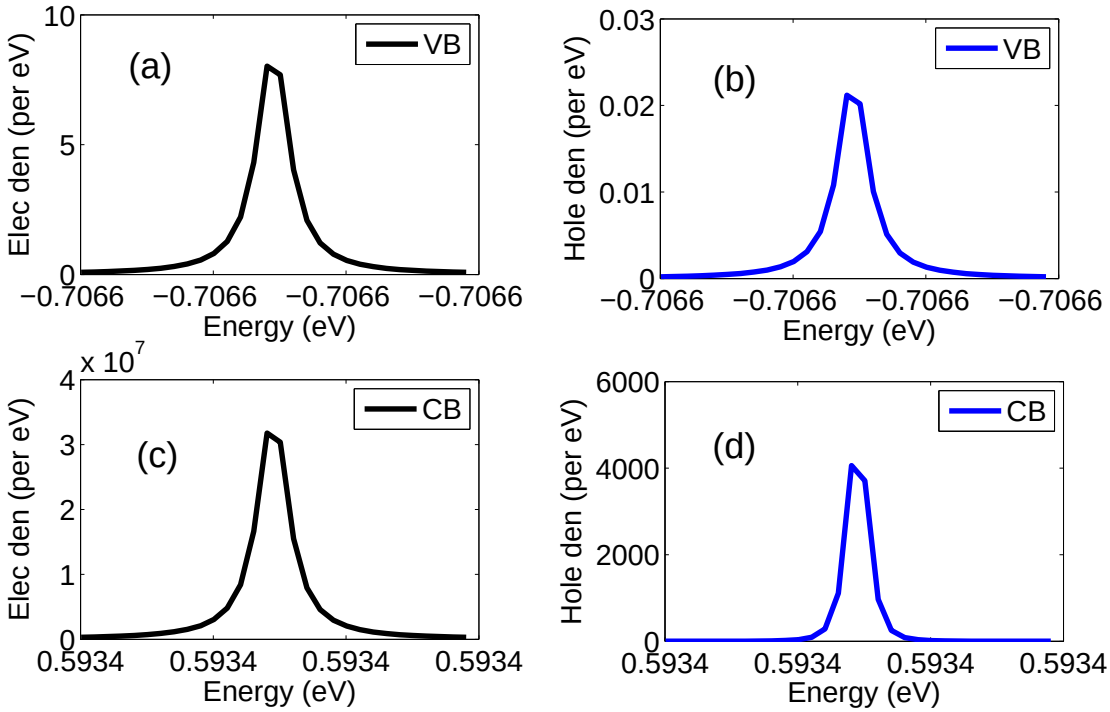

Figure 45. Electron and hole densities in CB for bound state in QW in CB and corresponding electron and hole densities in VB for for 7-AGNR CDS device for 1.3 eV photon excitation.

For the results shown in this section, 7-AGNR with 12 unit cells illuminated has been used. A GP of 0.1 eV has been applied in 6 unit cells. For this particular QW, the bound state is at 0.5934 eV as shown in Figure 44. For our simulation the leads are also made of infinite graphene nanoribbons. For this simulation we have used 41 unit cells. 14 unit cells are left of illuminated region and 15 unit cells are right of illuminated region. For finding this charge density and potential we have considered 30 energy buckets around the bound state with an interval of 10^{-8} eV. The energy resolution has been increased up to the energy when the total number of states around the bound energy come to a stable value with the increase of energy resolution. In Figure 45, we show the electron and hole densities in the bound state in CB and corresponding electron and hole densities in VB for 1.3 eV photon excitation. In Figure 45(c), we see that there is a large concentration of electrons in the bound state in CB, since electrons do not have any mechanism to come out of the bound state.

In each of Figure 46 and 47, we show the net charge density within the device and potential arising from this charge density. For Figure 46 the photon energy used is 1.3 eV and for Figure 47, the photon energy used is 1.5 eV. The charge densities for other energies except the bound state energy are negligible compared to charge density in the bound state. The charge density in the bound state is in the range of 10^{-3} per atomic position and the charge densities in other energies are in the range of 10^{-10} per atomic position. It can be mentioned here that though the electron density in the bound state is in the range of 10^{7} as shown in Figure 45(c), this result is per eV. So when integrated over the available energy range, the position resolved electron density becomes in the range of 10^{-3} as shown in Figures 46(b) and 47(b).

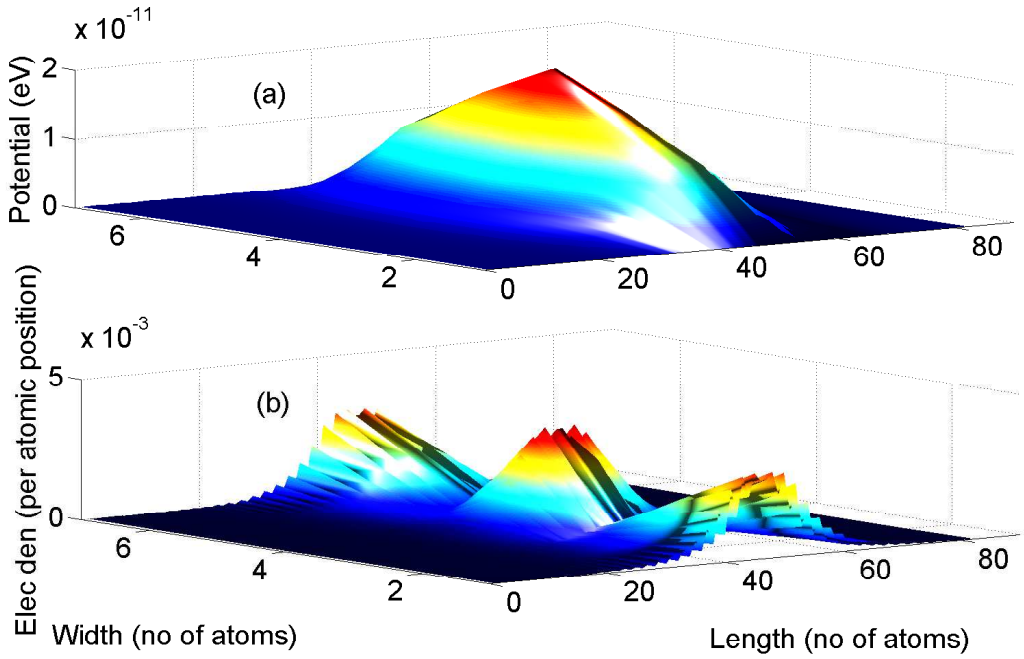

Figure 46. (a) Hartee potential (b) Electron density within the CDS device considering the bound state in QW in CB for photon energy of 1.3 eV

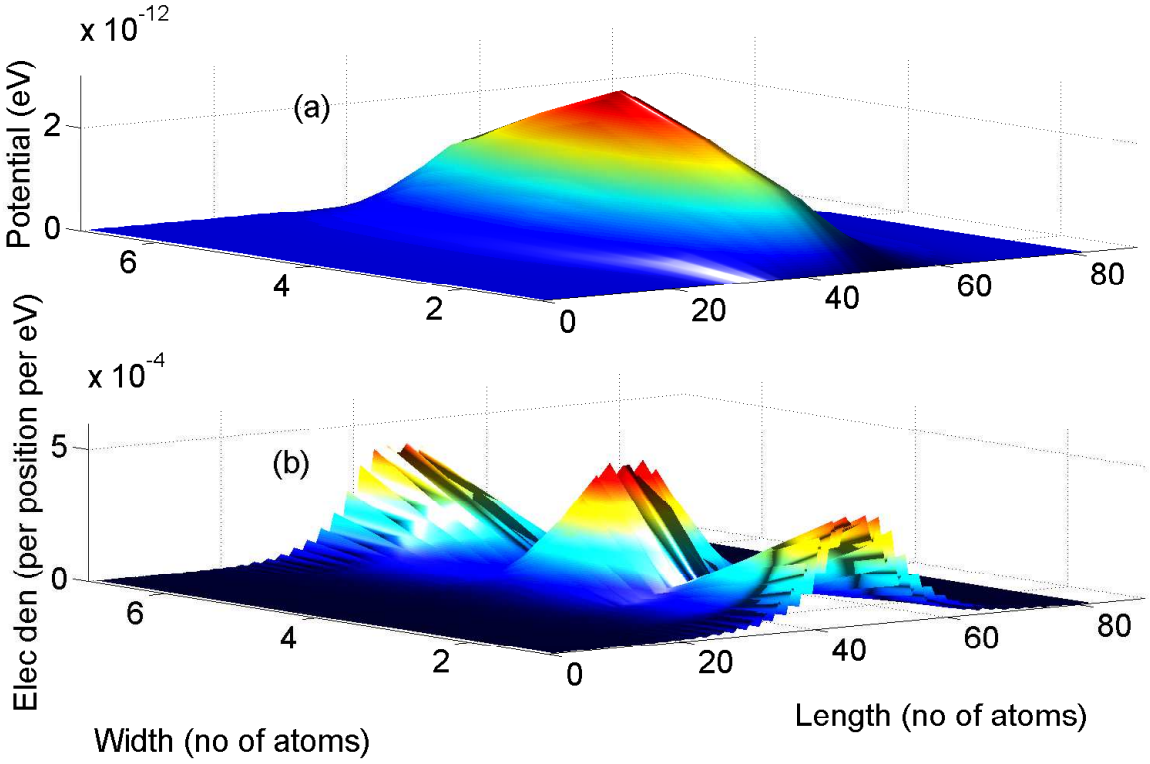

Figure 47. (a) Hartee potential (b) Electron density within the CDS device considering the bound state in QW in CB for photon energy of 1.5 eV

This potential arising from charge in the bound state in the QW is very small and as a result has negligible effect on photocurrent passing through the device at various photon energies. So the bound state has negligible effect on the CDS-PD results. It should be mentioned here that since graphene is a 2-D material, the charge density per unit volume is small and as a result the resultant potential is also small.

4.2.15 Phonon bath in the leads

The results coming from elastic phonon dephasing in the leads have been incorporated in this section. Here the device is made of 3-AGNR and 8.52 nm long. The coherence length of electron has been adjusted to be 8.52 nm also for the momentum conserved electron by adjusting the phonon dephasing strength. The illumination length is equal to device length.

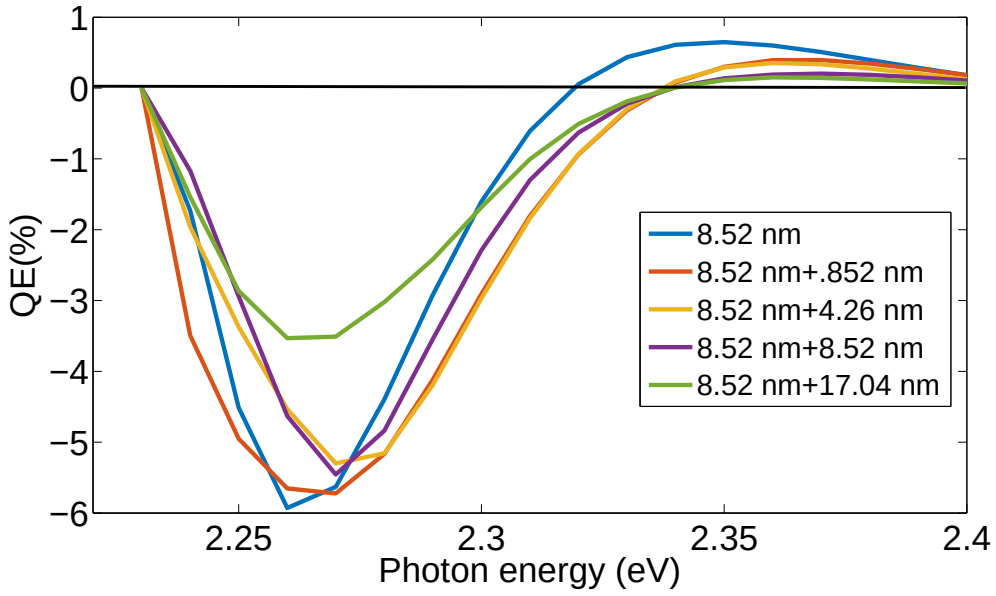

Figure 48. QE vs. photon energy for different length of leads. The sizes of the device and leads are shown before and after the '+' sign

For the particular simulation as is shown in Figure 48, keeping the device length fixed, the lead length has been increased and electrons are collected at the end of the lead. The sizes of the device and leads are shown before and after the '+' sign in the legend of Figure 48. As is shown in the Figure 48, though the length of leads is increased, the CDS behavior is still persistent. Electron interference effect happens in the device and illumination area. In the leads electrons travel as particles because coherence length is equal to device length. Once some electron density has been created in the end of the device due to light interaction, electrons then travel in the leads as particles.

More study is needed in this topic.

4.2.16 Experimental nanoplasmonic field

From the computations and simulations performed in this thesis, it has been found that light needs to be confined in an area less than the Bloch wavelength of participating electrons to observe the current direction switching (CDS) result. For the phase coherence length experimentally achievable and device sizes envisioned in this thesis, this is

in the range of 10-30 nm.

Researchers have demonstrated three-dimensional plasmonic nanofocusing of light (710 nm) that converge at a ~10 nm apex in a 36 nm X 36 nm X 14 nm volume[3]. 550 nm (2.24 eV) light can be focused in 27.5 nm (around 1/20 th of the wavelength) length.

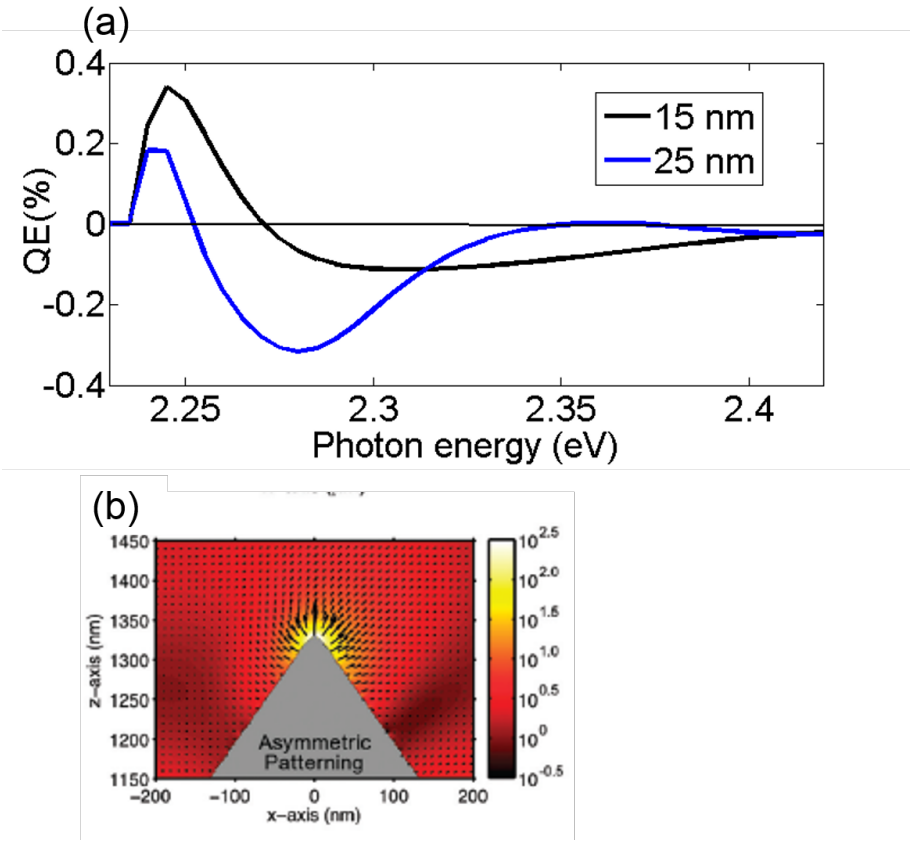

Figure 49. (a) QE vs. photon energy with experimental nanoplasmomic electric field profile (b) experimental nanoplasmomic electric field profile (collected from [3])

In Figure 49(a), the simulation results for the nanoplasmonic experimental field as is shown Figure 49(b) is shown. The CDS result is still there for 25 nm device but now the CDS result has shifted to the low photon energy. It should be mentioned here that, for all the results shown in this thesis except for the results shown in this section, the incident electromagnetic field has been assumed to have a plane wavefront. For the results shown in Figure 49(a), the electric field profile is as shown in Figure 49(b) and this is completely different from plane wave. There is a 180° phase shift in the longitudinal component of the electric field between the two parts of the device.

Much more study is needed in this topic.

4.3 GNR Mach-Zehnder interferometer (MZI) photodetector

In this section, we analyze the efficiency of coupling of light between two longitudinal resonant modes of the MZI structure in GNR and how this structure can act as a PD.

One device structure whose operation is based on quantum interference and has attracted attention is the resonant tunneling diode. In graphene nanoribbons, a Mach-Zehnder interferometer structure gives the same transmittance pattern as that of a resonant tunneling diode for incoming electrons. In this section, we investigate the optoelectronic properties of this MZI structure formed by graphene nanoribbons and a possible application of this structure as photodetector. In a MZI structure, an electron in ground transverse mode goes through the device with transmittance one (1) due to constructive interference at energies corresponding to longitudinal resonant modes. At these resonant energies, electrons have high density of states. In this section, we investigate for the first time the interaction of light in graphene nanoribbon MZI structure and specifically we look at the coupling of light between longitudinal resonant modes for both zig-zag and armchair structures.

This structure has the advantages that it does not require any p-n junction, that it is very small and that the PD has high internal quantum efficiency of 50% and external quantum efficiency of up to 5.2%. By changing device dimensions or using different resonant peaks, this structure can be used to detect light of different photon energies.

4.3.1 Device geometry

The device has a symmetric Mach-Zehnder type interferometer structure. The device geometries for zig-zag type nanoribbon and arm-chair type nanoribbon are shown in Figure 50 and Figure 51 respectively.

In this section, we have shown simulation results for both zig-zag type and armchair type nanoribbon structures. For the simulation, for zigzag type we have used N_a=1.136 nm (12 atoms), N_b=5.396 nm (52 atoms), N_c=0.986 nm (10 atoms), N_d=1.968 nm (18 atoms) and N_e= 1.136 nm (12 atoms). For armchair type we have used N_a=0.738 nm (7 atoms), N_b=2.214 nm (19 atoms), N_c=0.71 nm (8 atoms), N_d=4.97 nm (48 atoms) and N_e= 0.738 nm (7 atoms). The lattice constant is 0.142 nm.

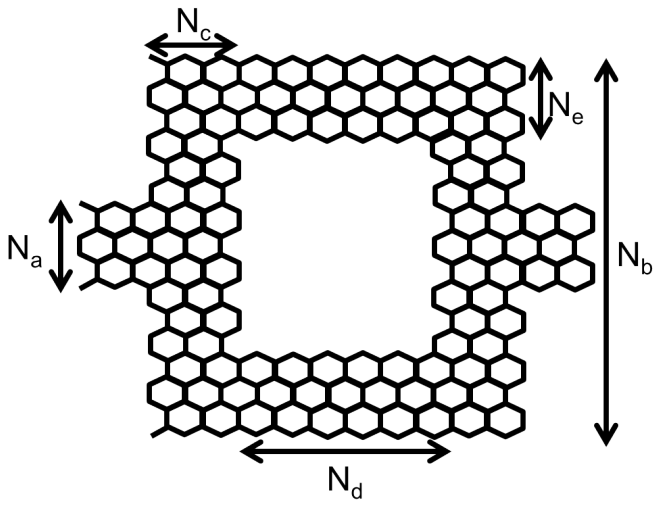

Figure 50. Graphene nanoribbon MZI structure (zig-zig type).

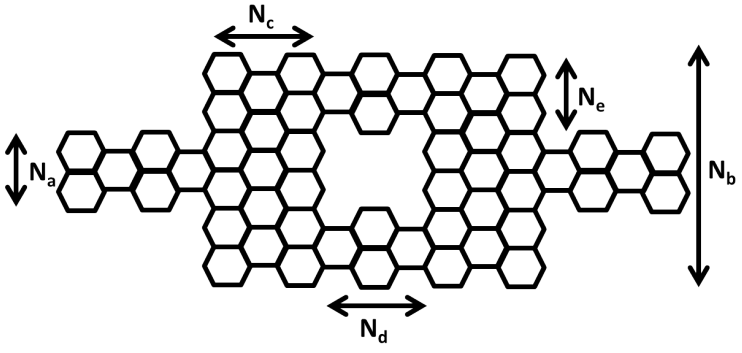

Figure 51. Graphene nanoribbon MZI structure (armchair type).

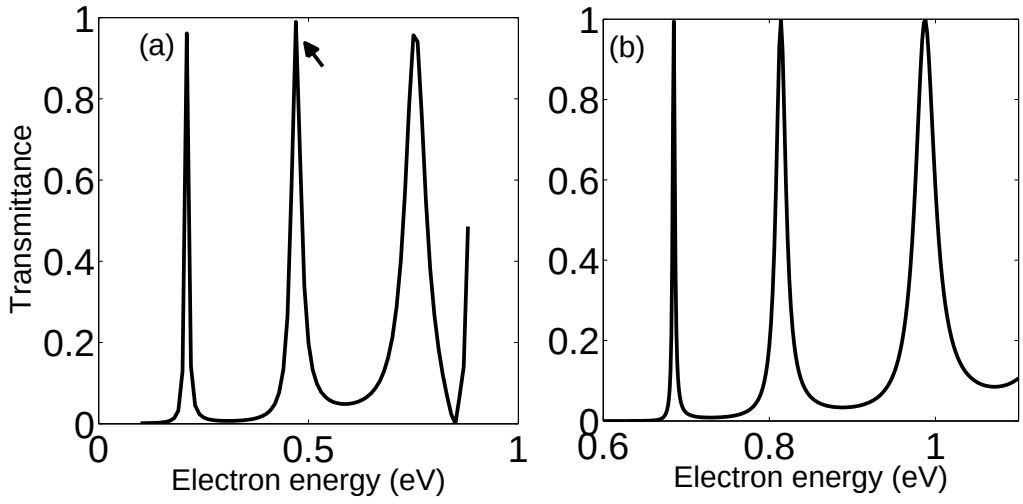

Figure 52. Transmittance vs. electron energy variation for graphene nanoribbon MZI structure (a)zig-zag type (b)armchair type

4.3.2 Results and discussion

The MZI structure in graphene nanoribbon works like a resonant tunneling structure, meaning that at some energies electrons go through the structure as if there were no barriers. At these energies the transmittance is one (1) and constructive interference occurs. These energies are called the resonant energy levels. There can be a 1st resonant level, a 2nd resonant level and so on. And at some other energies, electrons cannot go through the device at all. At these energies the transmittance is zero (0) and destructive interference happens. These regions are called the valley regions. The modes described so far are the longitudinal resonant modes for first transverse mode. At higher energy at higher transverse modes, longitudinal resonant modes can also occur. The transmittance pattern for the zig-zag structure is shown in Figure 52(a) and the transmittance pattern for armchair structure is shown in Figure 52(b).

As the length of the middle arm, N_d increases, the longitudinal resonant peaks become sharper and peaks become closer in energy. As the width of the nanoribbon, N_a increases, the higher transverse modes become closer in energy and the energy space available for longitudinal resonant modes to occur within a transverse mode decreases. Also as the width N_a increases, the longitudinal resonant peaks become sharper in energy. From our simulation results we see that by changing the device dimensions, we

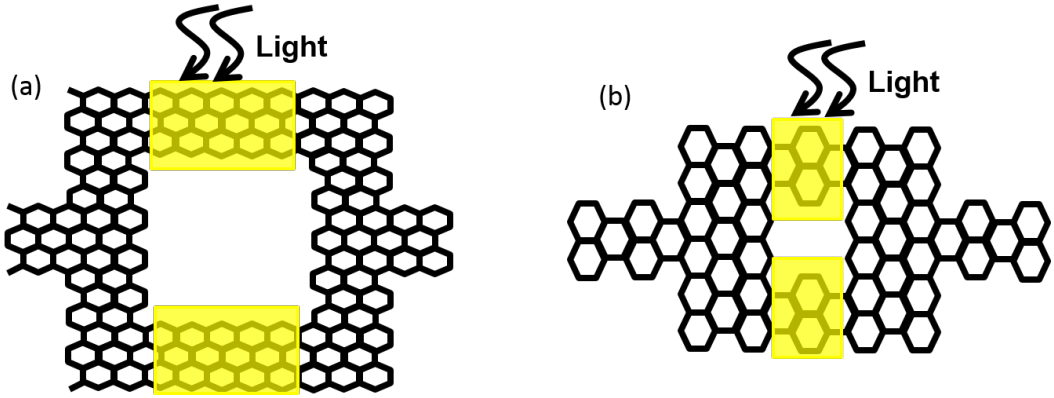

Figure 53. Device structure for light detection by coupling light between two resonant peaks (a) zig-zag structure (b) armchair structure.

can detect photons of energy of 0.1 eV to 1 eV.

Now we look at the response of the structure after light illumination.

4.3.3 Coupling light between resonant peaks

By shining light on both the interferometer arms as is shown in Figure 53, this structure can be made to work like a photodetector. As we shine light, electrons in the low energy level (1st resonant level) absorb the light and get transferred to the high energy level (2nd resonant level) and then they leave the device without any other kind of interaction. The calculated lifetime of the electron from photoexcitation is greater than the calculated transit time of the electron through the device. Since we are assuming that the device length is less than the mean free path of the electron, we are neglecting all phonon interactions here. The photocurrent flows in the leads due to the fact that one of the leads (drain) cannot supply the electrons to fill up the holes in the device because the Fermi level in the drain is lower than the Fermi level in the source due to applied bias. All the photogenerated electrons are collected in the leads. Half of these electrons participate in net photocurrent. So this device has an internal quantum efficiency of 50%.

The results of interaction with light for zig-zag and armchair structures are shown in Figure 54 and 55 respectively. For this simulation, the parameters used for zig-zag

structure are the applied voltage is 0.1 eV, photon energy is 0.26 eV and strength of photon flux is 10^{25} photon/m^2/sec ($4.16x10^6$ watt/m^2) and the parameters used for armchair structure are the applied voltage is 0.1 eV, photon energy is 0.13 eV and strength of photon flux is 10^{25} photon/m^2/sec ($2.08X10^6$ watt/m^2). For both the zig-zag and armchair structures, the polarization of applied electromagnetic field is along the length of the device. The full length of middle horizontal arms (216 (12X9X2) atoms for zig-zag structure and 336 (14X12X2) atoms for armchair structure) has been illuminated for this result. In the vertical arms the absorption is two orders of magnitude less than the horizontal arms, so this result is equivalent to illuminating the whole structure. The voltage is applied in such a way that the first resonant level is within the applied voltage range.

In top parts in Figures 54 and 55, we see that when there is no light, currents are flowing in the low energy (1st resonant) levels but there are no currents in the high energy (2nd resonant) levels. As we shine light, currents start to flow in the high energy(2nd resonant) level as are shown in bottom parts of Figures 54 and 55. The currents shown in Figures 54 and 55 are energy resolved current, i.e., current per unit energy. Negative current means electrons are entering the device.

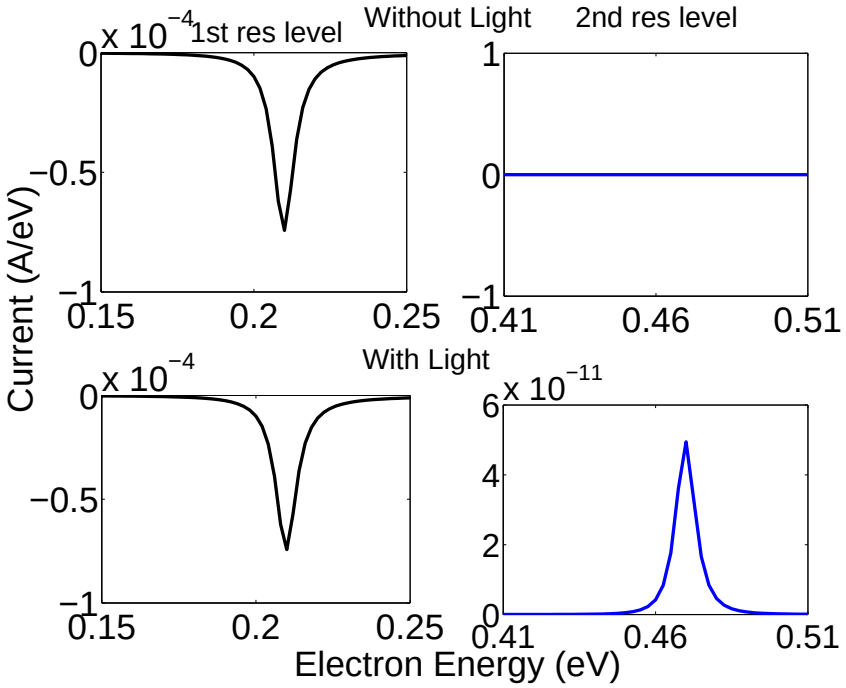

Figure 54. (zig-zag structure) Current density vs. electron energy for light detection by coupling light between two resonant peaks.(top) without light (bottom) with light.

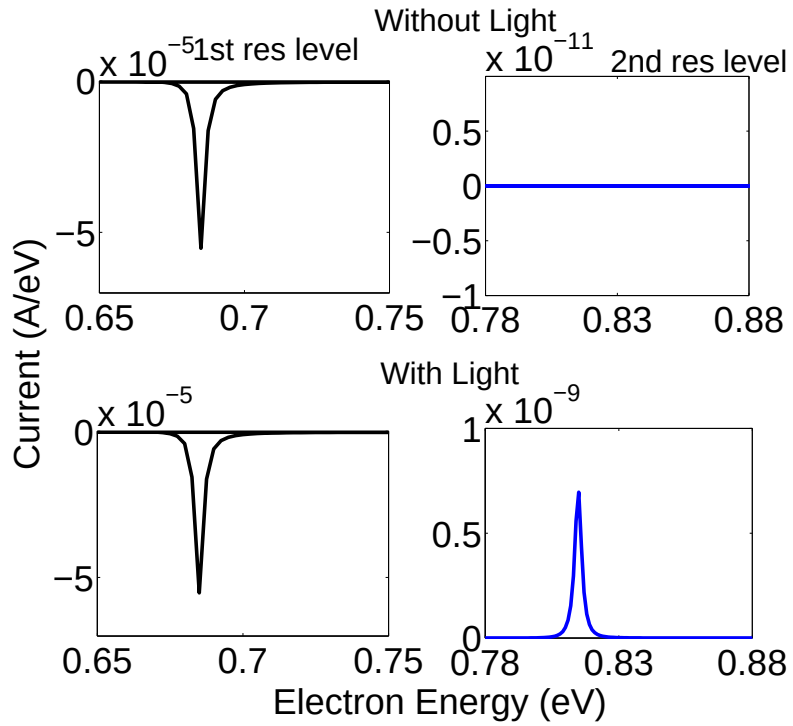

Figure 55. (armchair structure) Current density vs. electron energy for light detection by coupling light between two resonant peaks.(top) without light (bottom) with light.

The photocurrent does not increase linearly with the number of atoms illuminated in the middle arm. The variation of peak photocurrent with number of blocks illuminated is shown in Figure 56. Each block contains 12 atoms in zig-zag structure and 14 atoms in armchair structure. Initially the peak photocurrent increases quadratically with number of blocks illuminated and then the current starts to saturate. This particular variation of current comes from particular waveshape of electron in position basis on ground and excited states and Fermi golden rule which is being taken care of internally in NEGF formalism. The photocurrent is more in armchair structure than in zig-zag structure. This is because in zig-zag structure some neighboring atoms lie in vertical orientation which feels zero electric field because the polarization is in horizontal direction. Also the number of illuminated atoms (316) is more in armchair structure than the number of illuminated atoms (216) in zig-zag structure.

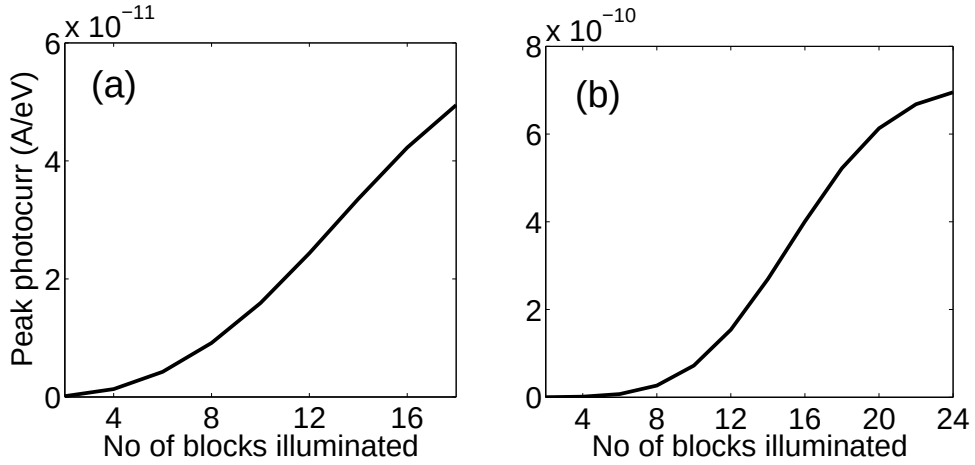

Figure 56. Variation of peak photocurrent with number of blocks illuminated.(a) zig-zag structure (b) armchair structure

It should be mentioned here that, without light the bias current through the device is in the range of $10^{-5}A/eV$ and with light the photocurrent is in the range of $10^{-11}A/eV$. So we need some kind of differential measurement to detect the current in the leads. Alternatively a high frequency pass filter can be used in the output of the device and the device can detect the variation of light.

With the appropriate bias, the device can also be used to detect photon energy corresponding to energy difference of any two resonant levels. The peak photocurrent variations with different photon energy are shown in Figures 57(a) and 57(b) corresponding to zig-zag and armchair structures respectively. 144 (12X6X2) atoms and 140 (14X5X2) atoms in the middle arm have been illuminated for zig-zag and armchair structures respectively for this result. 0.26 eV and 0.55 eV are the energy differences of 1st and 2nd resonant levels and 1st and 3rd resonant levels in zig-zag structure. 0.13 eV and 0.3 eV are the energy differences of 1st and 2nd resonant levels and 1st and 3rd resonant levels in armchair structure.

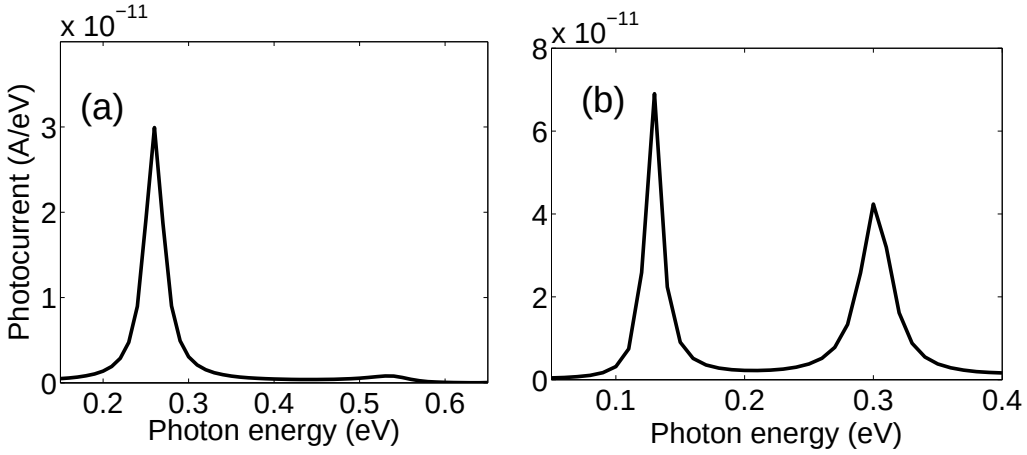

Figure 57. Variation of peak photocurrent with photon energy.(a)zig-zag structure(b) armchair structure

If we integrate the energy resolved photocurrent, we can calculate the total photocurrent through the device. For integration, we have used Fermi-Dirac statistics at 300^0 K in the leads. Knowing the photocurrent, the external quantum efficiency of the device can be calculated as

$$\text{Quantum efficiency (QE)} = \frac{\text{net photocurrent in either lead/q}}{\text{no of photons in the illuminated area per second}} \quad (46)$$

For zig-zag structure, external quantum efficiency shows a peak of 1.6% at photon energy of 0.26 eV and for armchair structure, external quantum efficiency shows a peak of 5.2% at photon energy of 0.13 eV as are shown in Figures 58(a) and 59(a). Photon energies 0.26 eV and 0.13 eV are the energy differences between the first two resonant

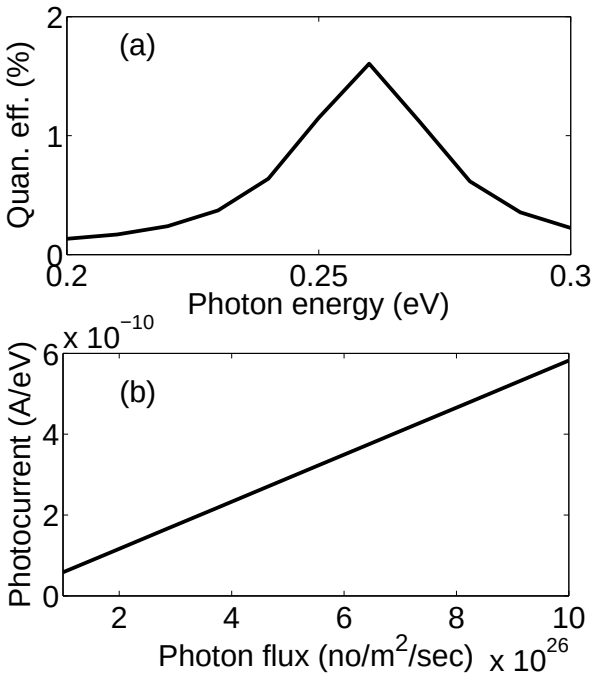

Figure 58. (a)Variation of external quantum efficiency with photon energy.(b) Linear trend of peak photocurrent with photon flux. (zig-zag device)

levels in zig-zag and armchair structures respectively. Quantum efficiencies are highest at 0.26 eV and 0.13 eV because the density of states is higher around resonant energy levels. External quantum efficiency remains constant with strength of photon flux for up to approximately 10^{31} photon/m^2/sec. The variation of peak photocurrent with photon flux is shown in 58(b) and 59(b).

We should mention here that internal quantum efficiency for our device is 50%. In the literature, the reported value of experimentally determined internal quantum efficiency is 15-30%[36]. In the experimental result, the electron hole pairs are separated by the built-in potential of metal-semiconductor junction. The experimental internal quantum efficiency is lower because they have electron hole recombination coming from phonon scattering and scattering in metal-semiconductor interface. We do not allow any electron hole recombination in our device. Our external quantum efficiency is 5.2% for armchair structure and 1.6% for zig-zag structure. Our photon absorption rate is 10.4% for armchair structure and 3.2% for zig-zag structure. This is higher than the 2.3% absorption rate of bulk graphene because of two reasons. First, we have high density of states at energies corresponding to longitudinal resonant modes and second,

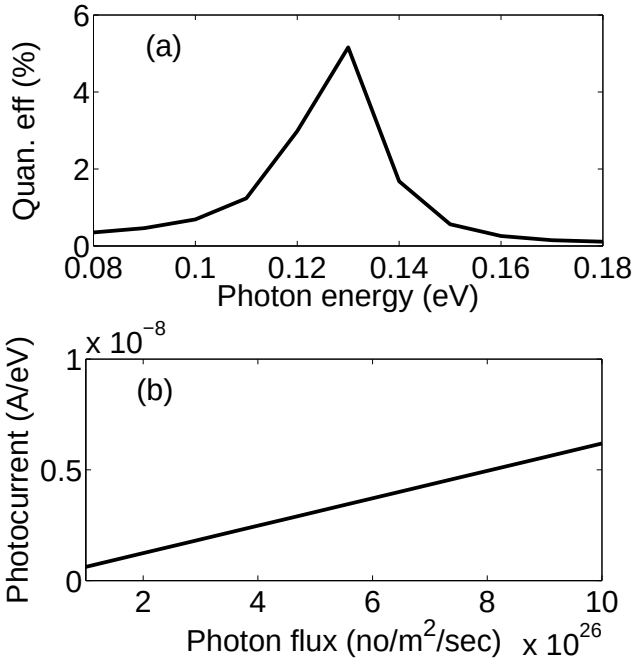

Figure 59. (a)Variation of external quantum efficiency with photon energy.(b) Linear trend of peak photocurrent with photon flux. (armchair device)

the high absorption rate is also coming from particular waveshapes of electron in 1st longitudinal resonant state and 2nd longitudinal resonant state within the first transverse mode in MZI structure.

Experimentally people have shown ballistic transport in graphene nanoribbon and have made MZI interferometer structure in graphene nanoribbon with a width of 40 nm[2]. We have shown results for MZI structure with graphene nanoribbon width of 1 nm. The basic physics remains there when we go to higher width and we hope the device sizes will become smaller in future.

4.4 Graphene coherent spectrometer

In this section, we look at the optoelectronic properties of a semiconducting armchair graphene nanoribbon (AGNR) connected with two larger width metallic armchair graphene nanoribbons and how this structure can work as a spectrometer.

Our graphene spectrometer is based on the property of a graphene photodetector which can detect light of various frequencies with the change in Fermi level across the device. The bandwidth of the spectrometer can be changed by changing the width of

the bias voltage.

One of the larger width graphene nanoribbons works as source (supplier) of electrons and the other larger width nanoribbon works as drain (collector) of electrons. With the applied bias voltage no electron can pass through the device because the available states in the middle graphene nanoribbon are situated at larger energy. As we put the light in, electrons can make transition from lower energy state to higher energy state and can leave the device through the narrower width nanoribbon. By changing the bias voltage we can make electrons available at higher energies and the structure can detect light of different energies.

4.4.1 Device Geometry

We show the device geometry in Figure 60. The device is made of armchair type nanoribbons because armchair nanoribbons have band-gaps and does not have edge effects coming from edge magnetism.

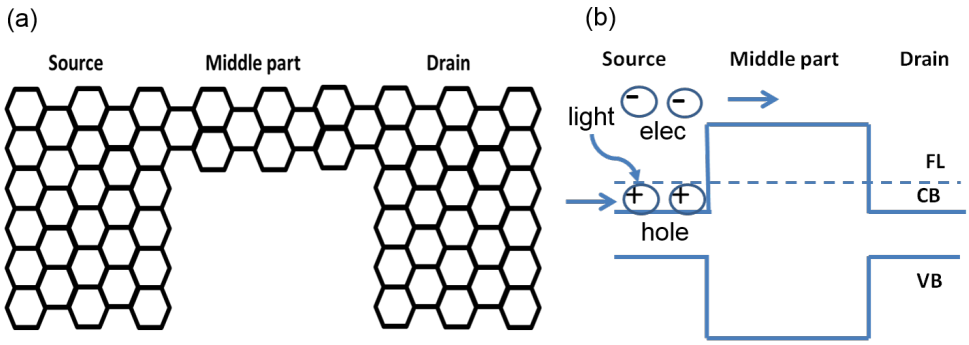

Figure 60. (a) Graphene spectrometer device structure (armchair type) (b) band diagram and operating principle

The device has three parts. The source part works as the reservoir and supplier of electrons, the middle nanoribbon part transmits electrons only when electrons have enough energy to occupy the first transverse mode in the conduction band in the middle nanoribbon and the drain part accepts the incoming electrons from the middle nanoribbon section.

The source and drain part can be made either semiconducting or metallic. If the source and drain parts are semiconducting, then the width of source and drain parts has

to be larger than the width of middle part so that the band-gap for source and drain parts are smaller than the band-gap for middle part. The source and drain have to be of same width so that net photocurrent comes only from the electrons which are situated in the applied voltage range. The middle nanoribbon is always made semiconductive so that it has a band-gap and electrons can pass only when electrons have greater energy than the energy of the first transverse mode in conduction band in the middle nanoribbon. The middle nanoribbon part is made long enough so that the tunneling current (dark current) through this part is negligible compared to photocurrent. For this simulation we have used 17-AGNR (metallic) for source and drain parts. We have shown simulation results for 3-AGNR, 7-AGNR and 9-AGNR (all semiconducting) in the middle nanoribbon section. The source and drain parts have 6 unit cells each and middle part has 15 unit cells.

4.4.2 Results and Discussion

The transmittance pattern for the structure is shown in the Figure 61 below. The source and drain are made of 17-AGNR and are metallic and middle nanoribbon part is made of 7-AGNR and semiconductive. The source and drain are conductive at all energies. So the transmittance of the device is primarily governed by the transmittance of the middle part. The device starts conducting at around 0.64 eV because at this energy the ground transverse mode in the middle nanoribbon part starts conducting.

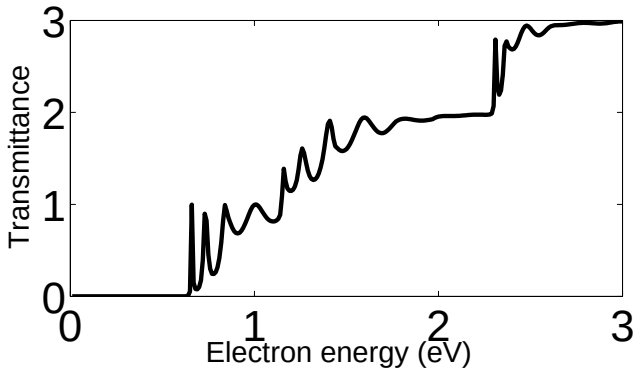

Figure 61. Transmittance pattern for the structure (armchair type).

The transmittance in the device can be larger than one (1) as shown in Figure 61.

The transmittance basically means the number of parallel transverse modes which are in conduction. The transmittance becomes two (2) at around 1.16 eV and the transmittance becomes three (3) at around 2.31 eV. From the band structure of 7-AGNR (middle nanoribbon), we can see that 1.12 eV is the onset energy for 2nd transverse mode and 2.29 eV is the onset energy of the 3rd transverse mode. This is a bit different than the device because the transmittance pattern in the device (7-AGNR with one 17-AGNR on either side) will be different from the transmittance pattern of the 7-AGNR only.

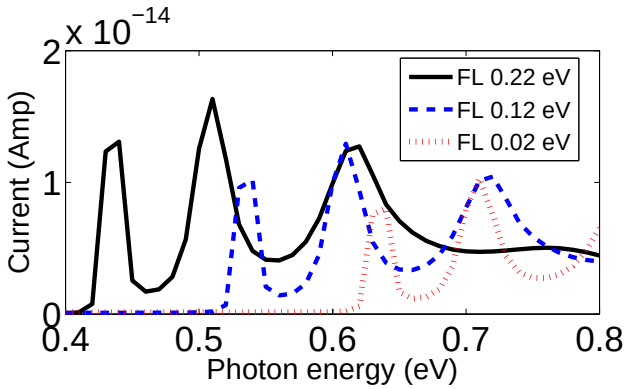

Figure 62. Variation of device current with different photon energy for different Fermi levels. Middle part is 7-AGNR and width of bias voltage is 0.01 eV.

In Figure 62, we see the variation of device current with photon energy for different Fermi levels. For this simulation the middle nanoribbon used is 7-AGNR. As we increase the Fermi level, the curves shift to the left because less photon energy is needed to put the electrons in the first transverse mode of the middle part. For a particular Fermi level, as photon energy is increased, the current through the device has some peaks and troughs. This comes because of variations in transmittance with electrons energy as is shown in Figure 61. From Figure 62, we notice that as Fermi level is decreased, the curves move to the right and the height (photocurrent) of the curves decreases. The photocurrent decreases because for this particular device photocurrent comes from intraband photoconductivity and intraband photoconductivity decreases with increasing photon energy.

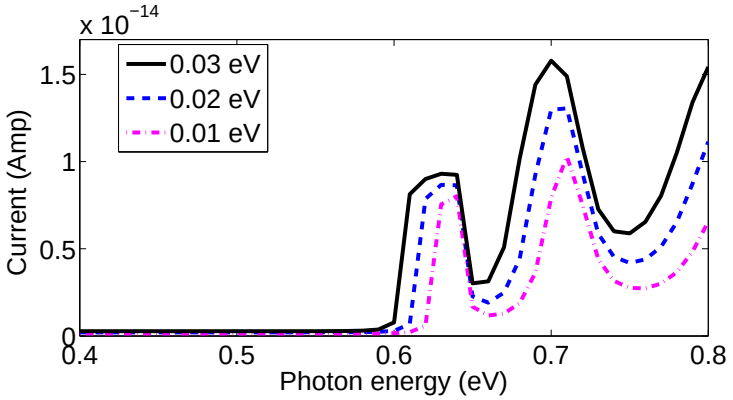

Figure 63. Variation of device current with different photon energy for different widths of bias voltages. Middle part is 7-AGNR and Fermi level is 0.02 eV.

In Figure 63, we see the variation of device current with photon energy for different widths of bias voltages. For this simulation the middle nanoribbon used is 7-AGNR. As we increase the width of bias voltage, the width of the peaks for the detected photons increase. For a particular photon energy, the lead photocurrent of the device is the convolution of optical absorption and transmittance of the device in the bias voltage range.

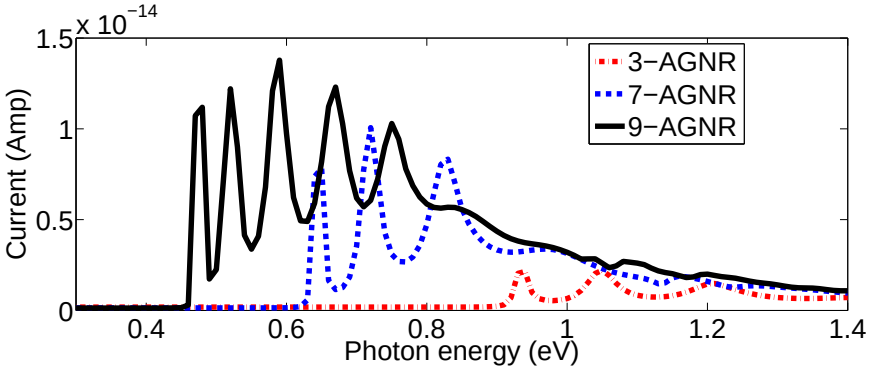

Figure 64. Variation of device current with different photon energy for different middle nanoribbon width. Fermi level is 0.02 eV and width of bias voltage is 0.01 eV.

In Figure 64, we see the variation of device current with photon energy for different middle nanoribbon width. From the band structure found from nearest neighbor tight-binding model, we find that the first transverse mode in conduction band starts at 1.12 eV, 0.635 eV and 0.475 eV for 3-AGAR, 7-AGNR and 9-AGNR respectively. We show here the simulation results for 3-AGAR, 7-AGNR and 9-AGNR. So photons of energy

1.12 eV, 0.635 eV and 0.475 eV at most can be detected by 3-AGAR, 7-AGNR and 9-AGNR respectively.

CHAPTER 5

CONCLUSION

In this thesis, we have explored the optical excitation of graphene nanoribbon having phase coherent electron transport. We have extensively looked at phenomena which arise when light interacts with phase coherent electron in both VB and CB. We have also investigated for the first time novel optoelectronic device ideas with sub Bloch wavelength of electron excitation. We have discovered new optical phenomenon and have also proposed three optoelectronic devices which are based on phase coherent electron transport and quantum interference of electrons in the VB and excited CB. As our understanding goes, this is a completely new research area and opens a paradigm for new opto coherent electronic research. We have outlined in our research four basic directions. The salient findings of our research are delineated below.

5.1 Illumination length dependent optical absorption of GNR

- We have shown that optical absorption is not independent of length of illumination but rather for very small scale illumination (where length of illumination is comparable with the Bloch wavelength of light) optical absorption depends on length of illumination. In general optical absorption is small for 1 unit cell and increases rapidly to a peak at a number that correspond to $\frac{1}{4}$ the Bloch wavelength. The absorption then decays (with damped oscillations) to its macroscopic limit. The Bloch wavelength is thus a suitable approximation for the length at which the long-illumination length optical absorption occurs.

- We see that when only a few unit cells are illuminated, absorption is dominated by very high density of states at the band edges (top of VB and bottom of CB). Then as number of unit cells illuminated is increased, momentum conserving electron transitions begin to take place.

- As more and more unit cells are illuminated, the peak of absorption (around momentum conserving energy) becomes narrower and narrower but at no point the

Heisenberg uncertainty relationship is violated.

- With the help of two level, 1-D atomic chain we have shown that Illumination length dependent optical absorption is coming from quantum interference of photoexcited electrons in CB and photoexcited holes in VB.

5.2 Current direction switching photodetector

- Our 2nd invention is a very simple nanoribbon photo-detector structure, in which the photocurrent in the external circuit (leads) changes direction depending on the frequency of incident light. The physical principle behind the phenomenon of direction of current switching is based on quantum interference of photoexcited electrons in multiple paths.

- We can change the direction of current by changing the illumination length or applied gate potential also.

- We have shown the CDS result is observed for various widths of nanoribbon and also for various bands of nanoribbon.

- With the help of a hypothetical two band 1-D structure, we have shown that this result is not graphene specific but rather is a generalized result. That is, the result is applicable for any semiconductor material with parabolic band structure because the result comes from interaction of photons with longitudinal wave patterns of electron.

- We have included the effect of electron-electron interaction in the CDS PD results. Since the photoexcited net charge density in the device is very small, this has negligible effect on the overall result.

- We have included the effect of elastic phonon dephasing in the CDS PD results. we have shown how coherent length is related with elastic phonon dephasing strength parameter. Then we have put all the results together and shown how decrease in coherent length due to elastic dephasing affects the CDS result.

5.3 Graphene quantum interference photodetector

- We have shown here a graphene nanoribbon Mach-Zhender interferometer photodetector structure which works by coupling of light between two longitudinal resonant modes. The longitudinal resonant modes arise because of quantum interference of electrons in the MZI structure.

- We have shown quantum efficiency results for both zig-zag and armchair nanoribbon structures. Armchair structure showed a QE of 5.2 % and zig-zag structure showed a QE of 1.6 %

- We have shown how QE does not remain constant with illumination length in the middle arm of the MZI structure. This result comes from illumination length dependent optical absorption of graphene nanoribbon when illumination length is around the Bloch wavelength of the electron.

5.4 Graphene coherent spectrometer

- In this section, we describe a graphene coherent spectrometer which can be made to detect photons of different energy by changing the Fermi level in the source and drain part of the device.

- This device work from intraband absorption rather than interband absorption.

- By changing the width of applied bias, we can change the linewidth of the detected photon energy

- This device has the advantage of low dark current, low tunneling current and tunability of detected photon energy and photon linewidth.

5.5 Future work

Richard Feynman famously remarked that there is plenty of room at the bottom. This thesis paves the way for a completely new field of opto coherent electronics, where phase coherent electron transport in ground and excited state with optical excitation for open device structures has been investigated for the first time.

In this thesis, we have performed our investigation on graphene nanoribbon. Other exciting 2-D materials like hexagonal boron nitride, molybdenum disulfide, transition metal di-chalcogenides (TMDC) should be investigated to find applicability as opto coherent electronic devices. Hexagonal boron nitride has a bandgap of 5 eV. 5 eV corresponds to a photon wavelength of 248 nm. This shorter wavelength light can be focused down to sub Bloch wavelength scale more easily.

We have outlined in the thesis that hyperfocusing of light can be achieved through plasmonic nanofocusing. For experimental realization of the CDS-PD device, we need more realistic modeling of the device. Future works should concentrate on this. Metal leads can be considered for collection of photocurrent from the device. Transparent ionic liquid can be used to put voltage on certain part of the device. Electric field profile on the nanoplasmonic focusing scheme should be investigated both experimentally and with simulation for experimental implementation of the optical part of the device.

More theoretical and experimental work is needed to investigate thoroughly the coherent behavior of electrons in 2-D materials in both ground and excited states. The times constants coming from electron-electron and electron-phonon interaction and their effect on the coherence of electrons should be investigated more thoroughly both experimentally and theoretically before the opto coherent electronic devices can be implemented experimentally.

REFERENCES

[1] Y.-C. Chen, T. Cao, C. Chen, Z. Pedramrazi, D. Haberer, D. G. de Oteyza, F. R. Fischer, S. G. Louie, and M. F. Crommie, "Molecular bandgap engineering of bottom-up synthesized graphene nanoribbon heterojunctions," *Nature Nanotechnology*, vol. 10, no. 2, pp. 156–160, 2015.

[2] J. Baringhaus, M. Ruan, F. Edler, A. Tejeda, M. Sicot, A.-P. Li, Z. Jiang, E. H. Conrad, C. Berger, C. Tegenkamp, and W. a. de Heer, "Exceptional ballistic transport in epitaxial graphene nanoribbons," *Nature*, vol. 506, pp. 349–354, Feb. 2014.

[3] N. C. Lindquist, P. Nagpal, A. Lesuffleur, D. J. Norris, and S. H. Oh, "Three-dimensional plasmonic nanofocusing," *Nano Letters*, vol. 10, no. 4, pp. 1369–1373, 2010.

[4] K. S. Novoselov, V. I. Fal'ko, L. Colombo, P. R. Gellert, M. G. Schwab, and K. Kim, "A roadmap for graphene.," *Nature*, vol. 490, pp. 192–200, Oct. 2012.

[5] F. Xia, H. Yan, and P. Avouris, "The Interaction of Light and Graphene: Basics, Devices, and Applications," *Proceedings of the IEEE*, vol. 101, pp. 1717–1731, July 2013.

[6] P. Avouris and M. Freitag, "Graphene photonics, plasmonics, and optoelectronics," *Selected Topics in Quantum Electronics, IEEE Journal of*, vol. 20, pp. 72–83, Jan 2014.

[7] F. Miao, S. Wijeratne, Y. Zhang, U. C. Coskun, W. Bao, and C. N. Lau, "Phase-coherent transport in graphene quantum billiards.," *Science (New York, N.Y.)*, vol. 317, pp. 1530–3, Sept. 2007.

[8] C. Berger, Z. Song, X. Li, X. Wu, N. Brown, C. Naud, D. Mayou, T. Li, J. Hass, A. N. Marchenkov, E. H. Conrad, P. N. First, and W. a. de Heer, "Electronic

confinement and coherence in patterned epitaxial graphene.," *Science (New York, N.Y.)*, vol. 312, pp. 1191–6, May 2006.

[9] H. B. Heersche, P. Jarillo-Herrero, J. B. Oostinga, L. M. Vandersypen, and a. F. Morpurgo, "Manifestations of phase-coherent transport in graphene," *The European Physical Journal Special Topics*, vol. 148, pp. 27–37, Sept. 2007.

[10] X. Du, I. Skachko, A. Barker, and E. Y. Andrei, "Approaching ballistic transport in suspended graphene," *Nat Nano*, vol. 3, pp. 491–495, Aug. 2008.

[11] S. Datta, *Lessons from Nanoelectronics- A New Perspective on Transport*. USA: World Scientific, 1 ed., 2012.

[12] S. Minke, J. Bundesmann, D. Weiss, and J. Eroms, "Phase coherent transport in graphene nanoribbons and graphene nanoribbon arrays," *Phys. Rev. B*, vol. 86, p. 155403, Oct 2012.

[13] Y. Wang, Z. Du, Y. Park, C. Chen, X. Zhang, and L. Pan, "Quasi-3D plasmonic coupling scheme for near-field optical lithography and imaging," *Optics Letters*, vol. 40, no. 16, p. 3918, 2015.

[14] A. K. Geim and K. S. Novoselov, "The rise of graphene," *Nat Mater*, vol. 6, pp. 183–191, Mar. 2007.

[15] K. S. Novoselov, A. K. Geim, S. V. Morozov, D. Jiang, Y. Zhang, S. V. Dubonos, I. V. Grigorieva, and A. A. Firsov, "Electric field effect in atomically thin carbon films," *Science*, vol. 306, no. 5696, pp. 666–669, 2004.

[16] Editorial, "It's still all about graphene," *Nat Mater*, vol. 10, p. 1, Jan. 2011.

[17] M. Breusing, C. Ropers, and T. Elsaesser, "Ultrafast carrier dynamics in graphite," *Physical Review Letters*, vol. 102, no. 8, pp. 1–4, 2009.

[18] M. Breusing, S. Kuehn, T. Winzer, E. Mali??, F. Milde, N. Severin, J. P. Rabe, C. Ropers, A. Knorr, and T. Elsaesser, "Ultrafast nonequilibrium carrier dynamics

in a single graphene layer," *Physical Review B - Condensed Matter and Materials Physics*, vol. 83, no. 15, pp. 1–4, 2011.

[19] J. M. Dawlaty, S. Shivaraman, M. Chandrashekhar, F. Rana, and M. G. Spencer, "Measurement of ultrafast carrier dynamics in epitaxial graphene," *Applied Physics Letters*, vol. 92, no. 4, pp. 16–19, 2008.

[20] H. Wang, J. H. Strait, P. A. George, S. Shivaraman, V. B. Shields, M. Chandrashekhar, J. Hwang, F. Rana, M. G. Spencer, C. S. Ruiz-Vargas, and J. Park, "Ultrafast relaxation dynamics of hot optical phonons in graphene," *Applied Physics Letters*, vol. 96, no. 8, pp. 19–22, 2010.

[21] D. Sun, Z. K. Wu, C. Divin, X. Li, C. Berger, W. A. De Heer, P. N. First, and T. B. Norris, "Ultrafast relaxation of excited dirac fermions in epitaxial graphene using optical differential transmission spectroscopy," *Physical Review Letters*, vol. 101, no. 15, pp. 1–4, 2008.

[22] H. Hsu and L. E. Reichl, "Selection rule for the optical absorption of graphene nanoribbons," *Phys. Rev. B*, vol. 76, p. 045418, Jul 2007.

[23] W. Liao, G. Zhou, and F. Xi, "Optical properties for armchair-edge graphene nanoribbons," *Journal of Applied Physics*, vol. 104, no. 12, pp. –, 2008.

[24] K.-i. Sasaki, K. Kato, Y. Tokura, K. Oguri, and T. Sogawa, "Theory of optical transitions in graphene nanoribbons," *Physical Review B*, vol. 84, p. 085458, Aug. 2011.

[25] S. Datta, *Electronic Transport in Mesoscopic Systems*. UK: Cambridge University Press, 5 ed., 2003.

[26] L. E. Henrickson, "Nonequilibrium photocurrent modeling in resonant tunneling photodetectors," *Journal of Applied Physics*, vol. 91, no. 10, p. 6273, 2002.

[27] L. Britnell, R. V. Gorbachev, A. K. Geim, L. A. Ponomarenko, A. Mishchenko, M. T. Greenaway, T. M. Fromhold, K. S. Novoselov, and L. Eaves, "Resonant

tunnelling and negative differential conductance in graphene transistors.," *Nature communications*, vol. 4, p. 1794, Jan. 2013.

[28] J. Munárriz, F. Domínguez-Adame, and A. V. Malyshev, "Toward graphene-based quantum interference devices.," *Nanotechnology*, vol. 22, p. 365201, Sept. 2011.

[29] Z. Wu, Z. Z. Zhang, K. Chang, and F. M. Peeters, "Quantum tunneling through graphene nanorings.," *Nanotechnology*, vol. 21, p. 185201, May 2010.

[30] Z. Z. Zhang, K. Chang, and K. S. Chan, "Resonant tunneling through double-bended graphene nanoribbons," *Applied Physics Letters*, vol. 93, no. 6, p. 062106, 2008.

[31] C. A. Stafford, D. M. Cardamone, and S. Mazumdar, "The quantum interference effect transistor.," *Nanotechnology*, vol. 18, p. 424014, Oct. 2007.

[32] T. Stoof and Y. Nazarov, "Time-dependent resonant tunneling via two discrete states," *Physical Review B*, vol. 53, pp. 1050–1053, Jan. 1996.

[33] C. Stafford and N. Wingreen, "Resonant Photon-Assisted Tunneling through a Double Quantum Dot: An Electron Pump from Spatial Rabi Oscillations," *Physical Review Letters*, vol. 76, pp. 1916–1919, Mar. 1996.

[34] F. Bonaccorso, Z. Sun, T. Hasan, and A. C. Ferrari, "Graphene photonics and optoelectronics," *Nat Photon*, vol. 4, pp. 611–622, Sept. 2010.

[35] A. Urich, K. Unterrainer, and T. Mueller, "Intrinsic response time of graphene photodetectors.," *Nano letters*, vol. 11, pp. 2804–8, July 2011.

[36] T. Mueller, F. Xia, and P. Avouris, "Graphene photodetectors for high-speed optical communications," *Nat Photon*, vol. 4, pp. 297–301, May 2010.

[37] E. Ahmadi, A. Asgari, and K. Ahmadiniar, "The optical responsivity in IR-photodetector based on armchair graphene nanoribbons with p-i-n structure," *Superlattices and Microstructures*, vol. 52, no. 4, pp. 605–611, 2012.

[38] F. Ostovari and M. K. Moravvej-Farshi, "Photodetectors with armchair graphene nanoribbons and asymmetric source and drain contacts," *Applied Surface Science*, pp. 1–5, Jan. 2014.

[39] M. Pourfath, O. Baumgartner, H. Kosina, and S. Selberherr, "Performance evaluation of graphene nanoribbon infrared photodetectors," *2009 9th International Conference on Numerical Simulation of Optoelectronic Devices*, no. July 2015, pp. 10–12, 2009.

[40] E. C. Peters, E. J. H. Lee, M. Burghard, and K. Kern, "Gate dependent photocurrents at a graphene p-n junction," *Applied Physics Letters*, vol. 97, no. 19, pp. 2010–2013, 2010.

[41] F. Xia, T. Mueller, Y.-M. Lin, A. Valdes-Garcia, and P. Avouris, "Ultrafast graphene photodetector.," *Nature nanotechnology*, vol. 4, pp. 839–43, Dec. 2009.

[42] F. Xia, T. Mueller, R. Golizadeh-Mojarad, M. Freitag, Y.-m. Lin, J. Tsang, V. Perebeinos, and P. Avouris, "Photocurrent imaging and efficient photon detection in a graphene transistor," *Nano Letters*, vol. 9, no. 3, pp. 1039–1044, 2009. PMID: 19203207.

[43] S. Datta, *Quantum Transport:Atom to Transistor*. USA: Cambridge University Press, 1 ed., 2005.

[44] S. Datta, "Nanoscale device modeling: the Green's function method," *Superlattices and Microstructures*, vol. 28, pp. 253–278, Oct. 2000.

[45] D. Stewart and F. Léonard, "Photocurrents in Nanotube Junctions," *Physical Review Letters*, vol. 93, p. 107401, Aug. 2004.

[46] J. Guo, M. A. Alam, and Y. Yoon, "Theoretical investigation on photoconductivity of single intrinsic carbon nanotubes," *Applied Physics Letters*, vol. 88, no. 13, p. 133111, 2006.

[47] S. Wohlthat, J. R. Reimers, and N. S. Hush, "Accurate and computationally efficient third-nearest-neighbor tight-binding model for large graphene fragments," *Physical Review B*, vol. 81, p. 195125, May 2010.

[48] A. H. Castro Neto, N. M. R. Peres, K. S. Novoselov, and A. K. Geim, "The electronic properties of graphene," *Reviews of Modern Physics*, vol. 81, pp. 109–162, Jan. 2009.

[49] H. Mohammadpour and A. Asgari, "Numerical study of quantum transport in the double-gate graphene nanoribbon field effect transistors," *Physica E: Low-dimensional Systems and Nanostructures*, vol. 43, no. 9, pp. 1708 – 1711, 2011.

[50] P. Marconcini, A. Cresti, F. Triozon, G. Fiori, B. Biel, Y.-M. Niquet, M. Macucci, and S. Roche, "Atomistic boron-doped graphene field-effect transistors: A route toward unipolar characteristics," *ACS Nano*, vol. 6, no. 9, pp. 7942–7947, 2012.

[51] J. Guo, "A quantum-mechanical treatment of phonon scattering in carbon nanotube transistors," *Journal of Applied Physics*, vol. 98, no. 6, p. 063519, 2005.

[52] Q. Gao and J. Guo, "Quantum mechanical simulation of graphene photodetectors," *Journal of Applied Physics*, vol. 112, no. 8, p. 084316, 2012.

[53] Y.-W. Son, M. L. Cohen, and S. G. Louie, "Half-metallic graphene nanoribbons," *Nature*, vol. 444, pp. 347–349, Nov. 2006.

[54] Z. F. Wang and F. Liu, "Giant magnetoresistance in zigzag graphene nanoribbon," *Applied Physics Letters*, vol. 99, no. 4, p. 042110, 2011.

[55] C. Tao, L. Jiao, O. V. Yazyev, Y.-C. Chen, J. Feng, X. Zhang, R. B. Capaz, J. M. Tour, A. Zettl, S. G. Louie, H. Dai, and M. F. Crommie, "Spatially resolving edge states of chiral graphene nanoribbons," *Nat Phys*, vol. 7, pp. 616–620, Aug. 2011.

[56] S. Ahsan, K. M. Masum Habib, M. R. Neupane, and R. K. Lake, "Interlayer magnetoconductance of misoriented bilayer graphene ribbons," *Journal of Applied Physics*, vol. 114, no. 18, p. 183711, 2013.

[57] J. C. Johannsen, S. Ulstrup, F. Cilento, A. Crepaldi, M. Zacchigna, C. Cacho, I. C. E. Turcu, E. Springate, F. Fromm, C. Raidel, T. Seyller, F. Parmigiani, M. Grioni, and P. Hofmann, "Direct view of hot carrier dynamics in graphene," *Phys. Rev. Lett.*, vol. 111, p. 027403, Jul 2013.

[58] D. I. Odili, Y. Wu, P. a. Childs, and D. C. Herbert, "Modeling charge transport in graphene nanoribbons and carbon nanotubes using a Schrodinger-Poisson solver," *Journal of Applied Physics*, vol. 106, no. 2, p. 024509, 2009.

[59] D. Johny, P. Pereira, D. Pulfrey, and L. Castroy, "A Schrodinger-Poisson Solver for Modeling Carbon Nanotube FETs," *NSTI-Nanotech*, vol. 3, no. 1, pp. 65–68, 2004.

[60] J. Velev and W. Butler, "On the equivalence of different techniques for evaluating the Green function for a semi-infinite system using a localized basis," *Journal of Physics: Condensed Matter*, vol. 16, pp. R637–R657, jun 2004.

[61] C. H. Lewenkopf and E. R. Mucciolo, "The recursive Green's function method for graphene," *Journal of Computational Electronics*, vol. 12, no. 2, pp. 203–231, 2013.

[62] A. Gupta, O. Alon, and N. Moiseyev, "Generation and control of high-order harmonics by the interaction of an infrared laser with a thin graphite layer," *Physical Review B*, vol. 68, no. 20, 2003.

[63] J. D. Griffiths, *Introduction To Qunatum Mechanics*. England: Pearson Education Limited, 2 ed., 2014.